



University
of Glasgow

Sjögren, Johan (2015) Pion photoproduction cross section at large momentum transfer. PhD thesis, University of Glasgow.

<http://theses.gla.ac.uk/6239/>

Copyright and moral rights for this thesis are retained by the author

A copy can be downloaded for personal non-commercial research or study, without prior permission or charge

This thesis cannot be reproduced or quoted extensively from without first obtaining permission in writing from the Author

The content must not be changed in any way or sold commercially in any format or medium without the formal permission of the Author

When referring to this work, full bibliographic details including the author, title, awarding institution and date of the thesis must be given.

Pion Photoproduction Cross Section at Large Momentum Transfer

Johan Sjögren

A thesis presented for the degree of
Doctor of Philosophy



Nuclear Physics
School of Physics and Astronomy
University of Glasgow
United Kingdom

February 27, 2015

*Dedicated to
Olivia and Viktor*

Pion Photoproduction Cross Section at Large Momentum Transfer

Johan Sjögren

Submitted for the degree of Doctor of Philosophy

February 27, 2015

Abstract

The Real Compton Scattering experiment was performed in Hall A at the Thomas Jefferson National Accelerator Facility. It was designed to measure, for Compton scattering and π^0 -photoproduction, the differential cross section over a range of kinematic points and the polarisation transfer to the proton at a single kinematic point. The full range of the experiment in Mandelstam variables t and s was $1.64 - 6.46 \text{ GeV}^2$ and $4.82 - 10.92 \text{ GeV}^2$ respectively with beam energies of $2 - 6 \text{ GeV}$. The motivation for the experiment is to test the cross section and polarisation transfer predictions of perturbative QCD versus that of predictions from Generalised Parton Distribution models. This thesis will give an overview of the pertinent theory, experimental setup in Hall A and the extracting of the π^0 -photoproduction cross section.

Declaration

The work presented in this thesis is based on research carried out within the the Nuclear Physics group of the School of Physics and Astronomy of the University of Glasgow, UK. The experiment was performed at the Thomas Jefferson National Accelerator Facility, Newport News, Virginia. No part of this thesis has been submitted elsewhere for any other degree or qualification and it is all my own work unless referenced to the contrary in the text.

Copyright © 2014 by Johan Sjögren.

“The copyright of this thesis rests with the author. Quotations and information derived from it must be acknowledged”.

Contents

| | |
|---|------------|
| Abstract | iii |
| Declaration | iv |
| 1 Introduction | 1 |
| 1.1 The Strong Force, QCD and the Nucleon | 2 |
| 1.2 Nucleon Structure from Electron Scattering | 5 |
| 1.2.1 Elastic Electron Scattering | 5 |
| 1.2.2 Deep Inelastic Scattering | 10 |
| 1.3 A Universal Core: Nucleon Structure from General Scattering Processes | 11 |
| 1.3.1 Generalised Parton Distributions | 13 |
| 1.3.2 Perturbative QCD | 17 |
| 1.4 Previous Results and Experiments | 18 |
| 1.4.1 Compton Scattering | 19 |
| 1.4.2 π^0 -photoproduction | 21 |
| 1.4.3 Results on pQCD: An Overview of the Past | 21 |
| 2 Experimental Setup | 23 |
| 2.1 Kinematics | 24 |
| 2.2 Jefferson Laboratory | 26 |
| 2.2.1 The Continuous Electron Beam Accelerator Facility | 26 |
| 2.3 Hall A Equipment | 29 |
| 2.3.1 Beamline Equipment | 29 |
| 2.3.2 Target and Radiator | 31 |
| 2.3.3 High Resolution Spectrometer | 33 |

| | | |
|----------|---|-----------|
| 2.3.4 | Focal Plane Polarimeter | 36 |
| 2.3.5 | HRS Optics Calibration | 38 |
| 2.4 | RCS Photon Spectrometer | 41 |
| 2.4.1 | Calorimeter | 41 |
| 2.4.2 | Energy Calibration | 43 |
| 2.4.3 | X & Y Positions | 44 |
| 2.4.4 | Electron-Photon Separation | 45 |
| 2.5 | Data Acquisition System | 46 |
| 2.5.1 | Trigger and Electronics | 46 |
| 2.5.2 | Data Readout & Software | 48 |
| 3 | The Monte Carlo Simulation | 49 |
| 3.1 | Beam Energy Profiles | 49 |
| 3.1.1 | Bremsstrahlung Calculation | 50 |
| 3.2 | Cross Sections | 52 |
| 3.3 | Event Generator | 54 |
| 3.4 | Corrections | 54 |
| 3.4.1 | Multiple Coulomb Scattering | 54 |
| 3.4.2 | Radiative Effects | 55 |
| 3.4.3 | π^0 - and η -decay | 56 |
| 3.5 | Detector Simulations | 56 |
| 3.5.1 | HRS | 56 |
| 3.5.2 | Calorimeter and Magnet | 56 |
| 4 | Data Analysis | 58 |
| 4.1 | Cut Definitions | 60 |
| 4.2 | Elastic Electron Scattering | 61 |
| 4.2.1 | <i>ep</i> : Timing and Background Subtraction | 61 |
| 4.2.2 | <i>ep</i> : Fiducial and Kinematical Data Reduction | 63 |
| 4.2.3 | <i>ep</i> : Event Identification | 67 |
| 4.2.4 | <i>ep</i> : Corrections | 71 |
| 4.2.5 | <i>ep</i> : Results | 72 |

| | | |
|----------|---|------------|
| 4.3 | π^0 -Photoproduction | 75 |
| 4.3.1 | π^0 : Timing and Background Subtraction | 75 |
| 4.3.2 | π^0 : Fiducial and Kinematical Data Reduction | 76 |
| 4.3.3 | π^0 : Event Identification | 80 |
| 4.3.4 | π^0 : Corrections | 84 |
| 5 | Results and Discussion | 86 |
| 5.1 | π^0 Results | 86 |
| 5.1.1 | Systematic Uncertainties | 86 |
| 5.2 | Kinematic Dependencies of the Cross Section | 89 |
| 5.2.1 | pQCD | 89 |
| 5.2.2 | GPDs | 94 |
| 5.3 | Conclusions and Discussion | 95 |
| A | Coordinate Systems | 97 |
| B | Reaction Reconstruction | 100 |
| C | Distributions for all Kinematic Points | 104 |
| D | Raw yields, Accumulated Charge and Monte Carlo Cross Section | 130 |
| | Bibliography | 132 |

List of Figures

| | | |
|------|---|----|
| 1.1 | Cross section for electron scattering on hydrogen | 6 |
| 1.2 | Electron scattering | 7 |
| 1.3 | Form factor fits | 9 |
| 1.4 | The scaling of $F_2(x, Q^2)$ | 12 |
| 1.5 | Deeply virtual scattering processes | 15 |
| 1.6 | Compton scattering and meson photoproduction in the handbag model | 16 |
| 1.7 | Compton scattering on the proton in pQCD | 18 |
| 1.8 | Previously published results from experiment e99-114 | 20 |
| | | |
| 2.1 | Experimental setup | 24 |
| 2.2 | HRS 3D-model | 25 |
| 2.3 | CEBAF overview | 28 |
| 2.4 | HRS-left detector package | 36 |
| 2.5 | Focal Plane Polarimeter | 38 |
| 2.6 | Reconstructions of sieve slit and target foil | 40 |
| 2.7 | Optics target variables | 41 |
| 2.8 | Energy calibrations | 44 |
| 2.9 | Calorimeter X & Y positions | 45 |
| 2.10 | Trigger scheme | 47 |
| 2.11 | Block summing scheme | 48 |
| | | |
| 3.1 | Monte Carlo flow chart | 50 |
| 3.2 | Comparison of bremsstrahlung spectra | 51 |
| 3.3 | Compton and π^0 cross section parametrisations | 53 |
| 3.4 | Distribution function for a 4.615 GeV beam with a 6.2% radiator . . . | 54 |

| | | |
|------|--|----|
| 4.1 | <i>ep</i> : Timing | 62 |
| 4.2 | <i>ep</i> : Calorimeter X hit positions; 3A | 63 |
| 4.3 | <i>ep</i> : Calorimeter Y hit positions; 3A | 64 |
| 4.4 | <i>ep</i> : HRS variables δ and θ_{tg} ; 3E | 64 |
| 4.5 | <i>ep</i> : HRS variables ϕ_{tg} and z_v ; 3E | 65 |
| 4.6 | <i>ep</i> : Reconstructed beam energy; 3A & 3E | 66 |
| 4.7 | <i>ep</i> : Reconstructed beam energy; 4D & 5D | 66 |
| 4.8 | <i>ep</i> : Hit position differences for electron scattering; 3A | 67 |
| 4.9 | <i>ep</i> : Hit position differences for electron scattering; 3E | 68 |
| 4.10 | <i>ep</i> : Hit position differences for electron scattering; 4D | 68 |
| 4.11 | <i>ep</i> : Hit position differences for electron scattering; 5D | 69 |
| 4.12 | <i>ep</i> : Energy differences; 3A & 3E | 69 |
| 4.13 | <i>ep</i> : Energy differences; 4D & 5D | 70 |
| 4.14 | Electron scattering cross section ratios | 73 |
| 4.15 | π^0 : Timing | 75 |
| 4.16 | π^0 : Calorimeter X hit positions; 3A | 76 |
| 4.17 | π^0 : Calorimeter Y hit positions; 3A | 77 |
| 4.18 | π^0 : HRS variables; 3E | 78 |
| 4.19 | π^0 : Reconstructed beam energy | 79 |
| 4.20 | π^0 : 2-dim hit position differences for π^0 photoproduction; 3A | 80 |
| 4.21 | π^0 : Hit position differences for π^0 photoproduction; 3A & 3E | 81 |
| 4.22 | π^0 : Hit position differences for π^0 photoproduction; 4D & 5D | 82 |
| 4.23 | π^0 : Energy differences for π^0 photoproduction | 83 |
| 5.1 | π^0 -photoproduction results. $\frac{d\sigma}{dt}$ vs. t | 88 |
| 5.2 | Scaling power extraction process for 80° and 90° | 91 |
| 5.3 | Scaling power extraction process for 100° and 110° | 92 |
| 5.4 | Scaling power extraction process for 120° | 93 |
| 5.5 | π^0 -scaling power. $n(\theta_{cm})$ vs. θ_{cm} | 93 |
| 5.6 | pQCD scaled results. $s^7 \frac{d\sigma}{dt}$ vs. $\cos(\theta_{cm})$ | 94 |
| 5.7 | GPD scaled results. $\frac{d\sigma/dt}{(s-u)^2/s^4u^2}$ vs. $ t $ | 95 |

| | | |
|-----|----------------------------------|----|
| A.1 | Coordinate systems | 98 |
| A.2 | VDC Coordinate systems | 99 |

List of Tables

| | | |
|-----|---|-----|
| 2.1 | Kinematic points | 27 |
| 2.2 | HRS specifications | 33 |
| 2.3 | Properties of TF-1 type lead glass | 43 |
| 4.1 | Electron scattering correction factors | 71 |
| 4.2 | Electron cross section ratios | 74 |
| 4.3 | π^0 correction factors | 84 |
| 5.1 | π^0 photoproduction cross section results | 87 |
| 5.2 | Systematic variation of the π^0 results | 90 |
| D.1 | π^0 : Raw extracted data. | 131 |

Chapter 1

Introduction

“Unaware of the scope of simple equations, man has often concluded that nothing short of God, not mere equations, is required to explain the complexities of the world.” - Feynman

Since the beginning of nuclear physics, experiments with electromagnetic probes have revealed much about the structure of hadronic matter and form a cornerstone of our present understanding of the strong force. Electromagnetic probes interact with the charged constituents of hadronic matter according to the well established and tested theory of Quantum Electro Dynamics(QED). They are therefore an excellent tool in our attempt to understand the presently accepted theory for the strong force, Quantum Chromo Dynamics(QCD), which the experimental and theoretical branches of hadron physics have struggled with for some 40 years now. One of the main goals of the work on QCD is still to understand the structure of hadronic matter, especially the nucleon, and the main goal of experiments on the nucleon is to understand how QCD may be used to describe hadronic structure. This coupled struggle is the context to which this thesis belongs.

The purpose of this chapter is to provide the motivation and the historical backdrop of experiments and theory, beginning with the history of QCD in the first section. The following sections will describe the experimental techniques, form factors and structure functions related to inelastic and elastic electron scattering on the nucleon, primarily the proton. The latter is of great importance to the simulation presented in Section 3.

The last two sections will focus on the theory and previous experiments that relate to this experiment, especially the work towards a general description of scattering processes. This is an area that faces many interconnected questions: what is the dominating reaction mechanism?; what is the structure?; how do we describe all processes in one framework? The important work done on Generalized Parton Distribution functions(GPDs), from which both the form factors and parton distribution functions can be obtained, is presented. It is promising that the GPDs can be connected not only to electron induced reactions but also photon induced reactions. Another very important approach is that of perturbative QCD(pQCD), which is expected to be valid in the high energy limit. The transition to pQCD marks the move from hadronic degrees of freedom to quark-gluon degrees of freedom. So it is of importance for the transition between the high and low energy descriptions of the strong force.

1.1 The Strong Force, QCD and the Nucleon

The field of nuclear physics is now over 100 years old. Its conception must be attributed to a sum of important discoveries made at the end of the 19th and the earliest part of the 20th century. The discovery of X-rays by Röntgen, for which he was awarded the first Nobel prize, and the works of Becquerel and the Curies (the 3rd Nobel prize) on radioactivity can be considered the first sparks. Rutherford's, and his co-worker's¹, scattering of α particles from a thin foil and the correct interpretation of the results, through the cross section formula named after him, established the model of the atomic nucleus. From this beginning the field of sub-atomic physics grew.

Meson exchange

The first quantum field theory for the strong force was proposed by Yukawa in 1935. He postulated the existence of pions, with non-zero mass m , as the mediators for

¹Geiger and Marsden.

the strong force, described by the potential:

$$V(r) = -g^2 \frac{e^{-kmr}}{r}, \quad (1.1)$$

bearing his name where g and k are scaling constants and r is the radial distance. The pions were subsequently discovered, but they did not come alone because more mesons were found by the early high energy accelerators. The Yukawa potential was a good attempt to describe the strong force and captures, not all, but many of the features of the nucleon-nucleon potential. By including other mesons as exchange particles into the "Meson exchange theory" it is possible to explain all aspects, except at extreme short ranges, of the nucleon-nucleon potential, at least to the limit of experimental knowledge. Of course this development did not exist in a scientific vacuum and discoveries such as those presented in Section 1.2 showed that the mesons and baryons had substructure. The meson theory could therefore not be the whole solution of the strong force.

QCD

QCD is, as mentioned above, the presently accepted underlying theory behind the strong force and at low momentum transfer it is the only truly non-perturbative theory included in the standard model. This theory grew out of the 60s quark model[1, 2] that in turn developed from the eightfold way by Gell-Mann and Ne'eman [3, 4]. The original quark model successfully used the proposed valence² quarks to classify the various particles that had been found up until this time period. This classification scheme lead to the prediction of Ω -baryons, in particular the Ω^- which was found in 1964[5]. Another model, the parton model, was developed around 1969, most notably by Feynman and Bjorken. The predictions of the model agreed with the discovery of scaling in Deep Inelastic Scattering(DIS), see Section 1.2.2. The parton properties were later found to be consistent with the quarks which together with DIS scaling brought general acceptance of the existence of the quark-parton.

²The quarks responsible for the hadron's quantum numbers.

The property of scaling in DIS implied that the underlying theory must exhibit asymptotic freedom, i.e. at high energies/short distances the quarks behave as a collection of free particles. No such theory was known at the time and this sparked a search for a quantum field theory fulfilling this demand. This ended with the formulation of QCD in 1973. That year Gross, Wilczek[6, 7] and independently Politzer[8, 9] found an SU(3) non-abelian gauge theory that fulfilled those demands and in the process solidified the concepts of colour charge and introduced the force mediating gluons.

Asymptotic freedom may be the property that defined QCD, but empirical knowledge puts more demands on this theory. The lack of a free quark is a phenomenon explained by the confinement property of QCD. There is certainly good empirical and some theoretical support for this property of QCD, especially through the approach suggested by Wilson[10] known as “lattice QCD”. There is, however, no analytical proof of confinement in QCD. Mathematically proving this is one of the Millennium price problems[11].

An interesting anomaly of the hadrons is the low mass of the pions (134.97 & 139.57 MeV) compared to the rest of the hadronic spectrum. The explanation is related to an important effect of the strong force; the generation of the majority of the nucleon mass and thus the majority of the visible mass of the universe. This occurs through the process of Dynamical Chiral Symmetry Breaking(DCSB)³ and the groundwork for this was laid by Nambu[12, 13] in 1960. The theory was inspired by a similar process in solid state physics, the BCS-theory[14] of super conductivity. The key feature is that the ground state is a degenerate quark condensate with mass even in the chiral limit(massless quarks), i.e.

$$\lim_{m_q \rightarrow 0} \langle 0 | q\bar{q} | 0 \rangle \neq 0. \quad (1.2)$$

The chiral symmetry, the symmetry between right and left handed⁴ particles, of the interaction is not a symmetry of this composite ground state. So the symme-

³Chiral symmetry is also explicitly broken by the non-vanishing masses of the quarks.

⁴If the projection of the spin onto the axis of motion is in the direction of motion it is right handed, otherwise it is left handed.

try is dynamically broken and the quark condensate "supplies" the hadron masses. Goldstone[15] proved that such symmetry breaking also requires the existence of connected massless bosons. In this case the three pions are those bosons and in the chiral limit they would have been massless, but as it stands they are only approximate Goldstone bosons courtesy of the explicit breaking of chiral symmetry.

1.2 Nucleon Structure from Electron Scattering

For the last 60 years or so, since the experiments of Hofstadter et al.[16–18] showed deviations from the distributions expected for a point-like proton as shown in Fig.1.1, the scattering of electrons from nucleons have allowed us access to much information about the structure of hadronic matter, in particular the proton. The elastic scattering of electrons have revealed the distributions of charge and magnetism within the proton, see Section 1.2.1, and inelastic scattering, see Section 1.2.2, has shown conclusive evidence for the point like quark/parton constituents of the proton and their distributions within it. These types of experiments were paramount to the development of QCD and remain a vital tool in the attempts to actually understand this theory.

1.2.1 Elastic Electron Scattering

The cross section for elastic electron scattering off a point-like charged particle, taking into account the recoil⁵ of the particle and the spin of the electron is given by the Mott cross section:

$$\left(\frac{d\sigma}{d\Omega}\right)_{Mott} = \alpha^2 \frac{E'}{4E^3} \frac{\cos^2 \theta/2}{\sin^4 \theta/2} \quad (1.3)$$

with α as the electromagnetic coupling constant, E and E' the initial and scattered electron energies respectively and θ is the electron scattering angle. As was found through the work of Hofstadter et al.[16–18] the proton has a structure that is more

⁵Mott scattering actually doesn't contain the recoil term (E'/E) in its original form, but for brevity it has been included here.

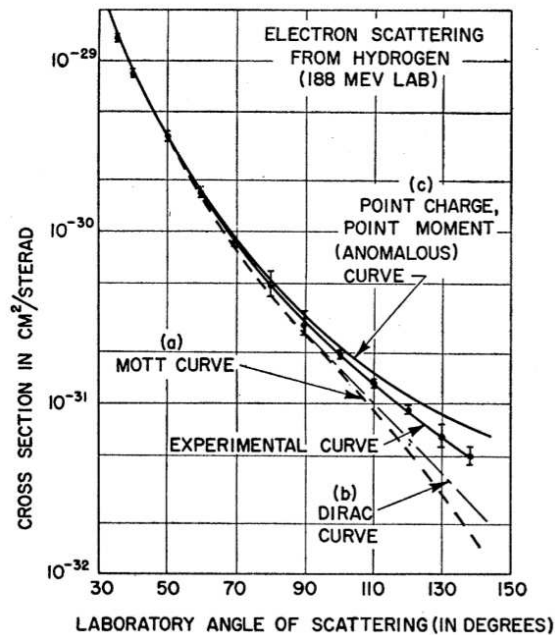


Figure 1.1: The Hofstadter results for the cross section of 188 MeV electrons scattering off hydrogen. The deviation from the theory lines suggested a proton with an inner structure. Picture from Ref. [16].

complex than a simple point charge, even if the anomalous magnetic moment is considered. This structure is encoded in the Dirac, $F_1(Q^2)$, and Pauli, $F_2(Q^2)$, electromagnetic form factors, as defined in Ref. [19]. Q^2 is given by

$$-q^2 = Q^2 = 4EE' \sin^2 \theta/2, \quad (1.4)$$

where q is the momentum of the virtual photon (see Fig. 1.2a) i.e. the momentum transfer. The dependence of these functions on the momentum transfer arises naturally from the relationship between the virtual photon's resolution power and its energy. When the contribution from the electric- and magnetic distributions are included, via these form factors, the cross section formula expands into

$$\frac{d\sigma}{d\Omega} = \left(\frac{d\sigma}{d\Omega} \right)_{Mott} \left(F_1^2(Q^2) + \tau \left[F_2^2(Q^2) + 2(F_1^2(Q^2) + F_2^2(Q^2)) \tan^2 \frac{\theta}{2} \right] \right) \quad (1.5)$$

where $\tau = Q^2/4m_p^2$ and m_p is the mass of the proton. The physical interpretation of F_1 and F_2 is not intuitive, but this can be partly remedied by introducing the Sachs

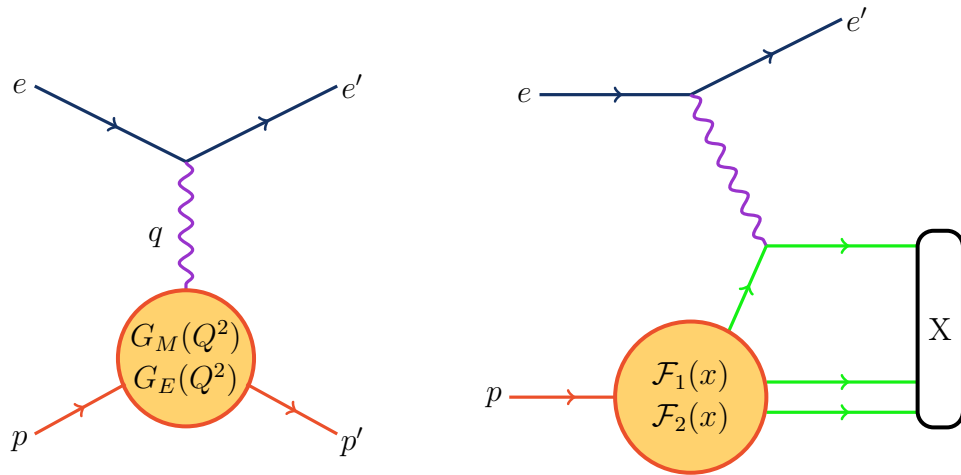
form factors

$$\begin{aligned} G_E(Q^2) &= F_1(Q^2) - \tau F_2(Q^2) \text{ and} \\ G_M(Q^2) &= F_1(Q^2) + F_2(Q^2). \end{aligned} \quad (1.6)$$

The $Q^2 \rightarrow 0$ limits, for the proton, of these form factors are the proton charge, $G_E(0) = 1$, and the protons magnetic moment, $G_M(0) = \mu_p$. Analogously for the neutron $G_E(0) = 0$ and $G_M(0) = \mu_n$. Written with the Sachs form factors eq.1.5 becomes

$$\frac{d\sigma}{d\Omega} = \left(\frac{d\sigma}{d\Omega} \right)_{Mott} \left[\frac{G_E^2 + \tau G_M^2}{1 + \tau} + 2\tau G_M^2 \tan^2 \frac{\theta}{2} \right] \quad (1.7)$$

which describes the process depicted in Fig. 1.2a. It is possible to derive further information about the proton structure from these form factors, for instance the radius of the proton that can be found from the slope of G_E . For more examples see Ref. [19], in particular Section 2.2.1. of that book.



(a) Elastic scattering of an electron on a nucleon.

(b) Inelastic scattering of an electron on a parton inside a nucleon causing it to end in the final state X.

Figure 1.2: Electron scattering

Form factor fits

Equation 1.7 is important to the simulation presented in Chapter 3, but there are no theoretically calculated form factors, at least not from first principles. Fortunately a wealth of measurements are available to allow reliable parametrisation, at least for the region with beam energies of a few GeV. One such is by P. Bosted[20],

$$G_{E_p}(Q^2) = \frac{G_{M_p}(Q^2)}{\mu_p} = \frac{1}{1 + 0.14Q + 3.01Q^2 + 0.02Q^3 + 1.20Q^4 + 0.32Q^5} \quad (1.8)$$

which is the one used in the Monte Carlo simulation(Chapter 3) for this experiment. Unfortunately, the relation, $G_{E_p}(Q^2) = \frac{G_{M_p}(Q^2)}{\mu_p}$, between the electromagnetic form-factors is subject to question since the turn of the millennium. Experiments[21, 22] that measured the transverse, P_t , and longitudinal, P_l , polarisation transfers to the proton to extract the form factor ratio via[23]

$$\frac{G_{E_p}}{G_{M_p}} = -\frac{P_t E + E'}{P_l 2m_p} \tan \theta/2 \quad (1.9)$$

did not agree with the expected $G_{E_p} = \frac{G_{M_p}}{\mu_p}$. Older unpolarised experiments had been in agreement with $G_{E_p} = \frac{G_{M_p}}{\mu_p}$. The determination of the form factors had previously been accomplished using the Rosenbluth separation technique[24] where one uses combinations of different beam energies and scattering angles which amount to constant Q to allow extraction of the form factors. This discrepancy sparked a number of experiments and theoretical investigations. Those prior to 2007 are reviewed in Ref. [25], but so far the results are inconclusive. Fortunately, at the energies of this experiment the cross section is dominated by G_{M_p} . So recent form factor fits such as those presented in Refs. [26, 27] do not yield very different results for the cross section. The Bosted fit is shown together with the data points used for the fit in Fig. 1.3a and a comparison with a different fit[26], that includes a few extra and some reanalysed data sets, is shown in Figs. 1.3b and 1.3c. The difference between them is small, of the order of a few percent.

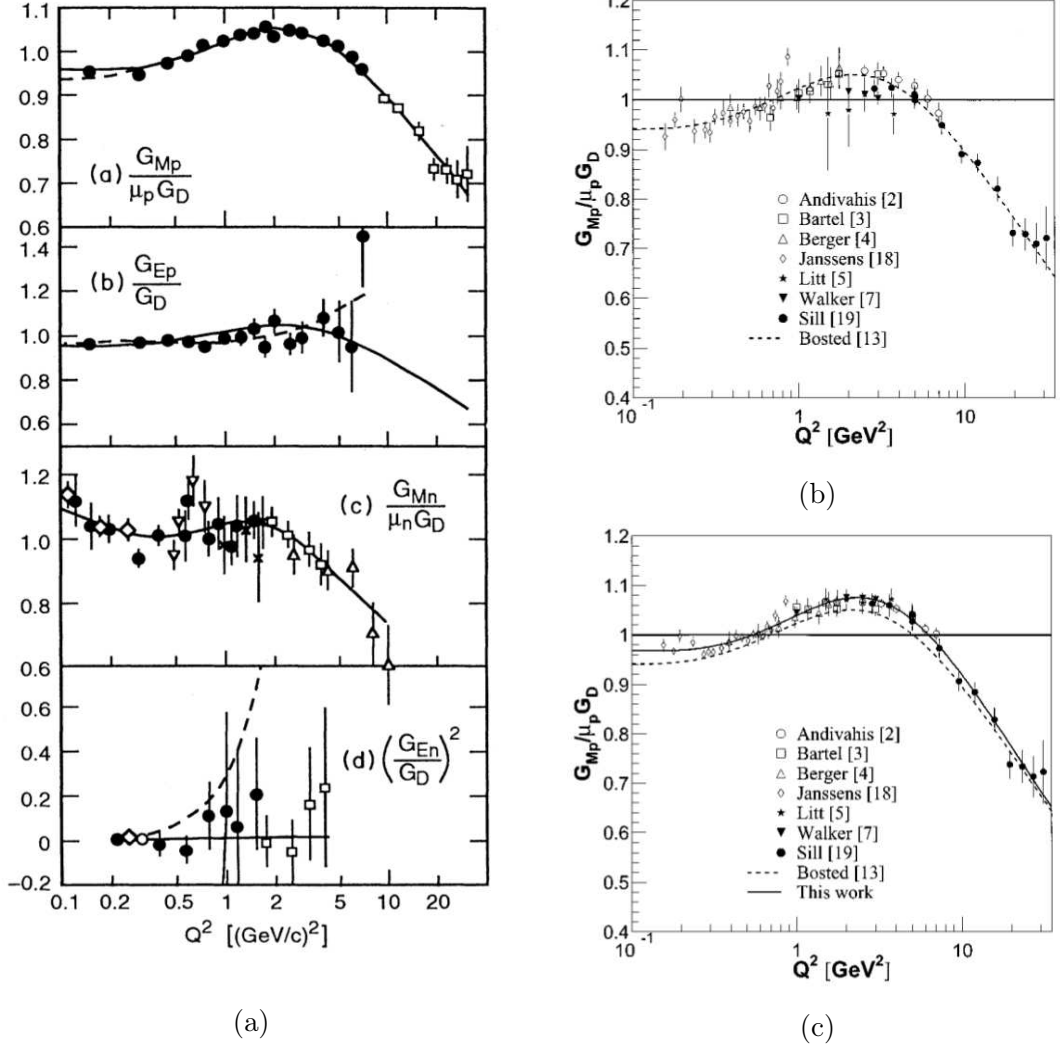


Figure 1.3: Fits to electromagnetic form factors. Picture (a) is from Ref. [20] and the top two plots show the fit of equation 1.8 as a solid line versus the then available data points for the proton form factors. The dashed lines are a set of (different) fits to G_{Mp} and G_{Ep} individually. The bottom two are fits to the neutron form factors. The pictures (b) and (c) are both from Ref. [26] with equation 1.8 included as a dashed line in both. Ref. [26] reanalysed the experimental results for $G_{Mp}/\mu_p G_D$, where G_D is the dipole form factor parametrisation ($G_D = (1 + Q^2/0.71)^{-2}$), and (b) shows the original values while (c) shows the reanalysed values with a new fit as a solid line.

1.2.2 Deep Inelastic Scattering

Deep inelastic scattering, depicted in Fig. 1.2b and extensively presented by Blümlein in Ref. [28], is the subject of study for inclusive experiments, where typically only the scattered electron is detected. Since the final state on the hadron side is unknown, the description of the cross section must be a sum of all possible final states. This means that the momentum transfer given by eq.1.4 is no longer a valid scaling variable and must be augmented by the energy transfer, ν , to the proton. The cross section is in this case given by

$$\frac{d^2\sigma}{d\Omega dE} = \frac{\alpha_{elm}^2}{4E^2 \sin^4 \theta/2} \left[W_2(\nu, Q^2) \cos^2 \frac{\theta}{2} + 2W_1(\nu, Q^2) \sin^2 \frac{\theta}{2} \right] \quad (1.10)$$

where new structure functions $W_{1,2}(\nu, Q^2)$ have been introduced. The most interesting behaviour of $W_{1,2}$ in the high energy limit is the property of Bjorken scaling. If the proton is made of spin-1/2 point-like partons, as in the Quark Parton Model(QPM) then $W_{1,2}$, in the high momentum transfer limit, should depend only on the Bjorken variable, $x \equiv \frac{Q^2}{2M\nu}$, that is

$$\begin{aligned} MW_1(\nu, Q^2) &\rightarrow F_1(x, Q^2) \equiv \mathcal{F}_1(x) \text{ and} \\ \nu W_2(\nu, Q^2) &\rightarrow F_2(x, Q^2) \equiv \mathcal{F}_2(x). \end{aligned} \quad (1.11)$$

Bjorken scaling behaviour is indeed found already at a few GeV, see Fig.1.4 and Refs. [29, 30]. The result, that was a surprise at the time, is of vital importance for the partonic picture of the nucleon, and QCD, as it is clear evidence that the nucleon is a composite object made of spin-1/2 point-like partons and implies asymptotic freedom, the defining property of QCD. The reader should note that the quark parton model naively disregards the gluons. Including the effect of the gluons explains the deviation seen in Fig. 1.4 from a flat line for large and small values of x .

$\mathcal{F}_1(x)$ and $\mathcal{F}_2(x)$ can be related to the momentum distributions of the quarks and gluons by boosting to the infinite momentum frame where the Bjorken x is the fraction of the nucleon momentum carried by the quark. Using the Callan-Gross relation, $2x\mathcal{F}_1(x) = \mathcal{F}_2(x)$, the momentum distributions or parton distributions for

the quarks $q(x)$ and the anti-quarks $\bar{q}(x)$ are accessed via

$$2xF_1(x) = \mathcal{F}_2(x) = x \sum_q e_q^2 (q(x) + \bar{q}(x)). \quad (1.12)$$

It is also possible to obtain, from polarised beam and target experiments, the polarised parton distribution functions for quarks $\Delta q(x)$ and anti-quarks $\Delta \bar{q}(x)$. The definition is $\Delta q(x) \equiv q(x)^\uparrow - q(x)^\downarrow$ and $\Delta \bar{q}(x) \equiv \bar{q}(x)^\uparrow - \bar{q}(x)^\downarrow$ where $q(x)^\uparrow(\downarrow)$ and $\bar{q}(x)^\uparrow(\downarrow)$ are the quark and anti-quark distributions with spin parallel(anti-parallel) to the proton.

1.3 A Universal Core: Nucleon Structure from General Scattering Processes

The above sections have described the strictly exclusive and inclusive scattering of electrons. There is a huge variety of other possible processes for incident electrons and photons that can be measured in experiments. Examples include, but are certainly not limited to, deeply virtual Compton scattering, Compton scattering and meson photo- and electroproduction. All of these access different distribution functions that are naturally related as they probe on some level the fundamental nucleon structure.

It is a daunting task, possibly an analytically impossible one, to calculate the properties of the nucleon from first principles and here phenomenology is an essential guide. Thus a large effort is put into understanding not immediately the full structure but rather particular localised views. The concept of factorisation is very important here. Factorisation is an approximation whereby the reaction mechanism is assumed to be separable into a hard, perturbative (and thus calculable) part and a soft, non-perturbative part that encodes much of the actual structure. This soft part should be universal, or at least obtainable from a universal structure function, and the hard part specific to the reaction. Factorisation is indeed assumed in the previously discussed electron scattering, see Figs. 1.2b and 1.2a.

There are several possible schemes of factorisation and the question is, at a

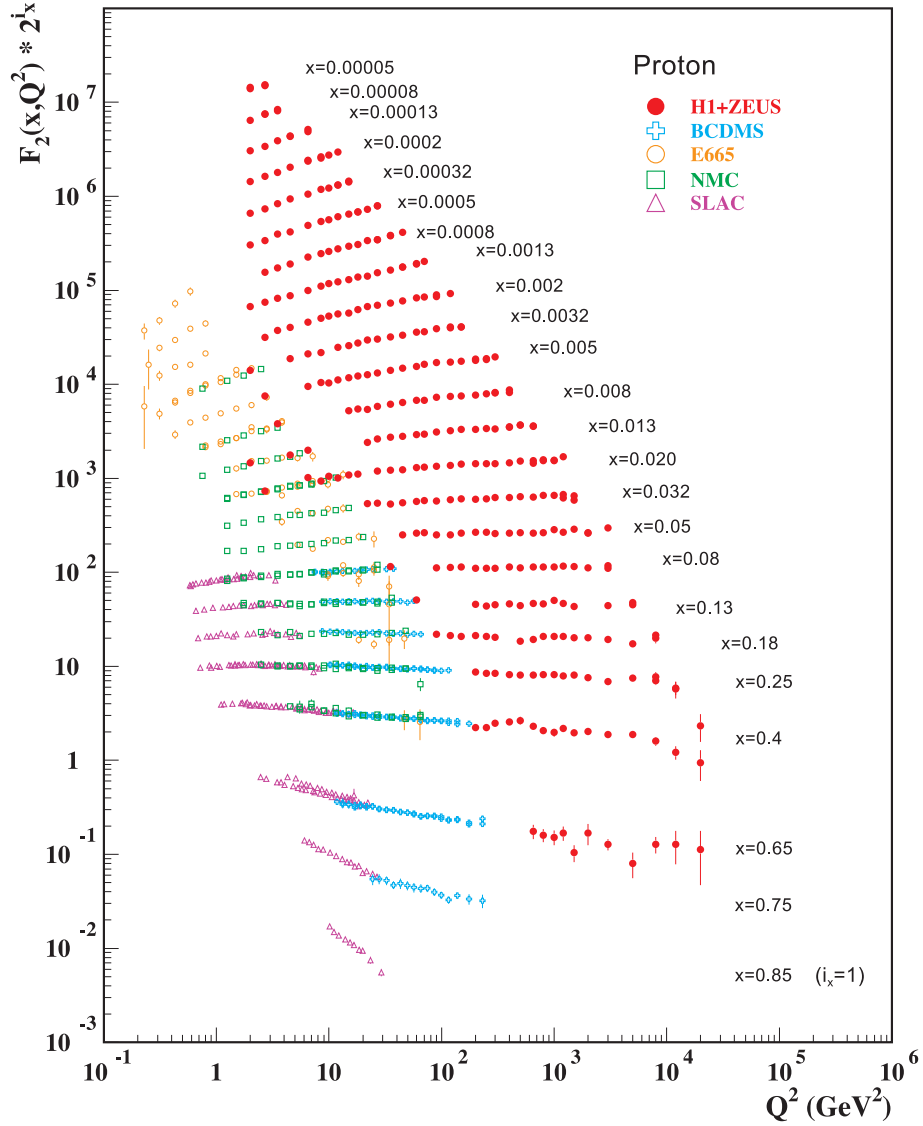


Figure 1.4: The scaling of $F_2(x, Q^2)$ measured in collider experiments over a large energy range, roughly 5 orders of magnitude. Picture from Ref. [31].

given energy, which is the dominating one(s). The remaining parts of this chapter will focus on the two that are presently of most interest to π^0 -photoproduction in the wide-angle few GeV energy range. The first factorisation scheme, see Section 1.3.1, is the Handbag-model and the soft-structure functions are the GPDs. These are connected to the previously mentioned parton distribution functions and the electromagnetic form factors and have been of increasing interest to the community for around 20 years. The other factorisation scheme discussed in Section 1.3.2 is that of pQCD which is supposed to dominate at large energies.

1.3.1 Generalised Parton Distributions

GPDs offer a way of connecting the parton distribution functions with the electromagnetic form factors so they are a natural step towards a general structure function. The approach centres around the Handbag-model, seen in Figs. 1.5 and 1.6, in which the nucleon emits a quark carrying a momentum fraction of $x + \xi$ who participates in the perturbatively calculable scattering process and is finally reabsorbed carrying a momentum fraction of $x - \xi$. GPDs are parametrisations of the quark emission and absorption process. They are parametrised in terms of the momentum transfer⁶, t , from the initial to the final nucleon, the average momentum fraction⁷, x , of the struck quark and the skewness, ξ , which is the asymmetry between the momentum of the emitted and absorbed quark. An important property of GPDs, which was hinted at in the previous section, is universality. The ellipses in Figs. 1.5a and 1.5b⁸ represent the same GPD; the differences lie in the hard-part. This should also be true when the incoming photon is/becomes real and it is through this that reactions induced by photons, as opposed to virtual photons, can be of great interest when testing the predictions of a GPD approach.

⁶The Mandelstam variable.

⁷Note that in the infinite momentum frame this is the same as the Björken x defined previously.

⁸The smaller ellipse in Fig. 1.5b represent the meson distribution amplitude.

Basic properties

In the forward limit, $\xi = 0$ and $t = 0$, the GPDs reduce to the parton distributions

$$\begin{aligned}
 H^q(x, \xi = 0, t = 0) &= q(x), \\
 \tilde{H}^q(x, \xi = 0, t = 0) &= \Delta q(x) \text{ for } x > 0 \text{ and} \\
 H^q(x, \xi = 0, t = 0) &= \bar{q}(x), \\
 \tilde{H}^q(x, \xi = 0, t = 0) &= \Delta \bar{q}(x) \text{ for } x < 0
 \end{aligned} \tag{1.13}$$

where $q(x)$ and $\Delta q(x)$ are the parton distribution functions defined previously and $-x$ is interpreted as x pertaining to anti-quarks. For zero-skewness, $\xi = 0$, the first moments of the GPDs correspond to the form factors.

$$\begin{aligned}
 \sum_q e_q \int_{-1}^1 dx H^q(x, \xi = 0, t) &= \sum_q F_1^q(t) = F_1(t) \\
 \sum_q e_q \int_{-1}^1 dx E^q(x, \xi = 0, t) &= \sum_q F_2^q(t) = F_2(t) \\
 \sum_q e_q \int_{-1}^1 dx \tilde{H}^q(x, \xi = 0, t) &= \sum_q g_A^q(t) = g_A(t) \\
 \sum_q e_q \int_{-1}^1 dx \tilde{E}^q(x, \xi = 0, t) &= \sum_q g_P^q(t) = g_P(t)
 \end{aligned} \tag{1.14}$$

where $F_{1,2}$ are again the Pauli and Dirac form factors and g_A and g_P are the axial and pseudoscalar form factors related to the weak, rather than the electromagnetic, current.

Spin off

In the late 1980s the spin crisis emerged as the European Muon Collaboration found that the spin of the quarks, Σ , only contributed a part of the proton spin[32]. So the spin of the proton must be a sum of not only the quark spin but also the quark orbital angular momentum, L_q , and possibly gluon terms, J_g , i.e. $\frac{1}{2} = \Sigma + L_q + J_g = J_q + J_g$. Thus when Ji[33] proposed a way of decomposing the spin structure and measuring

J_q through GPDs and his sum rule

$$\frac{1}{2} \int_{-1}^1 x[H^q(x, \xi, t) + E^q(x, \xi, t)]dx = J_q \quad (1.15)$$

the world interest in GPDs rose. The further works of Ji[34] and Radyushkin[35, 36] highlighted deeply virtual Compton scattering and deeply virtual meson production (or meson electroproduction), see Figs. 1.5a and 1.5b, as ideal reactions for access to the $\xi \neq 0$ parts of the GPDs.

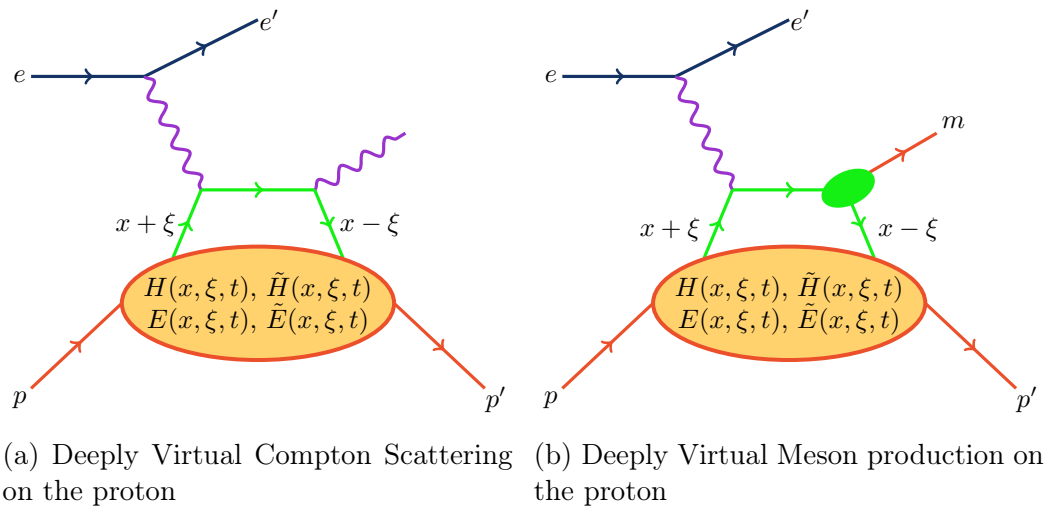


Figure 1.5: Deeply virtual scattering processes.

GPDs and real photons

Compton scattering off a point like charge with mass m is described by the Klein-Nishina formula:

$$\frac{d\sigma_{KN}}{dt} = \frac{2\pi\alpha^2}{s^2} \left(\frac{\tilde{s}}{\tilde{u}} + \frac{\tilde{u}}{\tilde{s}} \right) \quad (1.16)$$

where modified Mandelstam variables $\tilde{s} = s - m^2$, $\tilde{u} = u - m^2$ are used and factors of $\mathcal{O}(m^2)$ and $\mathcal{O}(m^4)$ have been omitted. Just as for electron scattering in Section 1.2 the cross section formula for scattering off a composite object, like the nucleon, is modified by the inclusion of form factors specific to Compton scattering. In the Handbag/GPD approach, see Fig. 1.6a, the cross section formula [37, 38] is given

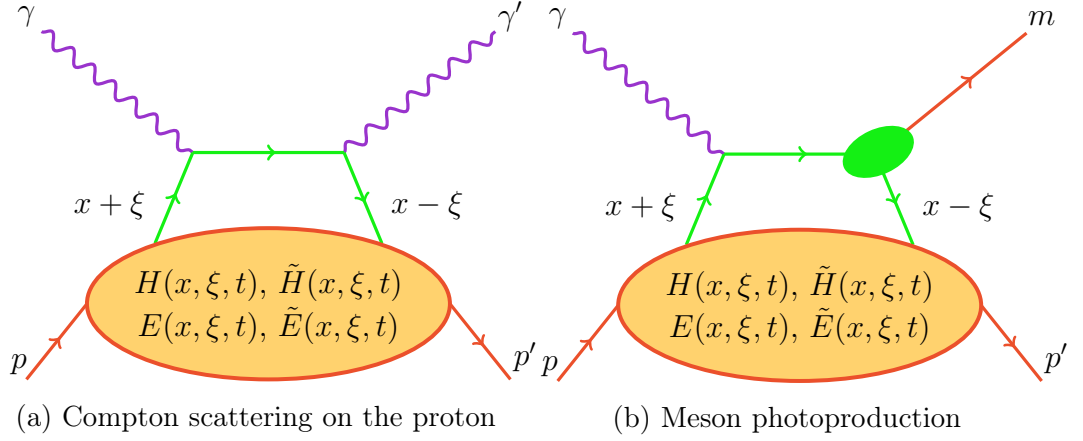


Figure 1.6: Compton scattering and meson photoproduction in the handbag model.

by

$$\frac{d\sigma}{dt} = \frac{d\sigma_{KN}}{dt} \left(\frac{1}{2} [R_V^2(t) + \frac{-t}{4M^2} R_T^2(t) + R_A^2(t)] - \frac{us}{s^2 + u^2} [R_T^2(t) + \frac{-t}{4M^2} R_T^2(t) - R_A^2(t)] \right) \quad (1.17)$$

where $R_{A,T,V}$ are respectively the axial, tensor and vector Compton specific form-factors and s , t and u are the Mandelstam variables. These form factors are the $1/x$ moments of the (universal) GPDs, that is

$$\begin{aligned} R_V(t) &= \sum_q e_q^2 \int_{-1}^1 \frac{dx}{x} H^q(x, 0, t), \\ R_T(t) &= \sum_q e_q^2 \int_{-1}^1 \frac{dx}{x} E^q(x, 0, t) \text{ and} \\ R_A(t) &= \sum_q e_q^2 \int_{-1}^1 \frac{dx}{x} \text{sign}(x) \tilde{H}^q(x, 0, t). \end{aligned} \quad (1.18)$$

The simplest photon induced reaction after Compton scattering is π^0 photoproduction, see Fig. 1.6b. The cross section formula is [39, 40]

$$\frac{d\sigma}{dt}(\gamma p \rightarrow \pi^0 p) = \alpha a^2 \frac{t(s-u)^2}{32s^4u^2} \left[(R_V^{\pi^0})^2 + \frac{-t}{4m^2} (R_T^{\pi^0})^2 + \frac{t^2}{(s-u)^2} (R_A^{\pi^0})^2 \right] \quad (1.19)$$

where s , t and u are the Mandelstam variables, $R_{V,T,A}^{\pi^0}$ are respectively the vector, tensor, and axial form factors given by a sum[41] of the up and down quark

contributions

$$R_i^{\pi^0} = \frac{1}{\sqrt{2}}(e_u R_i^u - e_d R_i^d). \quad (1.20)$$

a is often used as a free parameter fitted to obtain a good description of the photo-production cross section, but in the asymptotic limit of large Mandelstam variables the meson is formed through a one-gluon exchange. The result is that a is given by:

$$a = \frac{16}{9}\alpha_s f_\pi \langle 1/\tau \rangle_\pi \quad (1.21)$$

where α_s is the strong coupling constant, f_π is the π^0 decay constant and $\langle 1/\tau \rangle_\pi$ is the $1/\tau$ moment of the pions Distribution Amplitude.

1.3.2 Perturbative QCD

Inspired by the scaling results of deep inelastic scattering, an approach to predict the asymptotic behaviour for the cross section of electromagnetic and hadronic scattering, based on the quark model, was found independently by Brodsky and Lepage[42] and Matveev[43]⁹ in 1973. The result is a power law (scaling) of the cross section as a function of the centre-of-mass energy, s , and angle, θ_{cm} , like so:

$$\frac{d\sigma}{dt} \propto \frac{f(\theta_{cm})}{s^{N-2}} = \frac{f(\theta_{cm})}{s^n} \quad (1.22)$$

where N is the total number of involved constituents¹⁰. The rule is also known as the Constituent Counting Rule (CCR). This result was later shown to be consistent with the pQCD[44] prediction. The result for pQCD is obtained by assuming a factorisation different from the Handbag and an energy regime where the quarks are free, approximately massless, only the valence quarks participate through a minimum of hard gluon exchange and quark orbital angular momentum is neglected. The leading order diagram is shown in Fig. 1.7 and the two ellipses represent the Distribution Amplitudes that encode the soft, non-perturbative parts of the reaction. One should also note here that there is an interesting prospect, presented in Ref. [45],

⁹Ref. [43] is very often overlooked because he only derived the relation for elastic scattering.

¹⁰Incoming and outgoing quarks, real and virtual photons.

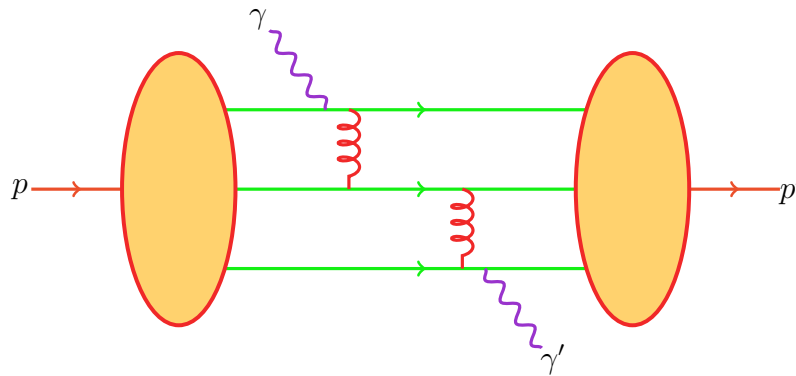


Figure 1.7: Compton scattering on the proton in pQCD. This is only one of a large number of possible diagrams that contribute.

that the oscillations of the cross section as a function of s about an average scaling found in pp scattering may also occur in pion photoproduction.

Another prediction of pQCD is Hadron Helicity Conservation(HHC)[46]. This can be tested for example through measurements of the polarisation transfer from a polarised beam of electrons or photons to a nucleon. However, if quark orbital angular momentum effects are included then there exists a mechanism that allows breaking[47] of HHC within the framework of pQCD. This is an interesting prospect due to the previously mentioned discovery that the quark spin only contributed a part of the proton spin[32].

1.4 Previous Results and Experiments

An excellent way of measuring the validity and accuracy of the theories and models presented in this chapter is to use beams of electrons and photons impinging on, primarily, a hydrogen target. The work of this thesis relates to such an experiment, the Real Compton Scattering experiment, E99-114, where a photon beam ranging in energy between 2-6 GeV were used to study scattering and photoproduction processes at wide centre-of-mass angles. The final goal was to test and compare the GPD approach, presented in Section 1.3.1, with qQCD, presented in Section 1.3.2.

1.4.1 Compton Scattering

Compton scattering was the other main target reaction channel for this experiment. The only available data, prior to this experiment, for Compton scattering in the few GeV range, covering wide centre-of-mass angles are from experiments, extracting the cross section[48, 49] and the recoil-proton polarisation[50], performed in the late 70s at Cornell. The cross section results of [48, 49] give a weighted scaling power of $n = 6.4 \pm 0.3$ which is “in reasonable agreement” with CCR and pQCD predictions of $n = 6$. The cross sections, see Fig. 1.8b, and the scaling measured in the present experiment is not, as seen in Fig. 1.8a, in agreement with CCR and pQCD.

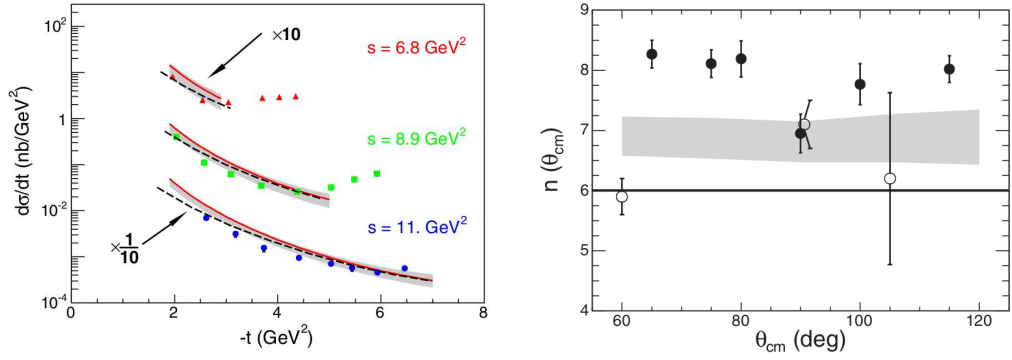
Longitudinal polarisation transfer is measured through the parameter K_{LL} ¹¹ defined by

$$K_{LL} = \frac{d\sigma(\uparrow\uparrow) - d\sigma(\uparrow\downarrow)}{d\sigma(\uparrow\uparrow) + d\sigma(\uparrow\downarrow)} \quad (1.23)$$

where $d\sigma(\uparrow\uparrow)$ ($d\sigma(\uparrow\downarrow)$) is the cross section with the photon helicity (anti-)parallel to the longitudinal polarisation of the recoiling proton. Just as in the case of the cross section, the measurement of the polarisation transfer to the proton does not agree with pQCD but agrees better with other models, including GPD approaches.

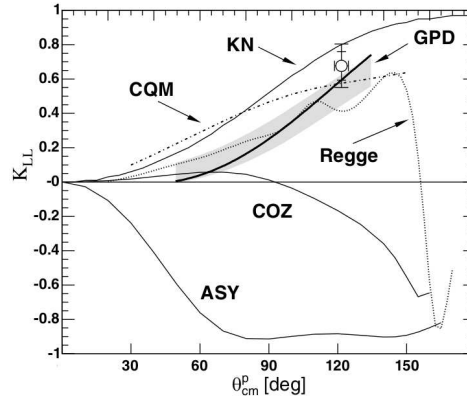
Much more detail concerning the Compton measurement and connected theories can be found in the articles and theses by D. Hamilton[51, 52], A. Danagoulian[53, 54] and V. Mamyan[55].

¹¹This is called P_l in eq. 1.9.



(a) The Compton cross section, $\frac{d\sigma}{dt}$, as a function of t . The lines are GPD based predictions. The solid line is based on the approach in Ref.[56] and the shaded region results from mass uncertainties, see Ref. [57]. The dashed line is the prediction obtained using the approach in Ref. [58]. Results and picture from Ref. [54]

(b) The extracted scaling behaviour for the Compton channel from this experiment (closed points) and from the Cornell measurement [48, 49] (open points). The pQCD prediction ($n=6$) is shown by the solid line and the shaded region the range expected from a GPD approach [56, 57], including mass uncertainties. Results and picture from Ref. [54]



(c) The measured value for K_{LL} from this experiment compared with a number of predictions. ASY and COZ are pQCD predictions from Ref. [59], GPD from Ref.[56](line) and Ref.[57](shaded region), Constituent Quark model(CQM) from Ref.[58], Regge from Ref.[60] and KN is the asymmetry from a point-proton, i.e. the “Klein-Nishina” prediction. Results and picture from Ref.[52]

Figure 1.8: Previously published results from experiment E99-114.

1.4.2 π^0 -photoproduction in the GeV Range

4 π detectors

A substantial amount of data on the $\gamma + p \rightarrow p' + \pi^0$ channel exists in the incident energy region around 1 GeV due largely to Baryon Spectroscopy interests, see [61] for a recent overview. Above this region the number of available data points starts to trail off but there are still a couple of experiments[62–65] whose kinematics overlap the energy points below 3 GeV of this experiment. These results are from the 4 π detector experiments CLAS and the Crystal Ball with TAPS and are in fair agreement with each other¹². A comparison is made to a subset of the the CLAS data in Section 5.2.

Limited detector aperture experiments

There have been a series of measurements with kinematics, both s and t , very similar to this experiment in the 70s, by Anderson et al.[66] at SLAC and by Shupe et al.[48, 49] at Cornell. About the same time measurements were also made for a range in s of 4 – 18 GeV² but not in the wide angle($\cos\theta_{cm} < |0.4|$) regime by Braunschweig et al.[67] at DESY and at SLAC by Anderson et al.[68–70]. All of these experiments, except [67], utilised a magnetic spectrometer for the detection of the recoiling proton as in the present experiment. Comparisons are made to the results of Anderson and Shupe in Section 5.2.

1.4.3 Results on pQCD: An Overview of the Past

Historically the tests of CCR and pQCD have yielded mixed results, see for example agreement in hadron-hadron and meson-hadron scattering in Ref. [71]. The early pion photoproduction experiment of Ref. [66] agrees for all species of pion as do later measurements on the charged pions[72]. Alas another experiment[49] from the 70s found that π^0 -photoproduction doesn't scale as predicted, but found that the Compton channel was in reasonable agreement. The present Compton experiment

¹²At least for the data points, and to a level, of use to this thesis.

reached a different conclusion as discussed earlier. For elastic scattering of electrons it has been found by Ref. [73] that scattering¹³ on deuterons follow pQCD. For scattering on protons the results were initially in agreement with pQCD[74], but later contradicted by the work of Ref.[75]. As mentioned in Section 1.2.1 the picture was complicated further in the early 2000's by the discovery that Rosenbluth separation techniques and polarisation techniques for extracting the form factors yielded different results.

The apparent agreement with scaling laws found in deuteron photodisintegration at wide angles in many experiments[76–79] and at surprisingly low values of s and $t(1\text{ GeV}^2)$ seems to be anomalous. This prompted an investigation of π^0 -photoproduction on the deuteron. The results of that measurement[80] were not consistent with CCR.

The results from measurements on polarisation transfer in π^0 -photoproduction[81, 82] and the Compton results presented previously have all been in disagreement with HHC.

In short the transition to pQCD, in fact pQCD itself, is not yet fully understood and more work and data are needed. This will be discussed further at the end of this thesis in Section 5.3.

¹³Coherently.

Chapter 2

Experimental Setup

“The strongest argument proves nothing so long as the conclusions are not verified by experience. Experimental science is the queen of sciences and the goal of all speculation.” -Roger Bacon

The Real Compton Scattering(RCS) experiment, E99-114[83], ran at the Thomas Jefferson National Accelerator Facility in January and February of 2002. This experiment, which was performed in Hall A, was primarily designed to measure the differential cross section of Compton scattering $\gamma + p \rightarrow \gamma' + p'$ [54] over a range of kinematic points and the polarisation transfer to the proton[52] at a single kinematic point. The ranges covered for Mandelstam variables t and s were $1.64 - 6.46 \text{ GeV}^2$ and $4.82 - 10.92 \text{ GeV}^2$ respectively, so the kinematic range was quite extensive. The experiment also collected data on π^0 -photoproduction, $\gamma + p \rightarrow \pi^0 + p'$, and it offers an additional, although analogous, set of experimental observables: the differential cross section and the polarisation transfer to the proton.

The experiment utilised an electron beam with an intensity varying between $5 \mu\text{A}$ and $60 \mu\text{A}$ which impinged on a 6% radiation length copper radiator. The resulting mixed beam of electrons and bremsstrahlung photons was allowed to directly hit the 15 cm cryotarget of liquid hydrogen. Scattered electrons and photons, and photons from π^0 decays were detected in the RCS photon spectrometer. Coincident recoiling protons were detected in the Hall A High Resolution Spectrometer (HRS). The setup is presented in Fig. 2.1. The photon spectrometer was built specifically for this experiment and its main part was the calorimeter which is an array of lead

glass blocks. Lead glass is an excellent material for detection of electromagnetically interacting particles and was organised in a highly segmented array to allow good spatial resolution and high-rate capability. The HRS referred to is the standard Hall A Left spectrometer which was set up for hadron detection. Another important addition to the setup was a deflection magnet installed between the target and the photon spectrometer. The capability to differentiate between the various reaction channels was improved by deflecting the scattered electrons and making an angular correlation with the proton detected in the HRS. This chapter presents the experiment, the experimental facility and the details of the various pieces of equipment used in the E99-114 experiment.

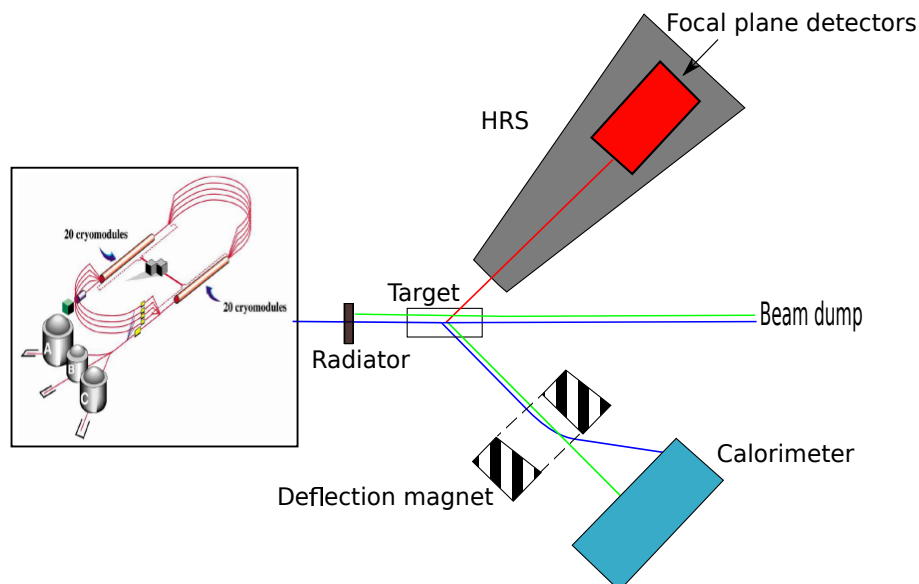


Figure 2.1: Overview of the experimental setup in Hall A. The insert shows an overview of the accelerator site and a larger version, including the recent upgrades, can be found in Fig. 2.3. A 3D model of the HRS is found in Fig. 2.2. Blue: electron; green: photon; red: proton. Picture is not to scale.

2.1 Kinematics

This section presents an overview of the most pertinent types of data collection runs that ran during the experiment. For each kinematic point data were collected with variations on target type, deflection magnet setting, HRS momentum($P_{End,Off}$) and angle($\theta_{End,Off}$) settings, distance between target and calorimeter surface($CaloD$)

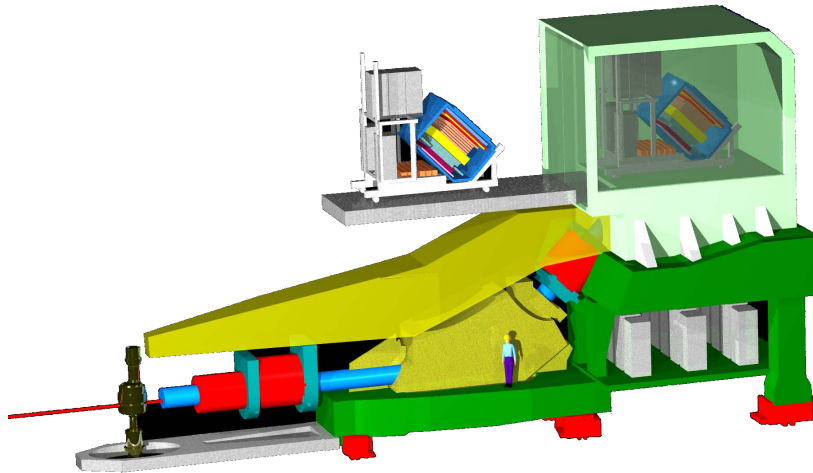


Figure 2.2: 3D-model of the HRS including the detectorstack and magnets. The quadrupole magnets are shown in red and the dipole magnet in yellow. Picture from [84].

and calorimeter angle($Calo\theta$). The HRS setting defines different windows on the incoming beam energy: one for electron runs covering the endpoint of the electron energy spectrum and an off-endpoint setting for the production runs. In summary the important types of data collection runs were:

1. HRS optics data collected with a carbon foil target to check the performance of the transfer matrix, both at endpoint and off-endpoint HRS settings.
2. Electron scattering data gathered without the radiator and the deflection magnet turned off at the endpoint HRS setting.
3. The production data collected with radiator mounted and with the deflection magnet turned on.

A complete listing of the kinematics can be found in Table 2.1 with the kinematic point for the polarisation transfer measurement in boldface. This thesis will make reference to the two HRS settings per kinematic point as endpoint and off-endpoint and to the beam energy groups as 2-, 3-, 4-, or 5-pass data; corresponding to the accelerator configurations that were used, specifically the number of turns around the accelerator. In addition, data were also collected with the purpose of optimising

the transfer coefficients for the HRS. These data were collected at two kinematic settings, indicated by italics in Table 2.1, and differed from the standard runs in that the polarity of the HRS magnets was reversed to accept electrons, a sieve slit was situated in front of the entrance window to the HRS and the carbon foil target was used.

2.2 Jefferson Laboratory

The Thomas Jefferson National Accelerator Facility, TJNAF, Jefferson Laboratory, or simply J-lab[84–86], is a US national laboratory funded through the U.S. Department of Energy (DOE) and located in the town of Newport News on Virginia’s coast. Its purpose is precision tests and probing of QCD and the associated strong force through the use of a high intensity and highly polarised electron beam. In order to do so the facility is necessarily at the forefront of the intensity and polarisation frontier.

The facility houses four experiment halls, the original halls A, B and C, and the new hall D, which is currently¹ being commissioned. Hall A is the largest in size and its standard detector equipment include two large magnetic spectrometers, the High Resolution Spectrometers. A related detector is the High Momentum Spectrometer located in the second largest hall, hall C, which like its hall A counterparts has a large dipole as its main component. Halls A and C offer the widest range of experimental options in terms of reconfigurability. The smallest hall, B, housed the CLAS² 4π -detector, which is now being replaced by CLAS12. Due to its greater acceptance, hall B runs with a lower intensity beam compared to hall A and C, typically tens of nA in contrast to tens of μ A.

2.2.1 The Continuous Electron Beam Accelerator Facility

The heart and soul of J-lab is the Continuous Electron Beam Accelerator Facility(CEBAF). The original design goal of the accelerator was a beam energy of 4 GeV,

¹As of the 15th of April 2014

²CEBAF Large Acceptance Spectrometer.

| | E GeV | Calo D (m) | Calo θ | HRS θ_{End} | HRS P_{End} (GeV/c) | HRS θ_{Off} | HRS P_{Off} (GeV/c) |
|------------|--------------|-----------------|---------------|--------------------|--------------------------|--------------------|--------------------------|
| 2A | 2.341 | 12.0 | 46 | 33.97 | 1.711 | 35.68 | 1.556 |
| 2B | 2.341 | 7.1 | 56 | 28.28 | 1.951 | 29.824 | 1.779 |
| 2C | 2.341 | 5.2 | 79 | 19.14 | 2.322 | 20.285 | 2.129 |
| <i>3A*</i> | <i>3.478</i> | <i>14.4</i> | <i>31</i> | <i>16.91</i> | <i>2.990</i> | – | – |
| 3A | 3.478 | 14.4 | 31 | 37.44 | 1.928 | 39.08 | 1.768 |
| 3B | 3.478 | 10.0 | 39 | 30.95 | 2.332 | 32.46 | 2.142 |
| 3C | 3.478 | 7.9 | 45 | 27.14 | 2.586 | 28.54 | 2.380 |
| 3D | 3.478 | 6.2 | 57 | 21.36 | 2.981 | 22.53 | 2.752 |
| 3E | 3.481 | 5.7 | 65 | 18.43 | 3.176 | 19.47 | 2.939 |
| 3F | 3.478 | 5.3 | 75 | 15.47 | 3.362 | 16.36 | 3.118 |
| <i>4A*</i> | <i>4.615</i> | <i>18</i> | <i>90</i> | <i>14.57</i> | <i>4.000</i> | – | – |
| 4A | 4.615 | 18.0 | 22 | 40.97 | 1.943 | 42.58 | 1.789 |
| 4B | 4.615 | 16.4 | 26 | 36.17 | 2.290 | 37.73 | 2.109 |
| 4C | 4.615 | 13.1 | 30 | 32.21 | 2.611 | 33.691 | 2.407 |
| 4D | 4.615 | 10.1 | 35 | 28.16 | 2.970 | 29.53 | 2.741 |
| 4E | 4.615 | 7.9 | 42 | 23.74 | 3.391 | 24.95 | 3.137 |
| 4F | 4.615 | 6.9 | 50 | 19.90 | 3.769 | 20.96 | 3.496 |
| 4G | 4.615 | 6.2 | 57 | 17.27 | 4.025 | 18.21 | 3.742 |
| 4H | 4.615 | 5.6 | 66 | 14.57 | 4.278 | 15.38 | 3.987 |
| 5A | 5.754 | 18.0 | 20 | 38.47 | 2.311 | 40.01 | 2.133 |
| 5B | 5.754 | 18.0 | 23 | 35.78 | 2.550 | 36.03 | 2.462 |
| 5C | 5.754 | 14.5 | 26 | 31.25 | 3.002 | 32.66 | 2.772 |
| 5D | 5.754 | 11.4 | 30 | 27.60 | 3.410 | 28.91 | 3.154 |
| 5E | 5.754 | 9.5 | 34 | 24.62 | 3.772 | 25.83 | 3.494 |
| 5F | 5.754 | 8.8 | 37 | 22.72 | 4.031 | 23.86 | 3.722 |
| 5G | 5.754 | 8.1 | 41 | 20.05 | 4.298 | 21.59 | 3.992 |
| 5H | 5.754 | 8.1/7 | 41/46 | 20.66 | 4.280 | 19.22 | 4.280 |

Table 2.1: The Kinematic points. 3E (bold) was the point used for the polarization transfer analysis[52] and 4A* along with 3A* (italics) are the points used for the HRS optics calibration. The kinematic points are grouped into 2-, 3-, 4- and 5-pass data given by the number of turns around the accelerator necessary to reach the desired energy. The endpoint setting of 5H is a special case due to the upper limit of the HRS momentum acceptance.

but over the course of construction and operation it was eventually able to reach close to 6 GeV. The accelerator is, at the moment of writing³, going through the final stages of the upgrade to produce a higher beam energy and the beam is now reaching the hall at just over 6 GeV. Following this upgrade it will reach 11 GeV for the three existing experimental halls and 12 GeV for the newly constructed Hall D. An outline of the accelerator, including upgrades, is presented in Fig. 2.3.

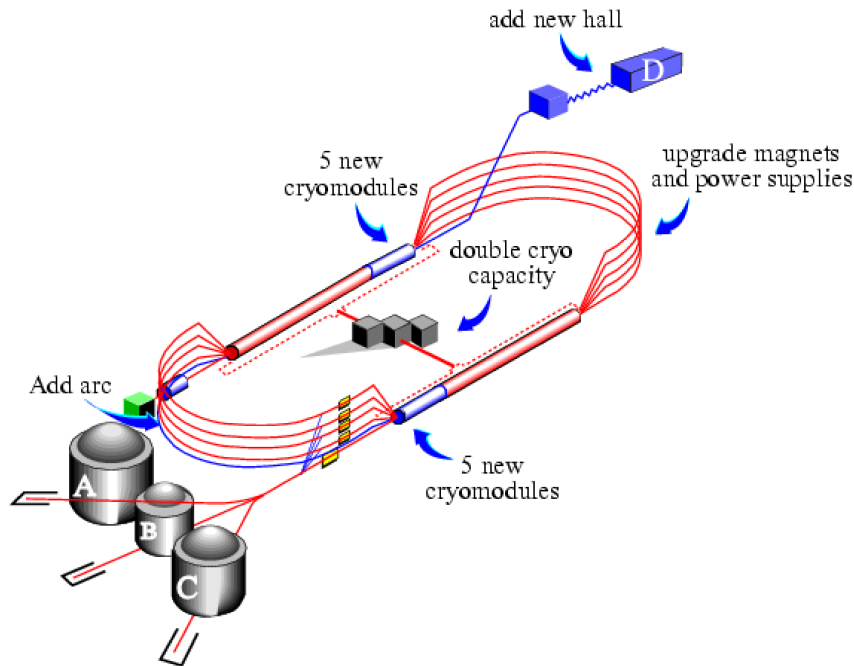


Figure 2.3: Overview of the Continuous Electron Beam Accelerator at Jefferson Laboratory including recent upgrades.

The electrons originate in the injector where, by shining with a 499 MHz polarised laser on a strained GaAs source, polarised electrons are extracted from the source and injected into the main accelerator cycle. To create all three beams simultaneously, multiple lasers are used. This produces in effect three sub-beams that are separated by one phase of the LINAC RF. The main accelerating part consists of two straight sections of LINACs and two recirculation arcs of high power bending and focusing magnets. The LINACs are superconducting Niobium cavities operating at a Radio Frequency (RF) of 1.5 GHz. They are at the very forefront of accelerator technology. In a room-temperature LINAC eddy currents in the Cu cavities cause

³Summer 2014.

heating, which effectively constrains operation to either limited voltage gradients or a non-continuous beam. In contrast to room-temperature cavities superconducting ones dissipate a very small amount of the supplied power thanks to the non-existing resistance. This allows a continuous wave(CW) operation of the LINACs and the electron bunching is, because of this, only limited by the injector and the output selector and thus allows an extremely tight bunch structure making the beam effectively continuous. The cavities are cooled to superconducting temperatures, around 2 K, by liquid helium. The helium itself is liquefied in the central helium liquefier and is reused as much as possible. The beam can be recirculated up to five times before the limit of the arc magnets bending capacity is reached, and each sub-beam can be recirculated independently of each other. The electron beam can thus be supplied to the three experimental halls continuously and simultaneously, with hall-dependent energy, intensity and polarisation. The final polarisation level of the accelerated electrons is higher than 80%.

2.3 Hall A: General and RCS Specific Equipment

The biggest of the three original halls is Hall A. Dominating the view inside of the hall is its two huge magnetic spectrometers, the High Resolution Spectrometers. These two spectrometers can be rotated around the centre of the circular hall, where the target is located, to detect scattered and recoiling particles at various angles. Several types of targets are readily available and include waterfall, cryogenic hydrogen, deuterium, helium and a selection of solid targets. The standard equipment of the hall also includes a multitude of high precision beam characteristics monitors, measuring the beam current, position, energy and polarisation. With the addition of a calorimeter built specifically for this experiment, this is the detector hardware used in this experiment.

2.3.1 Beamline Equipment

Two Beam Position Monitors (BPM) are used to determine the position of the incoming beam. They are located 7 m and 1 m upstream of the target. Each BPM

has four antennae and as the beam passes by, a current mirroring the RF time structure is induced in these. The relative amplitudes in the antennae depend on the distance of the beam from each antenna, thus allowing a very accurate measurement of the beam position at each BPM. Since the distance between the two BPMs is known through detailed surveys, the beam trajectory can be obtained using a simple linear extrapolation.

The current of the beam, or rather the accumulated charge, is measured by the Beam Current Monitors(BCM). They are located 25 m upstream of the target and their principle of operation is similar to the that of the BPMs. Each has a coaxial loop antenna and a cylindrical resonant cavity, the latter tuned to the natural frequency of the beam. Analogous to the BPMs the beam passing through the BCM induces a current in the antenna. The accumulated charge is calculated from this current and the beam current is the time derivative of the accumulated charge.

The energy of the beam is deduced in two ways. The first measurement occurs just downstream of the beam switch-yard. A dipole deflects the beam, and variations from its mean deflection angle of 34.4° is monitored by a set of wire scanners. The energy is calculated from knowing the deflection angle and the dipole field. The second method depends on the precise knowledge of a two-body elastic scattering process, $e + p \rightarrow p' + e'$. Silicon strip detectors measure the tracks of recoiling protons generated as the beam passes through a polyethylene foil. Calculating the kinematics⁴ of the reaction gives the incoming beam energy. Combining the results from these two techniques makes it possible to evaluate the energy of the beam to a relative precision of $2 \cdot 10^{-4}$.

The final important beam parameter for this experiment is the polarisation of the beam since the polarisation of the photons from the bremsstrahlung process depends on it directly. This is crucial to measure the polarisation transfer but is of no importance for the extraction of the cross section⁵. To measure the beam polarisation a Møller polarimeter is used. This is an intrusive device which utilises

⁴In analogue to that done for the proton detected in the HRS.

⁵The unpolarised cross section.

the asymmetry of Møller scattering where polarised beam electrons scatter off atomic electrons in a magnetised Fe foil. A small magnetic spectrometer detects both resulting electrons and the asymmetry of the cross section obtained depends on the longitudinal component of the beam polarisation. This asymmetry together with the magnetisation of the target allow one to compute the beam polarisation. This method has a relative error of about 3% mostly attributed to the uncertainty in target magnetisation.

The high intensity of the beam could cause damage, by overheating, to the target and affect the uniformity of the target material if it were constantly aimed at the same transverse position of the target. Such damage to the target would ultimately cause a reduction in luminosity. To avoid this the beam is rastered by two dipole magnets. The slow raster redirects the beam in a rectangular pattern across the target entrance. The fast raster oscillates the beam striking point, vertically and horizontally at frequencies of 17 kHz and 24 kHz, around the point defined by the slow raster.

2.3.2 Target and Radiator

In the experiment E99-114 the main target was a liquid hydrogen target[87] with an attached copper radiator. Complementary targets, for offline calibrations, were also implemented in this experiment. These include a carbon foil target for HRS optics calibration, a liquid hydrogen target without a radiator for calibration of the calorimeter and an empty “dummy” target. In order to minimise the number of hall accesses needed during the experimental run period, these targets were mounted on a target ladder. This target ladder could be remotely moved vertically to align the desired target cell with the beam. The ladder was enclosed in a vacuum chamber connected to the beam pipe. The vacuum chamber has two 0.34 mm thick aluminium windows covering the possible angular positions of the spectrometers, $\theta \in (12.5^\circ - 165^\circ)$. The hydrogen was contained in an aluminium cylinder, 15 cm in length and 63.5 mm in diameter. The walls of the container were designed to minimise the background contributions from the target and smearing effects such as multiple Coulomb scattering. They would also need to stand the pressure from the

pumping system versus the vacuum outside it. In the end it was manufactured with a $71\ \mu\text{m}$ thick upstream window, a $102\ \mu\text{m}$ thick downstream cap and $178\ \mu\text{m}$ thick target side walls.

The beam presents a significant heat load on the target, especially at such high beam currents as were utilised in this experiment. In fact, boiling of the target material is a real risk and a greatly undesired one⁶ as this might perturb its uniformity, decrease density and in the worst case cause damage to the target. The raster distributed the heat load across the face of the target and the target hydrogen was also recirculated in a complex system of cooling fins to improve further the uniformity of the heat exchange.

The cross sections of the processes of interest in this experiment are generally very small at the energies employed in this experiment. Together with a small combined experimental acceptance this could lead to undesirably low counting rates. Therefore, a high photon flux was a necessity and several steps were taken to achieve this. First, the radiator was purposely placed close to the target cell. Second, the radiator itself was made relatively thick and of a material with high Z . The total thickness of the copper radiator was $0.81\ \text{g}/\text{cm}^2$, equivalent to 6.2% of copper's radiation length. The choice of copper as the radiator material was based on knowledge of the process of "external" bremsstrahlung which is a well understood interaction mechanism. In the 1970s J.L. Matthews and R.O. Owens[88], published a detailed description for the calculation of bremsstrahlung spectra. This calculation method has been an extensively used, and verified, tool in a range of experiments such as Compton scattering, pion photo production and photo disintegration processes.

A result of setting up the experiment in this way is that the beam on target will be a mix of electrons and photons. The ratio of photons to electrons is lowest close to the high energy end point of the bremsstrahlung spectrum. However, since the experiment studies two-body processes the setup of the spectrometer and the calorimeter defines a window of acceptance (E_{min} , E_{max}) on the spectra. The choice of the window is a compromise between the theoretical aim of high values of centre-

⁶The target actually did boil at one point during the run period. Fortunately, this only rocked the target a tiny fraction and caused no further damage.

of-mass energy and the amount of background elastic electron scattering one can allow to “pollute” the data.

2.3.3 High Resolution Spectrometer

The HRSs were constructed with the intention to be the main tools of Hall A. Initially that was the case but more recently experiments have called for more specialised equipment and detectors with a different focus. The spectrometers have a small acceptance, compared to a 4π -detector like CLAS, but have excellent momentum and angular resolution. Table 2.2 outlines the acceptance, resolution and a few other properties of the HRS. This experiment used only the left spectrometer, while the right was moved to a backward angle.

| | |
|----------------------------------|-------------------|
| Magnet configuration | QQDQ |
| Bend Angle | 45° |
| Optical length | 23.4 m |
| Momentum Range | 0.3-4.3 GeV/c |
| Momentum acceptance | $\pm 4.5\%$ |
| Momentum Resolution (FWHM) | $1 \cdot 10^{-4}$ |
| Solid Angle (Rectangular approx) | 6.7 msr |
| Solid Angle (Elliptical approx) | 5.3 msr |
| Angular Resolutions | |
| Horizontal | 0.6 mr |
| Vertical | 2.0 mr |
| Spectrometer Angle accuracy | 0.1 mr |

Table 2.2: HRS specifications.

Magnets

The spectrometer disperses incoming particles according to momentum and approach vector. This happens in a series of superconducting magnets, three quadrupole and a dipole magnet, organised as Q1-Q2-D-Q3. The dipole is the main momentum selector as it bends the particle upwards dispersively to the detector hut. The quadrupoles are focusing/defocusing elements, with Q1 focusing in the vertical and defocusing in the horizontal plane while Q2 and Q3 do the reverse. The field in

the quadrupoles is monitored by Hall probes and the dipole field is measured by observing the nuclear magnetic resonance of a probe positioned inside the dipole.

Detector package

The detector stack of the HRS is located at the focal plane of the spectrometer in a hut at the top of the HRS. This serves two purposes. First, it allows for the magnetic optics to disperse to enable the reconstruction of the incoming particles momentum and approach vector. Second, it moves the detectors away from the plane of interaction where the radiation levels are much lower so that the detectors are not overloaded and a clean signal is obtained. In principle, if one knows the optics of the HRS in full then one can recreate the particle kinematics at the target from measurements at the focal plane. To enable such a retrace the measured quantities at the focal plane must be known with great precision. A number of sub-detectors, shown in Fig. 2.4a, are used to reach this precision and they are:

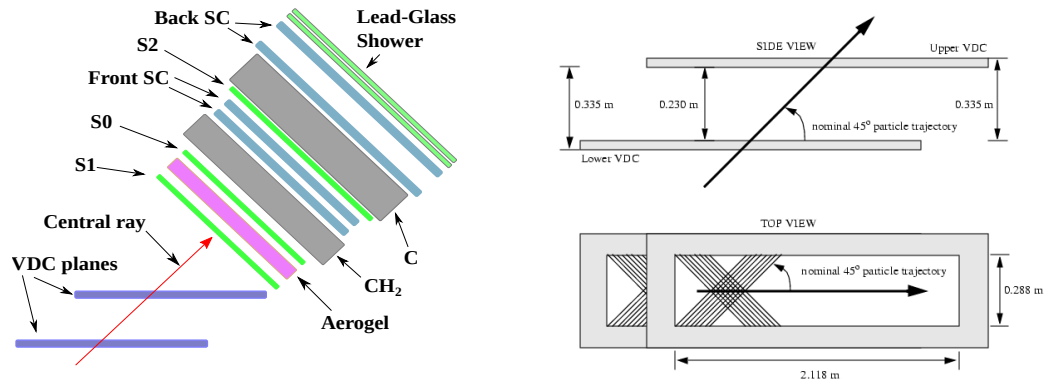
- Vertical Drift Chambers: Two chambers each with two planes of wires, track the particle as it enters the detector stack. These are the most important detector systems for determination of the particle trajectories. The VDCs sit at (the lower VDC) or near the focal plane of the spectrometer to obtain the desired resolution. This is not needed for the other non-position sensing components of the stack. The positions of the planes in relation to each other and the other detectors are presented in Figs. 2.4a and 2.4b. Note that in contrast to the other subdetectors the VDCs are tilted by 45° with respect to the central particle trajectory. All planes have 368 wires and for each plane the wires are oriented at either 45° or -45° relative to the the central particle trajectory as is seen in Fig. 2.4b. The wires are immersed in a mix of argon and ethane⁷ with a voltage of 4000 V applied to each wire. When a charged particle passes through the chamber gas it causes ionisation. The electrons from the ionisation⁸ first drift and then finally accelerate rapidly in the electric field of

⁷62% argon and 38% ethane.

⁸The ions are far too heavy and slow to contribute to the measured current.

the wires. It is the final acceleration that boosts the electrons into creating an avalanche of ionisation. This electrical pulse is amplified, passed through a discriminator to a Time-to-Digital Converter(TDC) and finally read out by the Data Acquisition System(DAQ), see Section 2.5. The perpendicular distance between the hit position and the wire is calculated from this drift time and the known electron drift velocity. In total each chamber covers an area of 240 cm by 40 cm with a sensitive area per chamber of $211.8 \times 28.8 \text{ cm}^2$.

- Scintillator planes: Three scintillator planes are the main HRS triggers. One, S0, was specific to this experiment and consisted of a single scintillator bar viewed by two PMTs. S0 was used together with the calorimeter for the coincidence trigger which is further explained in Section 2.5.1. The other two, S1 and S2, are a standard part of the detector package and operate in coincidence for triggering and timing. Each of the S1 and S2 planes have five bars viewed by two PMTs each.
- Cherenkov and shower counters: An aerogel cherenkov and a lead-glass shower counter were mounted in the detector package for particle identification purposes. The latter excels at separating electrons from hadrons but in this case was not necessary for the triggering or the analysis. The former allows separation of pions from protons, but the coincidence trigger between the HRS and the calorimeter was found to be very clean with a negligible pion background. So neither of the detectors were used in the analysis or in the trigger of this experiment.
- Focal Plan Polarimeter: See separate section 2.3.4.



(a) Overview of the HRS-left detector package used in the experiment. (b) The relative positions of the VDC chambers and planes.

Figure 2.4: HRS-left detector package used in the experiment.

2.3.4 Focal Plane Polarimeter

The Focal plane polarimeter (FPP) was installed in the detector hut alongside the standard detector package described in section 2.3.3. It was used to extract the polarisation of the recoiling proton at the focal plane. Combined with knowledge of the spin transport in the HRS magnets this was used to determine the polarisation components at the target. The polarimetry is based on measuring nucleon-nucleon scattering in an analyser material.

Proton Polarimetry

The polarimetry technique centres around the fact that the nucleon-nucleon scattering potential contains a non-zero spin-orbit term, making it sensitive to the direction of the proton spin. This causes a modulation of the cross section (σ_0), see eq. 2.1, and thus results in an asymmetry in the azimuthal scattering angle (ϕ) if the incoming protons have non-random spin directions. The polar angle (θ) affects the relative amplitude of the asymmetry since both σ_0 and the analysing power A depend on it, but the effect is symmetric. From the modulation of ϕ the polarisation's transverse components, P_x^{fpp} and P_y^{fpp} , can be extracted by fitting a sine and a cosine function. Knowing the polarisation at the focal plane and the spin transport through the HRS magnets allows one to determine the polarisation components at the target,

$$\sigma(\theta, \phi) = \sigma_0(\theta)[1 + A(\theta)\{P_x^{fpp} \sin \phi + P_y^{fpp} \cos \phi\}]. \quad (2.1)$$

In reality, scattering also occurs to a large degree by electromagnetic interaction, also known as Coulomb scattering. This interaction does not depend on the proton polarisation and is a contamination of the data sample. Fortunately, it is characterised by a narrower distribution in the polar angle compared to the strong interaction and can be suppressed effectively by choosing sufficiently large polar angles. Measuring the proton's trajectory at its entry and exit from an analyser block is the common way to use secondary scattering for polarimetry of protons and neutrons. The precision to which the transverse polarisations (P_x^n & P_y^n) can be determined in this way depends directly on A . This property is commonly referred to as the analysing power. The effectiveness of a polarimeter depends on the detection efficiency, resolution effects⁹, the scattering cross section, and most importantly on the square of the analysing power.

Polarimeter outline

The Hall A FPP is made of two pairs of straw-chambers, a 51 cm thick carbon analyser and for this experiment an additional 44 cm thick analyser block of polyethylene placed in front of the first straw chamber. The straw chambers are a detector type similar to the drift chambers. The main difference is that each wire is surrounded by a grounded "straw". In principle, a proton passing through the plane will therefore only result in a pulse in one wire which limits the resolution. Each straw-chamber consists of 6 planes of straws, 3 of which are at 45° and 3 are at -45° relative to the the central particle trajectory¹⁰. They are used to measure the proton trajectory before and after the second analyser block. Since the VDCs measure the proton trajectory into this additional block there was no need for another plane of straw chambers. The point of introducing an extra block was to increase the detection efficiency on one hand by simply using two independent polarimeters but also because

⁹Such as multiple scattering and particle misidentification.

¹⁰The same as in the VDCs, but the chambers in this case are not tilted like the VDCs.

the use of polyethylene increases the analysing power for proton momenta above 2.4 GeV/c[89]. A schematic outline of the Polarimeter setup is presented in Fig. 2.5.

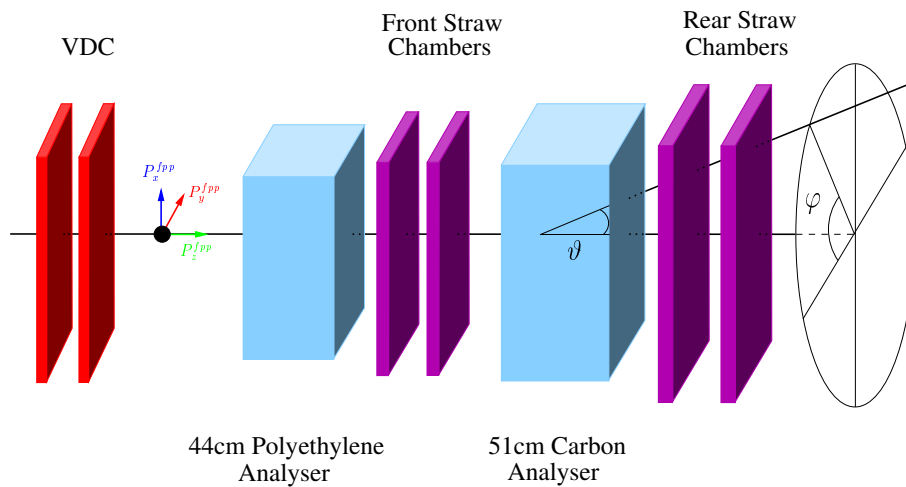


Figure 2.5: The Focal plane polarimeter as it was used in the experiment. Note that in reality the VDCs are rotated in relation to the other detectors in the focal plane and that some of the detectors present in Fig. 2.4a have been omitted.

2.3.5 HRS Optics Calibration

The VDC data contain clusters of wire signals for each VDC plane. Using these the position of the hit in each plane can be reconstructed to a high degree of precision, roughly $100 \mu\text{m}$ [90] in x and y coordinates. It is also possible to reconstruct the angles of the traversing particle but with a relatively high uncertainty. Instead the hit positions from both the VDC chambers are used to determine the angles of the trajectory with a resolution of about 0.5 mr [90]. This determines the focal plane variables, x , y , θ and ϕ , where x and $\theta \equiv dx/dz$ specify the trajectory's vertical coordinate and angle and y and $\phi \equiv dy/dz$ its horizontal coordinate and angle. z is the component along the central trajectory. The coordinate systems are further explained in Appendix A. These variables are transformed to the target coordinate system in accordance with eq.2.2,

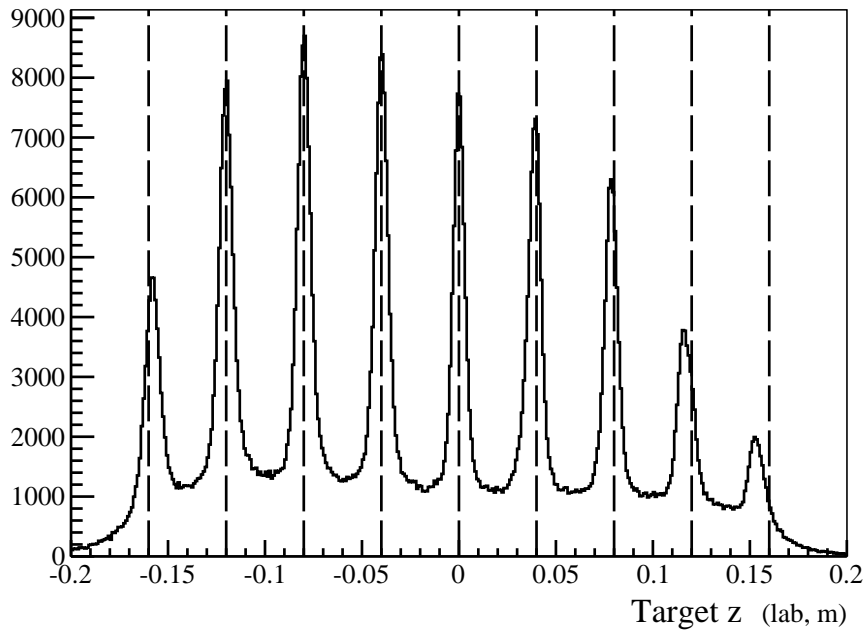
$$\begin{pmatrix} \delta \\ \theta \\ y \\ \phi \end{pmatrix}_{tg} = \begin{pmatrix} A_{\delta \leftarrow x} & B_{\delta \leftarrow \theta_{fp}} & 0 & 0 \\ C_{\theta \leftarrow x} & D_{\theta \leftarrow \theta_{fp}} & 0 & 0 \\ 0 & 0 & E_{y \leftarrow y_{fp}} & F_{y \leftarrow \phi_{fp}} \\ 0 & 0 & G_{\phi \leftarrow y_{fp}} & H_{\phi \leftarrow \phi_{fp}} \end{pmatrix} \begin{pmatrix} x \\ \theta \\ y \\ \phi \end{pmatrix}_{fp} \quad (2.2)$$

where δ is defined as $\delta \equiv (P_p - P_{central})/P_{central}$. Transverse target positions cannot be determined independently of δ and must be obtained by combining y_{tg} with BPM data. The form of the transform matrix assumes perfect alignment and that the magnetic optics of the vertical and horizontal plane are independent. In practice the transformation is described using the tensor notation of eq.2.3, where Y , T , P and D are elements of the transformation tensor:

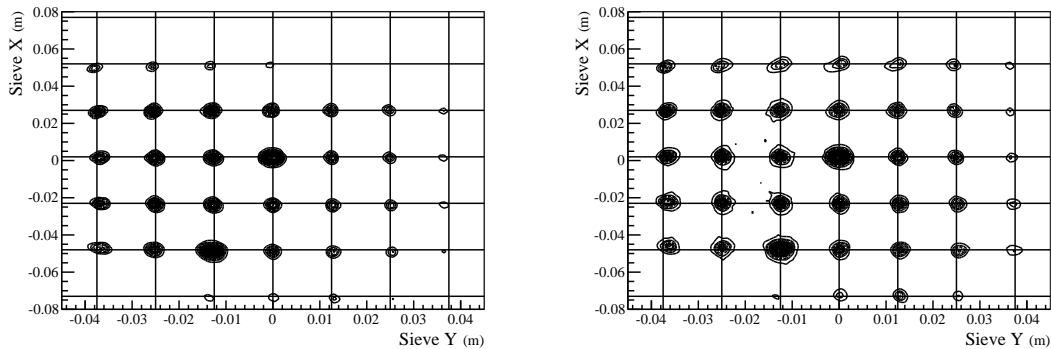
$$\begin{aligned} y_{tg} &= \sum_{i,j,k,l} Y_{ijkl} x_{fp}^i y_{fp}^j \theta_{fp}^k \phi_{fp}^l, \\ \theta_{tg} &= \sum_{i,j,k,l} T_{ijkl} x_{fp}^i y_{fp}^j \theta_{fp}^k \phi_{fp}^l, \\ \phi_{tg} &= \sum_{i,j,k,l} P_{ijkl} x_{fp}^i y_{fp}^j \theta_{fp}^k \phi_{fp}^l, \\ \delta &= \sum_{i,j,k,l} D_{ijkl} x_{fp}^i y_{fp}^j \theta_{fp}^k \phi_{fp}^l. \end{aligned} \quad (2.3)$$

This transformation tensor must be well calibrated in order to produce an accurate reconstruction of the important physics variables at the target. A procedure[91] for accomplishing this has been developed and is well proven by the Hall A collaboration. The calibration is done using dedicated runs where a sieve slit with a regular hole pattern is placed in front of the HRS entrance and a series of carbon foils are used as a target. The sieve slit pattern must be reproduced by projecting the reconstructed angles θ_{tg} and ϕ_{tg} onto the face of the HRS, see Figs. 2.6b and 2.6c. Furthermore, Fig. 2.6a demonstrates that positions of the target foils are reconstructed with a good degree of precision, especially in the ± 7.5 cm region where the hydrogen target was located. Unfortunately, the target boiled and rocked the target ladder slightly between the taking of 5-pass and 3-pass data¹¹. Although only a small shift, this adds a degree of uncertainty to the calibration. The target position is used in the sieve slit reconstruction and the great agreement in Fig. 2.6c strongly indicates that any shift in the foil position was very small.

¹¹The 3-pass data were collected last.



(a) Target foil positions from 4-pass data. The dashed lines indicate the positions of the carbon foils.



(b) Sieve slit from 4-pass calibration data. (c) Sieve slit from 3-pass calibration data.

Figure 2.6: Reconstructions of sieve slit and target foil. The two larger sieve slit holes are located at $(0,0)$ m and $(-0.0125, -0.048)$ m.

It was important to make sure that the optics reconstruction was accurate throughout the whole experiment. For this reason optics data were collected for all kinematic settings with the carbon foil target, but some without the sieve slit due to time constraints. An example of the reconstruction of the four target variables for one optics run is presented in Fig. 2.7 and the carbon foils are clearly seen.

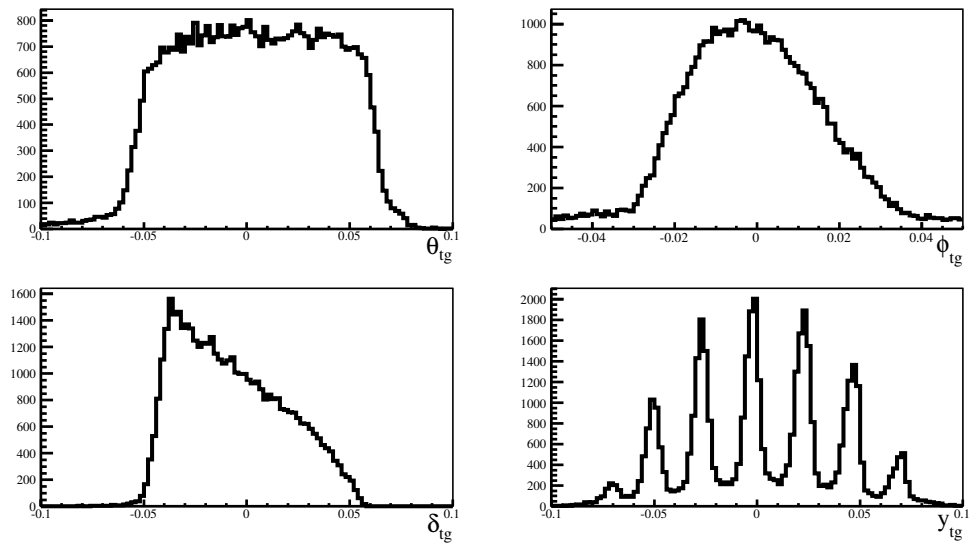


Figure 2.7: Optics target variables.

2.4 RCS Photon Spectrometer

The photon spectrometer was built specifically for this experiment. It was needed to detect the scattered electrons and scattered or produced¹² photons. The main design constraints were the need for high-rate capability, a precise coordinate determination and sufficient energy resolution to allow separation of the main experimental channels. Lead-glass (Type TF-1) was chosen as the detection material for the calorimeter part and to obtain the desired spatial resolution and high-rate capability this calorimeter was made highly segmented. The full setup also included a deflection magnet and a veto detector. The latter was not extensively used.

2.4.1 Calorimeter

The electromagnetic calorimeter, as mentioned in the last section, was made of an array of blocks of Lead-glass. High energy electrons and photons create showers in the blocks because as they traverse the block, or blocks, they undergo a series of interactions, mainly bremsstrahlung and pair production. An initial electron will

¹²Referring to the photons resulted from the decay of the photo produced π^0 .

first undergo bremsstrahlung and an initial photon will pair-produce, resulting in new particles that can themselves interact by these processes and so this chain of reactions produces a shower of electrons and photons. Each branch of this chain will eventually result in electrons and photons below a threshold, ϵ_0 , at which point ionisation becomes the dominating process. The transverse extent of the chain for the initial generations is due mostly to multiple coulomb scattering, but as the energy decreases the angular distributions for bremsstrahlung and pair production broadens and they will contribute as well. The depth, d , that the chain reaches in the material depends on the radiation length, X_0 , the initial energy E_0 and the threshold ϵ_0 . The produced electron and positron in pair production will carry on average half of the original particle's energy, and after n generations of iterations the energy will be $E_0/2^n$. So the depth of the shower will be given by eq. 2.4 because the number of generations needed to reach the threshold is given by eq. 2.5:

$$d = n \cdot X_0 = X_0 \cdot \log_2 \frac{E_0}{\epsilon_0}, \quad (2.4)$$

$$\frac{E_0}{2^n} = \epsilon_0 \text{ gives } n = \log_2 \frac{E_0}{\epsilon_0}. \quad (2.5)$$

At this point the concern is the conversion of the energy deposited in the previously described way into something that can be converted into an electrical pulse. The energy of the shower is measured by detecting Cherenkov light from the shower electrons. Cherenkov light is produced when the speed of a charged particle exceeds the speed of light in the material. So the material needs to have a refractive index that implies a speed of light that is lower than the speed of an electron with an energy of ϵ_0 . Lead glass is an excellent material as it has a short radiation length, a high refractive index and good transparency for the Cherenkov radiation. Unlike a scintillator the Cherenkov detector is insensitive to very high intensity, low energy background produced in the target and beam line. The Cherenkov signal is very sharp and thus the detector has high rate capability. A collection of properties of Lead-glass is presented in Table 2.3. From this table and eq.2.4 it is easy to calculate the expected shower depth for a given energy E_0 . For this experiment the expected shower depth was between 14 and 21 cm.

| | |
|------------------|------------------------|
| Density | 3.86 g/cm ³ |
| Refraction index | 1.65 |
| Molière radius | 4.7 cm |
| Critical energy | 15 MeV |
| Radiation length | 2.5 cm |

Table 2.3: Properties of TF-1 type lead glass.

The final calorimeter was made of 704 lead-glass blocks, each block was 40 cm deep with 4 cm sides. They were placed in a 32x22 configuration with FEU-84/3 PMTs attached at the rear end of each block to read out the Cherenkov signal. The high refractive index of lead glass means that total internal reflection is dominant but light leakage from the bar was minimised by wrapping each block in aluminised mylar and black tedlar. This was also intended to augment the spatial resolution by limiting the light to the block it was produced in and exclude light from outside. The whole matrix of blocks with its attached PMTs was situated in a light-tight housing.

2.4.2 Energy Calibration

The decoded data from the photon spectrometer, in its rawest form, are the digitised signals from the ADCs connected to each block's PMT. The charge of the signal is proportional to the energy deposited in the block. Summing of all blocks to which the shower spread allows one to calculate the total energy of the shower. However, one must first calibrate the gain for each block. This is done by using data from elastic electron-proton scattering and the calibration coefficients, C_i , for each block, i , are calculated from a minimisation of the χ^2 -function

$$\chi^2 = \sum_n \left[E_e^n - \sum_{i \in B^n} C_i (A_i^n - P_i) \right]^2, \quad (2.6)$$

where A_i^n is the amplitude for block i in event n , P_i is the ADC pedestal value for the i th block, E_e^n is the energy of event n obtained from the HRS measurement of the recoiling proton momentum-vector, B^n is the ensemble of blocks firing in event n and N is the total number of events used for the calibration. The precision of the

calibration is limited by the inherent properties of the leadglass blocks and by the resolution of E_e^n which is dominated by multiple scattering and radiative corrections, see Section 3.4, and amounts to about 2-3% depending on the kinematic point. For the calibration, and the analysis in general, it is necessary to take extra care with the blocks on the edges of the calorimeter since it is very likely that part of the shower will escape from the calorimeter completely. Therefore events are excluded from the summation if the the central block in the cluster, i.e. the block with the highest energy, is one of the edge blocks. There are several possible ways and algorithms within the *ROOT*[92] package capable of performing the minimisation. In this case a matrix inversion technique¹³ was used. The energy resolutions for kinematic points 4A and 3F are presented in fig. 2.8. 4A has one of the best resolutions because the scattered electron energy was high and it ran very early in the run period so the the calorimeter had not yet suffered from radiation damage. 3F on the other hand has one of the worst resolutions because of the relatively low electron energy and degraded Cherenkov light collection efficiency due to the high received radiation dose.

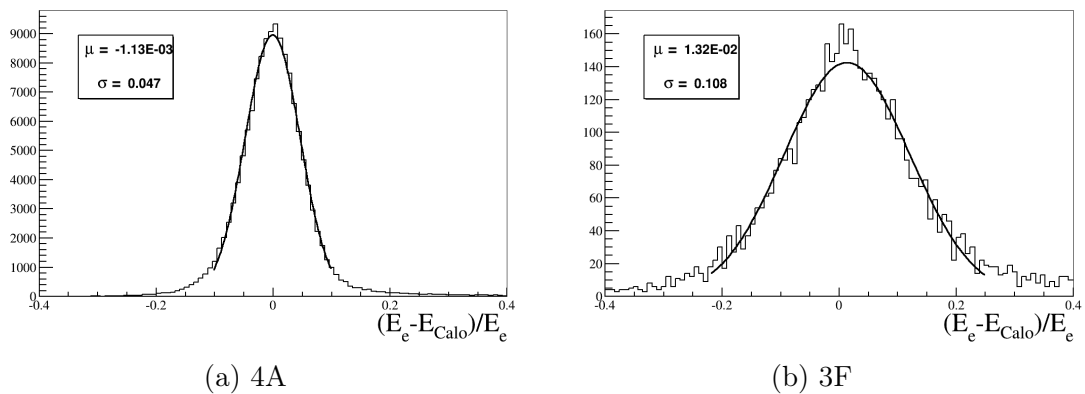


Figure 2.8: Energy calibrations for one of the best cases, kinematic point 4A, and one of the worst cases, kinematic point 3F.

2.4.3 X & Y Positions

The hit positions X_{Calo} and Y_{Calo} are calculated by taking the average of the position of the blocks involved in the shower weighted by the energy deposited as in eq. 2.6,

¹³Singular Value Decomposition, see Section 2.6 in Ref. [93].

$$X_{Calo} = \frac{\sum_{i \in B} X_i C_i (A_i - P_i)}{\sum_{i \in B} C_i (A_i - P_i)} = \frac{\sum_{i \in B} X_i E_i}{\sum_{i \in B} E_i}, \quad (2.7)$$

where A_i is the amplitude for block i , P_i is the pedestal value for the i th block, B is the ensemble of blocks firing during the event and $X_i(Y_i)$ is the block centre coordinate.

Due to the size of the calorimeter blocks the central block for each event cluster will dominate the position reconstruction. This leads to the spiky structure seen in Fig.2.9 and effectively limits the spatial resolution to about half the bar width. Fortunately, the resolution is still sufficient even for the kinematic points where the calorimeter was close to the target.

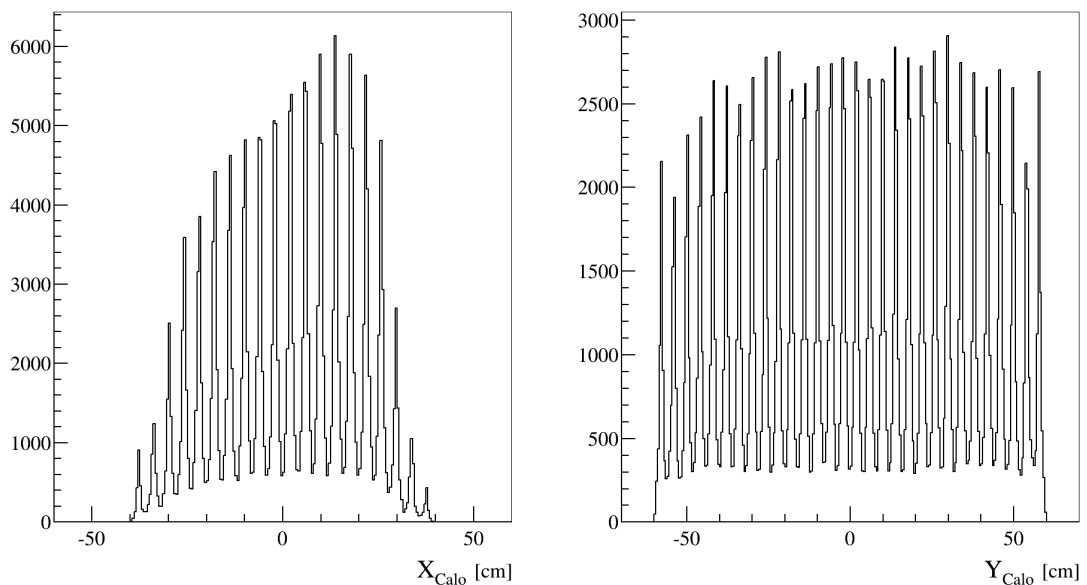


Figure 2.9: Calorimeter X & Y positions.

2.4.4 Electron-Photon Separation

A deflection magnet was placed between the target and the photon spectrometer. During production runs its purpose was to deflect the electrons in the horizontal direction. The experiment relied, as is outlined in more detail in Chapter 4 and Appendix B, on two body kinematics for the prediction of the scattered particles hit position and deflecting the electrons makes them separable from the Compton

scattering events. A simple dipole capable of causing a separation of 10 cm at the closest position of the calorimeter to the target was adequate. For analysis of the π^0 channel the deflection is useful but not absolutely necessary.

2.5 Data Acquisition System

2.5.1 Trigger and Electronics

The experiment operated with a series of triggers as outlined in Fig. 2.10. The main triggers are T7 coming from the HRS S0 scintillator plane and the calorimeter trigger T1. Together T1 and T7 form trigger T5, the coincidence trigger. Other important triggers are T8, to study deadtime, and T3/T4, to study HRS proton triggering efficiency. T2 and T6 provide supplemental pulse height calibration information for the calorimeter.

The T1 trigger is formed in a very high radiation environment and it is imperative that it is capable of rejecting the low energy background. At the same time it must not reject true events. The two extreme alternatives would be on the one hand to sum all the signals which would only require one threshold to be set. In a high radiation area this would cause a large amount of random background to enter the coincidence trigger and large, possibly unmanageable, amounts of deadtime. The other extreme would be to discriminate on the signal from each block. However, this would require more electronics and 704 discriminator levels to be set. Furthermore, the electromagnetic shower will cover several blocks and there will be instances when the particle hits close to the boundary of two(or more) blocks and using only one of the block signals in this case might result in rejection of true events. The summing used is a compromise put in place to limit the number of trigger thresholds needed. To build the trigger, the blocks are first summed in groups of 8 to form 75 *Sum8* signals. These are in turn summed into 56 *Sum32* signals. The *Sum32* signals thus form an overlapping cover of all the blocks except the outer ones. The summing scheme is outlined in Fig. 2.11. Outer blocks were not included in the trigger.

Normally the triggers from the HRS are created from the signals of two scintillator planes (S1 and S2). In this experiment the coincidence trigger(T5) was formed

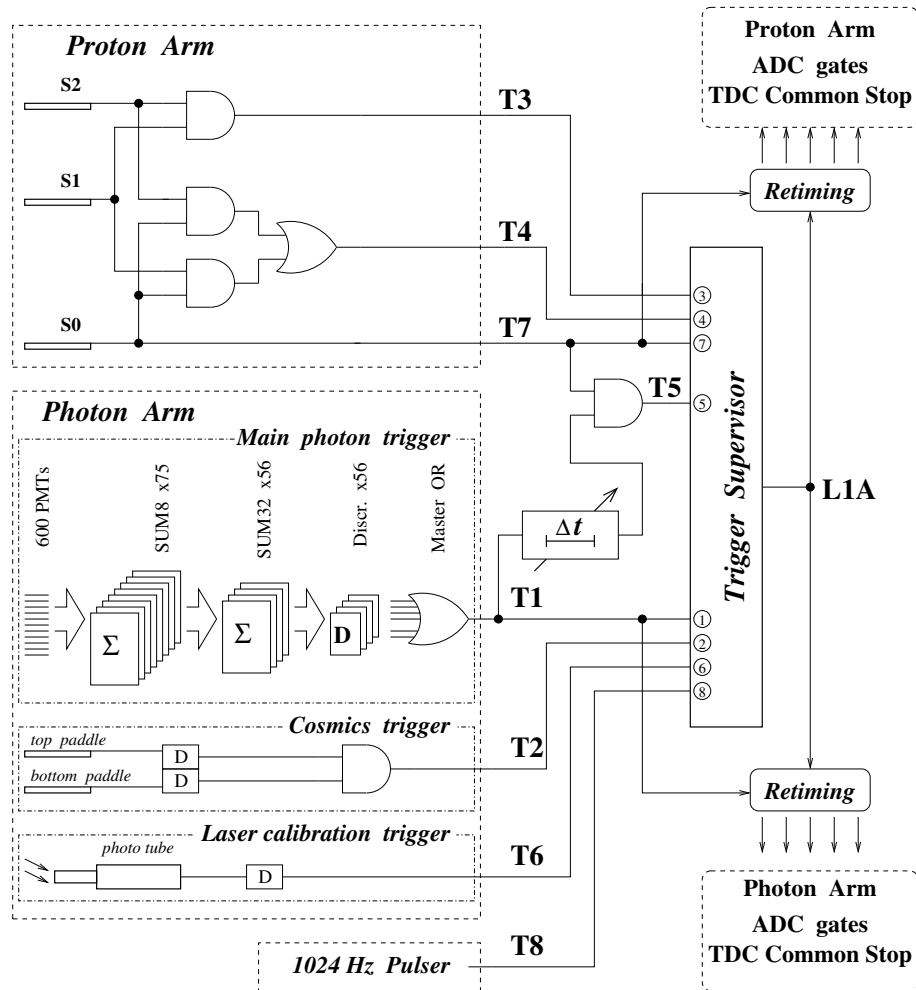


Figure 2.10: Layout of the triggering scheme for the experiment.

at the photon arm electronics which favoured a simpler and slightly faster signal for the hadron trigger. For this reason the single scintillator bar, S0, viewed by two PMTs, was used for the hadron trigger, T7.

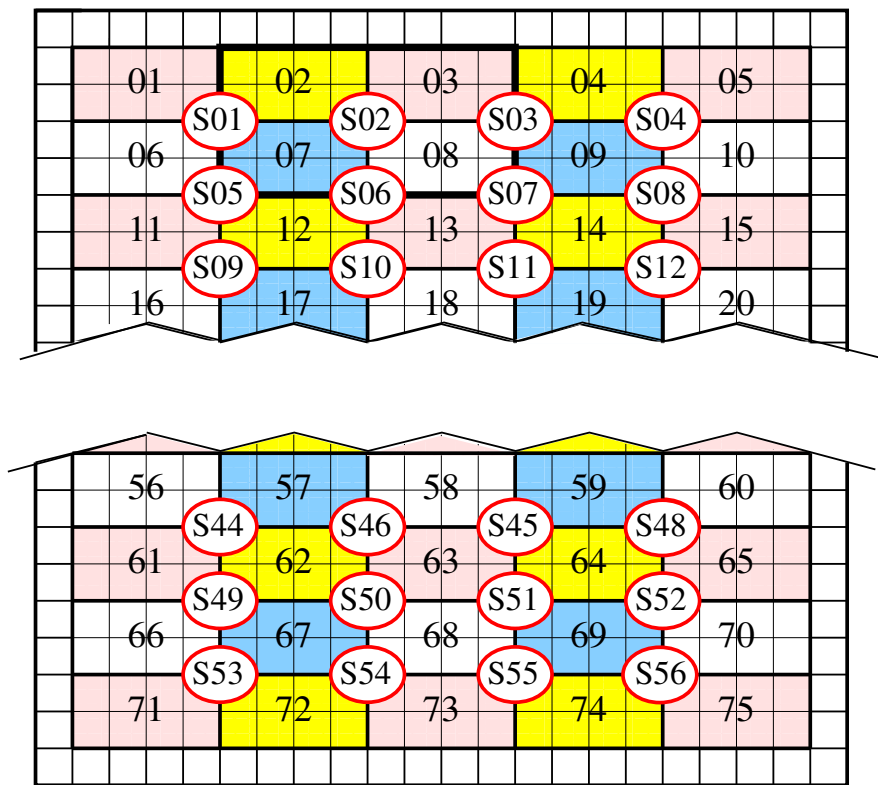


Figure 2.11: Outline of the block summing scheme for triggering.

2.5.2 Data Readout & Software

The triggers are monitored by the Trigger supervisor (TS), a VME bus module based on a Motorola MVME2400 processor. It operates as an “event selector” based on incoming triggers and trigger prescale factors. The prescale factors determine how often a certain trigger will be accepted and the corresponding digitised event read out into the data stream. For the standard production runs it was set to accept all T5 while the other triggers were prescaled to avoid undue dead time in the DAQ system. For each event selected for data readout by the Trigger Supervisor, a Level 1 Accept (L1A) signal is sent to each Readout Crate (ROC) initiating the collection of data from their ADC and TDC modules. The readout of the data from these in total thousands of detector channels is handled by a custom made readout system. The readout system is based on the CEBAF Online Data Acquisition package (CODA) which feeds the read data into the output data stream CODA files. Once all this is completed the busy flag is turned off and the TS is once again ready to accept new triggers/events.

Chapter 3

The Monte Carlo Simulation

“I do not fear computers. I fear the lack of them.” -Isaac Asimov

The detectors used in this experiment are very complex, especially the HRS. To obtain cross sections with a total uncertainty of less than 10% the detectors need to be well understood through models of their individual and collective behaviour. It was thus necessary to develop a Monte Carlo simulation(MC) to accurately normalize the results and obtain a reliable π^0 -photoproduction cross section. This chapter outlines the structure and workings of the MC, while the usage of the MC generated data in the analysis is described in Chapter 4.

The MC consists of several steps and sub-parts, outlined in Fig. 3.1 . First, beam energy profiles are calculated from theoretical models for electron energy loss, including bremsstrahlung. Cross sections are obtained for electron scattering from the Rosenbluth formula and for the Compton and π^0 channels from a fitted parametrised form. These are combined to form a distribution function from which events are sampled by the event generator. Once generated, the events are passed to simulations of the HRS and the calorimeter and finally read out as *ROOT*-files suitable for analysis in an analogous manner to the real data.

3.1 Beam Energy Profiles

The first stage of the MC is the generation of the electron and photon beam energy profiles. This includes energy loss of the electrons in the target and radiator and

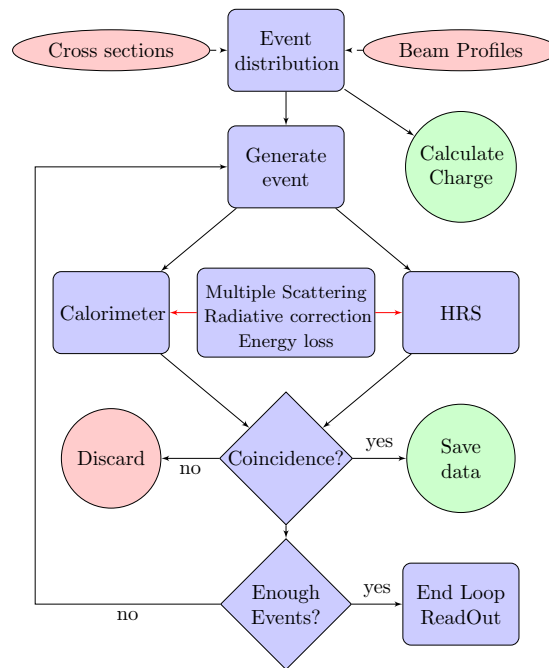


Figure 3.1: Monte Carlo flow chart

calculation of the bremsstrahlung process. The electron profile was calculated using a Geant4(G4)[94, 95] simulation of the target and the 6% Cu radiator. The photon spectrum was originally obtained from this procedure but this required the running of a huge amount of electron events to acquire a spectrum with decent statistics. Alternatively, a code(OW) originally developed by David Meekins[96], based on the work of Owens et. al.[88, 97] was used to calculate the photon flux.

3.1.1 Bremsstrahlung Calculation

Two approaches were tried and compared for the calculation of the bremsstrahlung spectra. Aside from the difference in calculation approach the underlying theory differs only slightly. They are both based on the extreme relativistic equations derived by Heitler[98], subsequently compiled by Koch & Motz[99] and Tsai[100]. The slight difference is that OW uses the intermediate screening formula while G4 uses Tsai's complete screening version¹. OW is aimed at lower energies (but still above 30 MeV and thus relativistic) and radiators of 0.01 – 0.1 radiation lengths.

¹for electron energies >1 GeV.

G4 is a full tracking monte carlo so that in principle a radiator of any thickness can be calculated accurately. G4 also includes high energy corrections such as the LPM-effect[101, 102](Landau-Pomeranchuk-Migdal) and dielectric suppression[102, 103], although these should have little effect for this application. Both G4 and OW have been validated within energy regions respectively higher[104] and lower than this experiment. These two approaches at the energies of this experiment differ substantially close to the bremsstrahlung endpoint. This is to be expected because the theory is less precise in that region. There is better agreement for the photon energy regions that are of interest for the off-endpoint setups used in this experiment, see Table 5.1 in Section 5. Plots comparing the spectra for the three main beam energies are shown in Fig. 3.2.

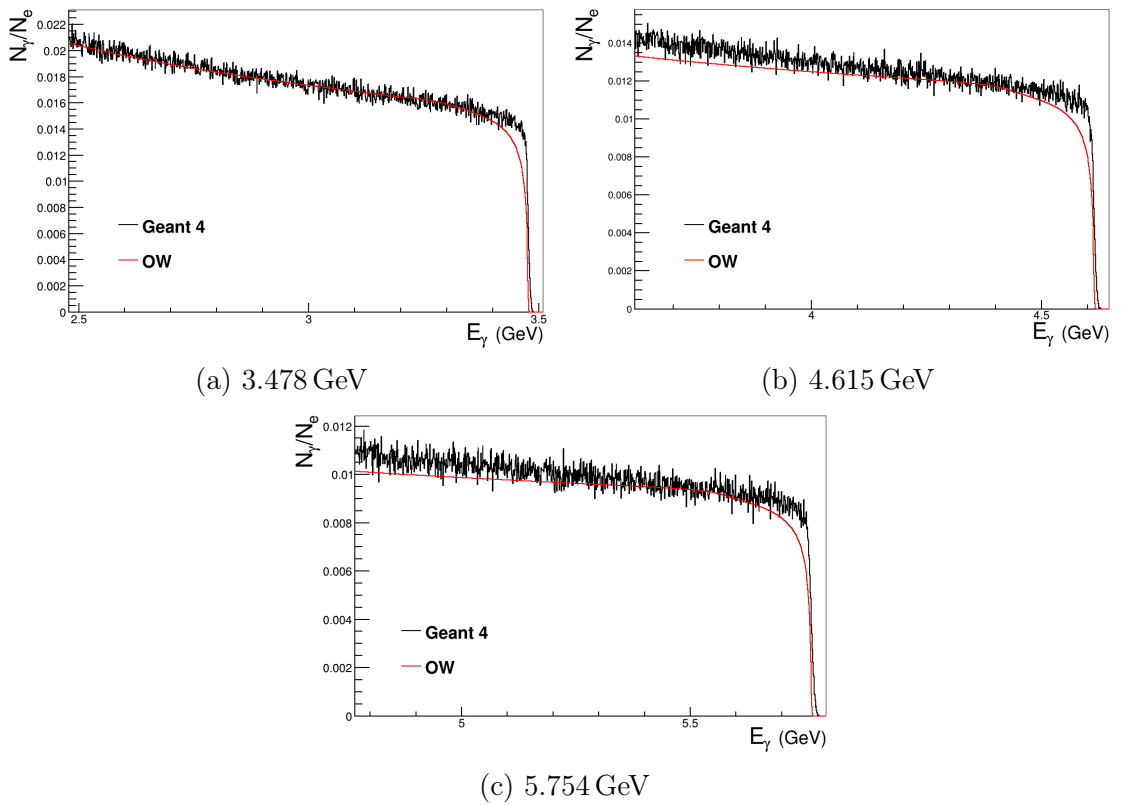


Figure 3.2: Comparison of bremsstrahlung spectra from OW calculation (red) and from Geant 4(black).

3.2 Cross Sections

The ep cross section, in the one-photon exchange approximation, is given by the Rosenbluth formula, eq.1.7, with the electromagnetic form factors of the proton, as functions of Q^2 , approximated by the Bosted fit[20], eq. 1.8. It is also necessary to take into account the higher order contributions to the reaction cross section, commonly known as radiative corrections. These corrections are often divided up into a hard and a soft part. The soft part deals with the effects of external and internal radiation of real photons, this is further described in Section 3.4.2 below. The hard part is a correction to the reaction vertex due to the exchange of additional virtual photons. This was applied directly to the cross-section by:

$$\begin{aligned} \frac{d\sigma}{d\Omega} &= \frac{d\sigma}{d\Omega_{Rosen}} \cdot (1 - \delta_{hard}) \text{ with} \\ \delta_{hard} &= 2\alpha \left[-\frac{3}{4\pi} \ln \left(\frac{-q^2}{m_e^2} \right) + \frac{1}{\pi} - \sum_i \delta_i^{vp}(q^2) \right] \text{ and} \\ \delta_i^{vp} &= \frac{1}{3\pi} \left[-\frac{5}{3} + \ln \left(\frac{-q_i^2}{m_i^2} \right) \right] \end{aligned} \quad (3.1)$$

where the first two terms of the hard correction arises from the electron-photon vertex corrections and the last term from the vacuum polarisations. The vacuum polarisation sum is over the quark and lepton(excluding the neutrinos) flavours. This follows exactly the approach in Ref.[105].

The Compton cross section was parametrised by fits to the Compton data[54] from this very experiment and the π^0 cross section was parametrised from fits to the preliminary π^0 data obtained by A. Danagoulian[53]. The form of the parametrisation was inspired by the work of A. Puckett[106] and is given by:

$$\frac{d\sigma}{dt} = C_1 \left[(1 + \cos \theta_{CM})^{-C_2} + (1 - \cos \theta_{CM})^{-C_3} \right] \left(\frac{s_0}{s} \right)^7 \quad (3.2)$$

where $C_{1,2,3}$ are the variable parameters, s_0 and s are the Mandelstam s for the data-point and the generated event respectively and θ_{CM} is the Centre-of-Mass scattering angle. The results of the fits are presented in Fig. 3.3.

The simulation included η photoproduction as an additional option. The η cross section was set equal to the π^0 in order to gauge the maximum possible contribution of η . This overestimates the η cross section by a large factor, but even with this assumption the contribution of η to the yield (see Table 5.2 in Section 5.1.1) is very small.

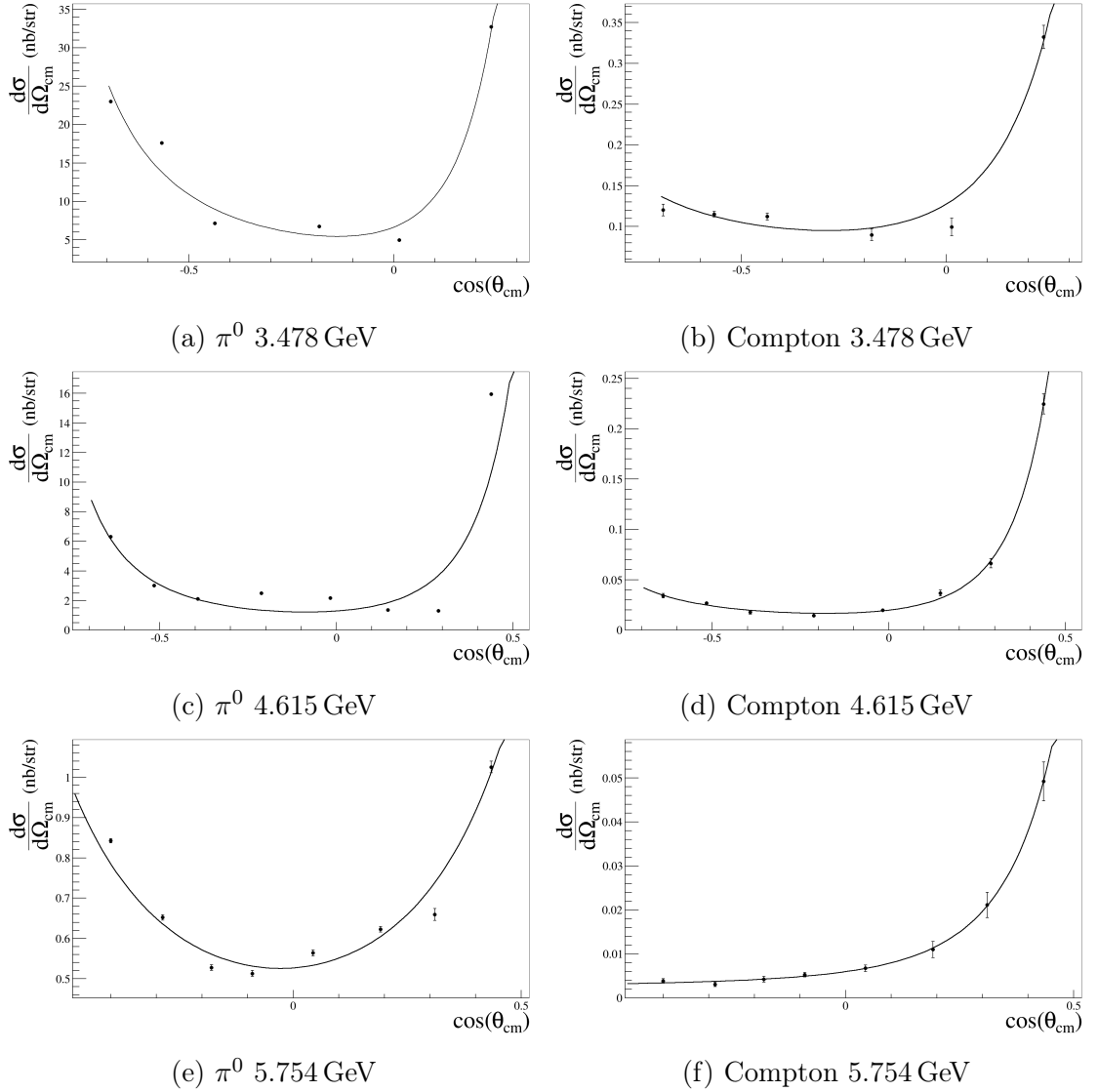


Figure 3.3: The fitted cross section parametrizations (eq.3.2) used in the Monte Carlo and the data points. Error bars are statistical only and in many cases they are smaller than the size of the marker.

3.3 Event Generator

The event generator folds the beam profile with the parametrised cross section. These convolutions are summed to give a total distribution function that represents not only the cross section but also the beam profile dependency. An example can be seen in Fig. 3.4. Events are sampled from this distribution using the inverse transform algorithm implemented for *ROOT* histograms.

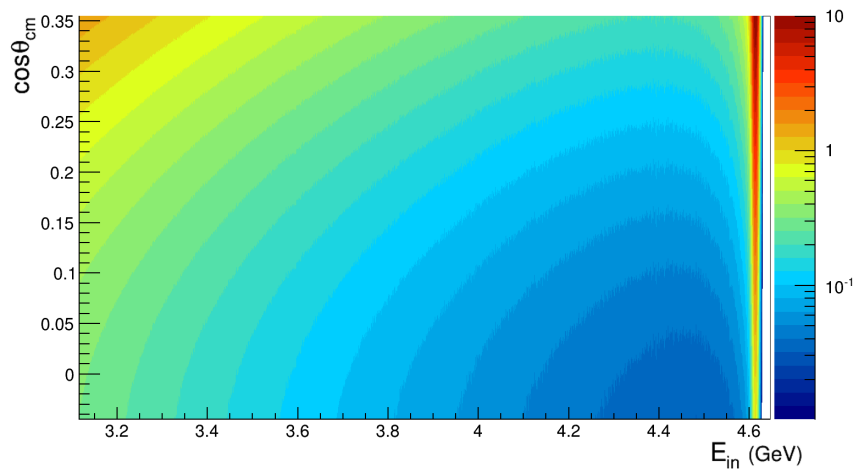


Figure 3.4: An example of a distribution function for a 4.615 GeV beam with a 6.2% radiator. The z-axis is the summed convolutions of beam profiles and cross sections, (nb/str/GeV).

3.4 Corrections

3.4.1 Multiple Coulomb Scattering

Multiple coulomb scattering is applied to all involved charged particles by assuming a Gaussian distribution with the width given by:

$$\theta_0 = \frac{13.6 \text{ MeV}}{\beta c p} z \sqrt{x/X_0} [1 + 0.038 \ln(x/X_0)] \quad (3.3)$$

where x/X_0 is the fractional radiation length, z is the charge of particle, p is the momentum and βc is the velocity. This is Molière's theory[107] as employed in

Ref.[31] and the Gaussian approximation is expected to be correct for the central 98% of the distribution.

3.4.2 Radiative Effects

The correction due to internal and external radiative effects is implemented in the Extended Peaking approximation from Ref.[105]. Using this approximation, the total radiated energy(E) factors out completely in the cross section. This way the radiated energy dependence has a simple form and it is thus easy to sample the distribution using standard inverse transform methods. The dependence is given by

$$\frac{d\sigma}{dE} \approx \frac{1}{E^{1-\lambda}} \quad (3.4)$$

where λ is the sum of the radiative strengths of the proton, the incoming and the scattered electron. The "Unextended" strengths are given by

$$\begin{aligned} \lambda_e &= \frac{\alpha}{\pi} \left[2 \ln \left(\frac{2|\mathbf{k}|}{m_e} \right) - 1 \right], \\ \lambda_{e'} &= \frac{\alpha}{\pi} \left[2 \ln \left(\frac{2|\mathbf{k}'|}{m_e} \right) - 1 \right] \text{ and} \\ \lambda_{p'} &= \frac{\alpha}{\pi} \left[\frac{p'^0}{|\mathbf{p}'|} \ln \left(\frac{p'^0 + |\mathbf{p}'|}{p'^0 - |\mathbf{p}'|} \right) - 2 \right] \end{aligned} \quad (3.5)$$

where \mathbf{k} and \mathbf{k}' are the incoming and scattered electron four-vectors, m_e is the electron mass and \mathbf{p}' is the proton four-vector. The effects due to the non-peaked strength in the electron-electron and electron-proton interference are added² giving the "Extended" strengths

$$\begin{aligned} \tilde{\lambda}_e &= \lambda_e + \frac{\alpha}{\pi} \left[2 \ln \left(\frac{|\mathbf{k}|}{|\mathbf{k}'|} \right) - \ln \left(\frac{1 - \cos \theta_e}{2} \right) \right], \\ \tilde{\lambda}_{e'} &= \lambda_{e'} + \frac{\alpha}{\pi} \left[2 \ln \left(\frac{|\mathbf{k}|}{|\mathbf{k}'|} \right) - \ln \left(\frac{1 - \cos \theta_e}{2} \right) \right] \text{ and} \\ \tilde{\lambda}_{p'} &= \lambda_{p'} \end{aligned} \quad (3.6)$$

²The article [105] chose to divide the extra strengths evenly between the electrons.

where θ_e is the electron scattering angle. The total radiated energy is distributed according to these strengths.

3.4.3 π^0 - and η -decay

The π^0 decays, isotropically in its rest frame, into two γ s with a probability of 98.8%. The Dalitz decay, $\pi^0 \rightarrow \gamma + e^- + e^+$, which is the second most common, has a probability of 0.012. In the case of the η , this decays via neutral modes ($\eta \rightarrow 2\gamma$ (39.3%) and $\eta \rightarrow 3\pi^0 \rightarrow 6\gamma$ (32.5%)) and charged modes ($\eta \rightarrow \pi^+\pi^-\pi^0$ (22.74%) and $\eta \rightarrow \pi^+\pi^-\gamma$ (4.6%)). All data are from Ref. [31]. For simplicity the simulation considers only the neutral decay modes, primarily because the event structure of a charged mode event would be similar to a neutral mode event.

3.5 Detector Simulations

3.5.1 HRS

The HRS was simulated using functions from the SIMC[108] package. This uses a transport matrix model to track the proton or electron passage through the QQDQ-magnet configuration, testing at magnet entry and exit if the particle has scattered out of the allowed path. A shortcoming is that it does not take into account the effect of hitting the walls of the vacuum system inside the dipole, only at the exit and entry. This puts a limitation on the δ range which is simulated accurately. If the simulated particle passes all magnets and collimators then it reaches the scintillator trigger planes and the VDCs. A smearing is applied to the VDC hit positions to account for the finite resolution[90] of the VDCs. The event is then reconstructed by inverting the transport process, without any acceptance checks, to give the reconstructed lab variables.

3.5.2 Calorimeter and Magnet

The calorimeter is a simpler setup to simulate. The scattered or produced e/γ is simply projected onto the surface of the calorimeter. The energy is smeared by the

resolution obtained from the calorimeter calibration, see Section 2.4.2. The position is shifted to the block centre to mimic the peak structure shown in Section 2.4.3 and smeared by an empirical function in this way

$$\begin{aligned} X_{fin} &= X_{Block} + (X_{gen} - X_{Block}) * Gaus(0, 1) \\ Y_{fin} &= Y_{Block} + (Y_{gen} - Y_{Block}) * Gaus(0, 1) \end{aligned} \quad (3.7)$$

where $X(Y)_{fin}$ is the resulting position, $X(Y)_{Block}$ is the block centre and $X(Y)_{gen}$ is the original position. The deflection of the electrons in the dipole magnet between the target and the calorimeter is simulated using a simple polynomial for the field integral given by

$$\begin{aligned} \int B \cdot dl &= 0.5328 - 0.01499 \cdot \theta_e + 2.021 \cdot 10^{-4} \cdot \theta_e^2 - 9.757 \cdot 10^{-7} \cdot \theta_e^3 \text{ and} \\ \int B \cdot dl &= 0.636 - 0.01903 \cdot \theta_e + 2.657 \cdot 10^{-4} \cdot \theta_e^2 - 1.310 \cdot 10^{-6} \cdot \theta_e^3 \end{aligned} \quad (3.8)$$

where the first one corresponds to a 500 A magnet setting and the second to a 600 A magnet setting and both are fits to data taken from Ref.[109].

Chapter 4

Data Analysis

“Sed fugit interea, fugit irreparabile tempus, singula dum capti circumvectamur amore.” -Virgil

But meanwhile it flees: time flees irretrievably, while we wander around, prisoners of our love of detail.

The analysis, and this chapter, has two main parts. The first will deal with the cross section for elastic electron scattering(ep) for endpoint kinematics. This is used to show that the normalisation method is correct and to study systematic errors. The second part presents the extraction of the π^0 -photoproduction cross section. The results are presented in Chapter 5. In both parts, comparisons between Monte Carlo(MC) and experimental data are frequent and of great importance due to the core role they play in the normalisation. Plots and histograms in this chapter are limited to the kinematic points 3A, 3E, 4D and 5D, chosen to cover small(3A), intermediate(4D & 5D) and wide(3E) calorimeter angles as well as short(3E) and long(3A) calorimeter distances. Furthermore, 4D and 5D are both roughly at θ_{cm} ¹= 90° which is of special interest. Twenty five kinematic points, each with two settings of the HRS defining the endpoint and off-endpoint beam energy windows, means that presenting all within this chapter would make it very extensive, to the point of incomprehensibility. Instead the plots for the remaining kinematics are presented in Appendix C. The coordinate systems are explained in Appendix A and all important

¹Centre-of-mass scattering angle

variables are explained in Appendix B.

The method of normalisation employed here has been used in a number of analyses performed at Hall A, for example in Ref. [53, 110]. It is sometimes referred to as the Ratio method. In this method one assumes a reasonable cross section $\frac{d\sigma_{MC}}{d\Omega}$ and calculates a MC(or normalisation) yield Y_{MC} based on this assumed cross section. Taking detector acceptances and beam flux into account the yield is given by:

$$Y_{MC} = k \cdot \frac{C_{MC}}{e} \int \frac{d\sigma_{MC}}{d\Omega} \frac{dN_{MC}}{dE} \cdot A_{MC}(\Omega, E) dE d\Omega \quad (4.1)$$

where $\frac{dN_{MC}}{dE}$ is the beam distributions, $A_{MC}(\Omega, E)$ is an acceptance function depending on the detector simulations and the cuts used², k is the target number density³, e the elementary charge and C_{MC} is the accumulated beam charge used in the Monte Carlo. The yield from the experiment (Y_{Data}) is similarly a result of the analogous equation:

$$Y_{Data} = k \cdot \frac{C_{Data}}{e} \int \frac{d\sigma}{d\Omega} \frac{dN}{dE} \cdot A(\Omega, E) dE d\Omega \quad (4.2)$$

where C_{Data} is the accumulated beam charge and $\frac{dN}{dE}$, $A(\Omega, E)$ and $\frac{d\sigma}{d\Omega}$ are the, in principle unknown, real world equivalents to those in eq. 4.1. Finally, by dividing and rearranging eq. 4.1 and 4.2, the cross section is calculated as:

$$\frac{d\sigma}{d\Omega} = \frac{d\sigma_{MC}}{d\Omega} \cdot \frac{Y_{Data} \cdot \epsilon}{Y_{MC}} \cdot \frac{C_{MC}}{C_{Data}} \quad (4.3)$$

where $\epsilon = \epsilon_{bs}/(\epsilon_{lt} \cdot \epsilon_{trigg} \cdot \epsilon_{track})$ is the combination of corrections due to livetime(ϵ_{lt}), tracking(ϵ_{track}) & triggering(ϵ_{trigg}) inefficiencies and background subtraction(ϵ_{bs}) found from the experiment data as described in Sections 4.2.1, 4.2.4, 4.3.1 and 4.3.4. In the π^0 case a correction is also made to account for electroproduction, as is explained in Section 4.3.4.

²Cuts must be identical for MC and real data.

³Number of nuclei per unit area.

4.1 Cut Definitions

The cuts used to reduce background and to select the reaction channels(Event Identification, EID) of this experiment are as follows:

R (Raw)

- **Coincidence** (Trigger=5)
- **HRS reconstructable track** (Number of reconstructed tracks=1)
- **Timing** (Kinematic point dependent)

K (Kinematics)

- **Calorimeter X&Y [cm]** ($|X_{Calo}| < 36$ & $|Y_{Calo}| < 58$)
- **Target z [m]** ($|z_v| < 0.06$)
- **Reconstructed beam energy [GeV]** (Beam energy dependent)
- **HRS fractional momentum deviation** ($|\delta| < 0.04$)

E (ep -EID)

- dE [GeV] ($|E_e - E_{Calo}| < 0.6$)
- dX & dY [cm] ($|dY| < 20$ and $|dX| < 20$)

P (π^0 -EID)

- dE [GeV] ($E_{\gamma_{\pi^0}} - E_{Calo} < \text{Kinematic point dependent}$)
- dX & dY [cm] ($dX \cdot 15 - dY^2 < -225$ and $dX < 0$)
- dX & dY [cm] ($|\sqrt{dY^2 + (dX - 5)^2}| < 40$).

The EID choices are explained in the analysis sections 4.2.3 and 4.3.3 below. R is applied in almost every case below. The exceptions are the timing seen in Sections 4.2.1 and 4.3.1 where the timing cut was omitted from the R-cut and in the estimation of the tracking and triggering efficiencies outlined in Sections 4.2.4 and 4.3.4. When only R is applied then this will be referred to as raw data, when R & K is

applied this is called reduced data and when the EID-cut (E/ P) is added this will be referred to as final data.

Note that in the analysis when comparing raw MC and experimental data discrepancies are to be expected, but these discrepancies become less significant as the kinematics are more tightly defined and the reaction channel is identified. It is necessarily so because of limitations in the MC and because the input π^0 cross section is initially an educated guess. As described in the previous chapter, the MC is limited to the central δ region of the HRS and by the photon flux calculation. *ep* data provides a cross-check for the MC and an estimation of its contribution to the systematic error is given in the next section. Furthermore, the analysis can not depend on an initial precise knowledge of the π^0 cross section. The dependence of the extracted cross section on the assumed input cross section is an important systematic error which is studied in Section 5.1.1.

4.2 Elastic Electron Scattering

The *ep* data were used for calibration, acceptance studies and as a cross-check for the MC and the normalisation procedure. As the method of the cross section extraction is so closely tied to the simulation a comparison is made between the data and the MC results for all physical variables except for timing which isn't included in the MC. In the case of electron scattering the setup itself leads to a relatively clean data set, but there are some cases where the in-target bremsstrahlung and relatively large π^0 photoproduction cross section leads to a significant amount of π^0 events in the data set. This is typical for wider angle kinematics and is clearly seen in the data plots from 3E shown in Figs. 4.4 and 4.6.

4.2.1 *ep*: Timing and Background Subtraction

The beginning and the end of this analysis relates to the timing. The first step in the analysis is to subtract obvious random contributions by identifying the prompt coincidence timing peak. In Fig. 4.1 the scaled raw timing distributions are shown along with the placement of the timing cuts and the final data. Note that the timing

cut is not applied here

The background subtraction process is described here and the same procedure is used for the π^0 photoproduction data. For background subtraction a function, consisting of a Gaussian plus a constant, is fitted to the final data but without timing cuts. The extracted yield is then corrected by subtracting the fitted constant value, integrated over the range of the timing window. The value of this correction is presented in Table 4.1 in Section 4.2.4 below.

These plots also show that the timing cuts do not remove any significant number of ep events.

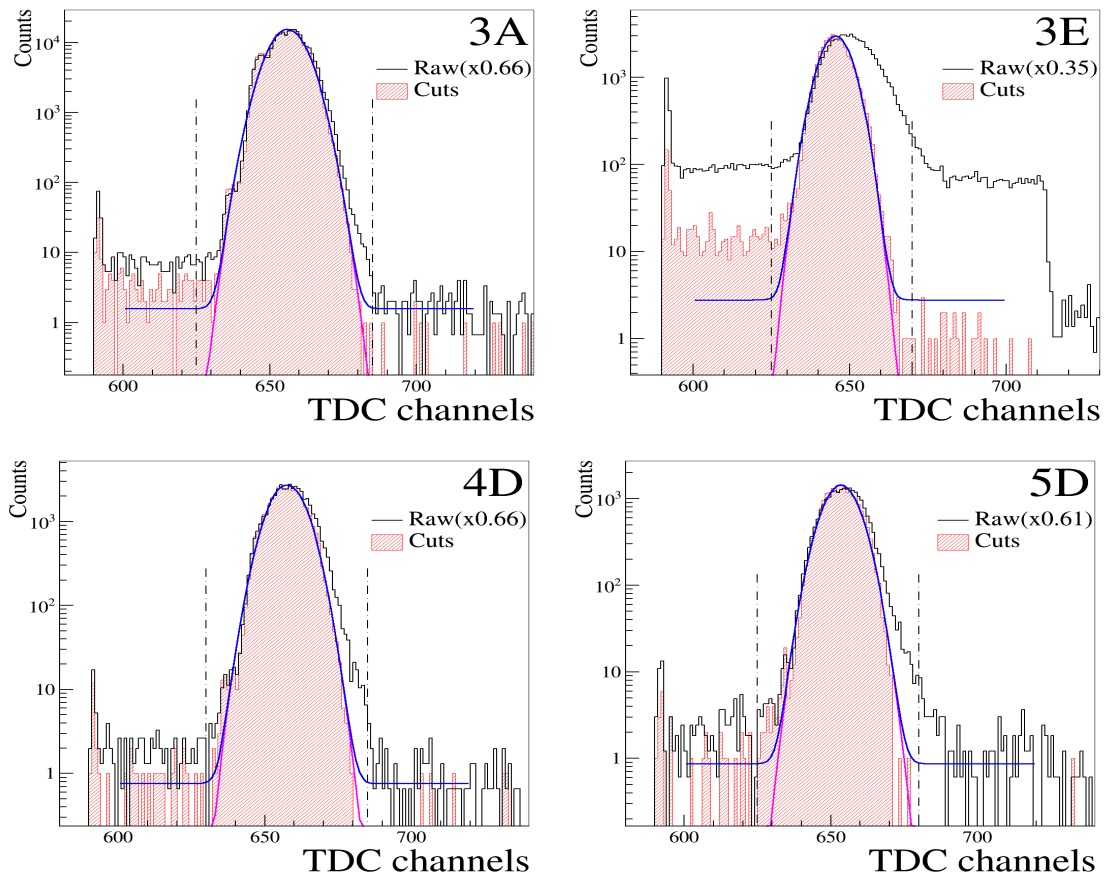


Figure 4.1: The figure shows scaled down raw timing distributions(black), the timing cuts applied(vertical dashed lines) and the timing distributions for final data(shaded red) without the timing cut. The blue curves indicate a fitted Gaussian plus constant(random background) and the purple curves indicate the Gaussian parts.

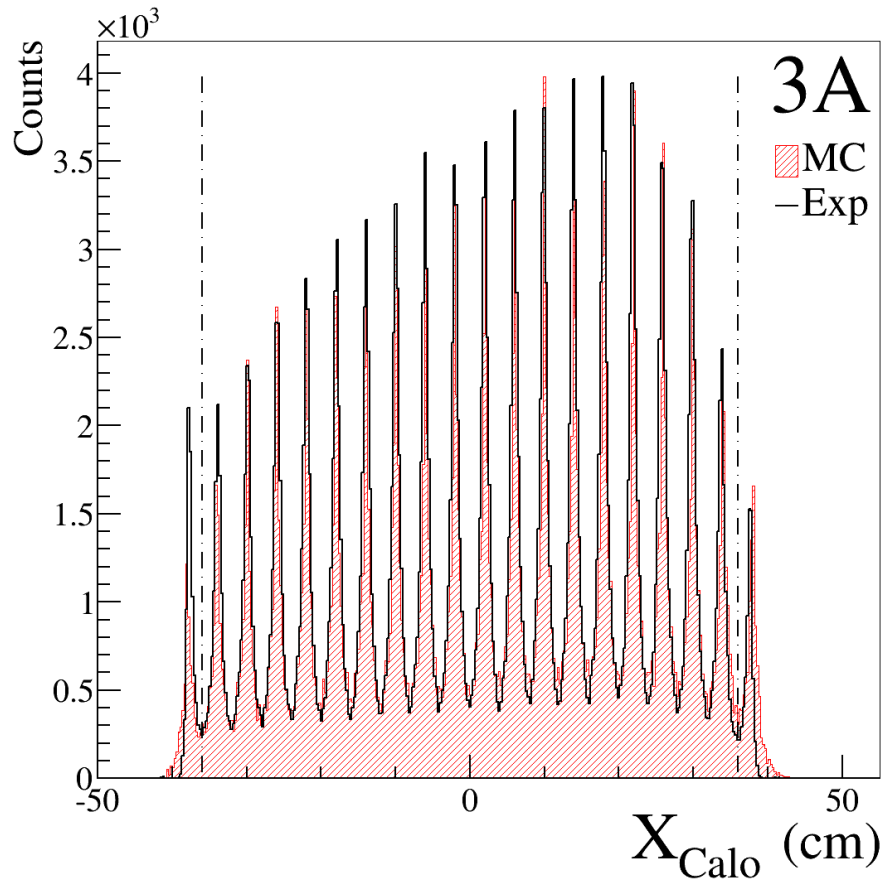


Figure 4.2: The calorimeter hit positions for 3A from raw data(black) and MC(red) with the fiducial cuts marked by vertical dashed lines.

4.2.2 *ep*: Fiducial and Kinematical Data Reduction

The next step in the data selection process is the application of fiducial cuts on the detectors. Excluding the outer elements of the calorimeter is necessary because the outer layer of elements was not included in the trigger, although it was used in the energy and position reconstruction. Figure 4.2 and Fig. 4.3 show a comparison between data and MC and also marks out the fiducial cuts applied to exclude events at the edge of the calorimeter. These cuts are the same for all kinematic points.

For the HRS one must limit the accepted range of δ because of a shortcoming in the simulation of edge effects in the dipole magnet. In Fig. 4.4 and Fig. 4.5, the raw data is shown on the left and the final data on the right. These figures also show the other three HRS variables θ_{tg} (out of plane angle), ϕ_{tg} (in plane angle) and the target z-vertex position, z_v . z_v is used to excluded effects from the target entrance and exit windows by limiting the range to ± 6 cm from the target centre($z_v = 0$).

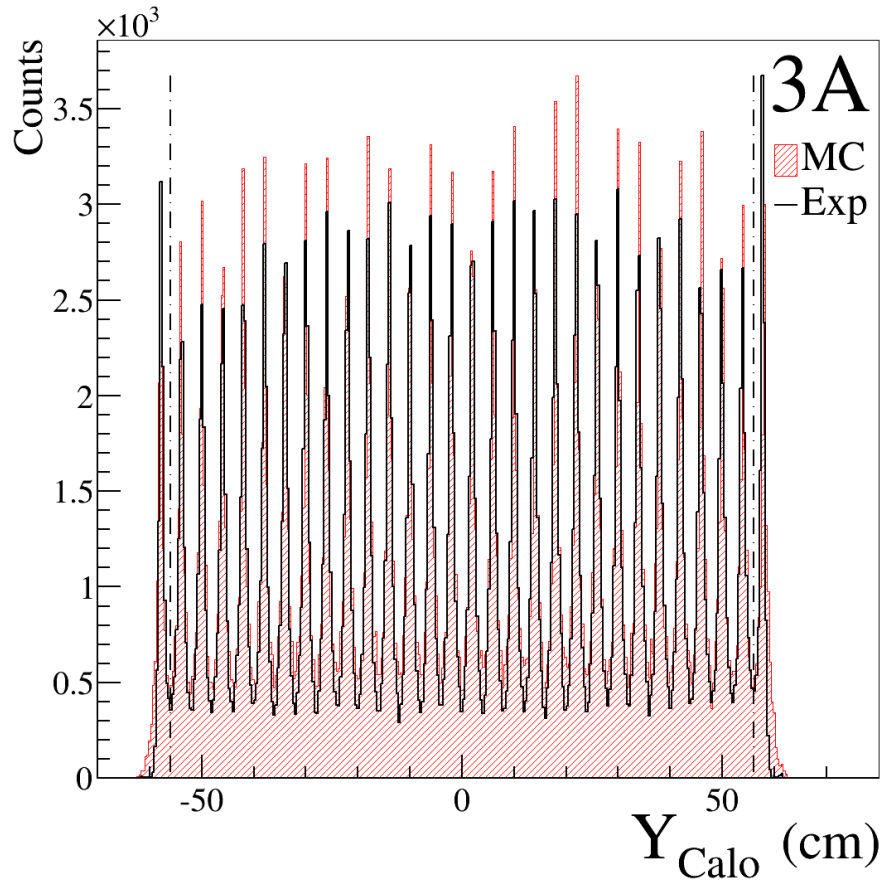


Figure 4.3: The calorimeter hit positions for 3A from raw data(black) and MC(red) with the fiducial cuts marked by vertical dashed lines.

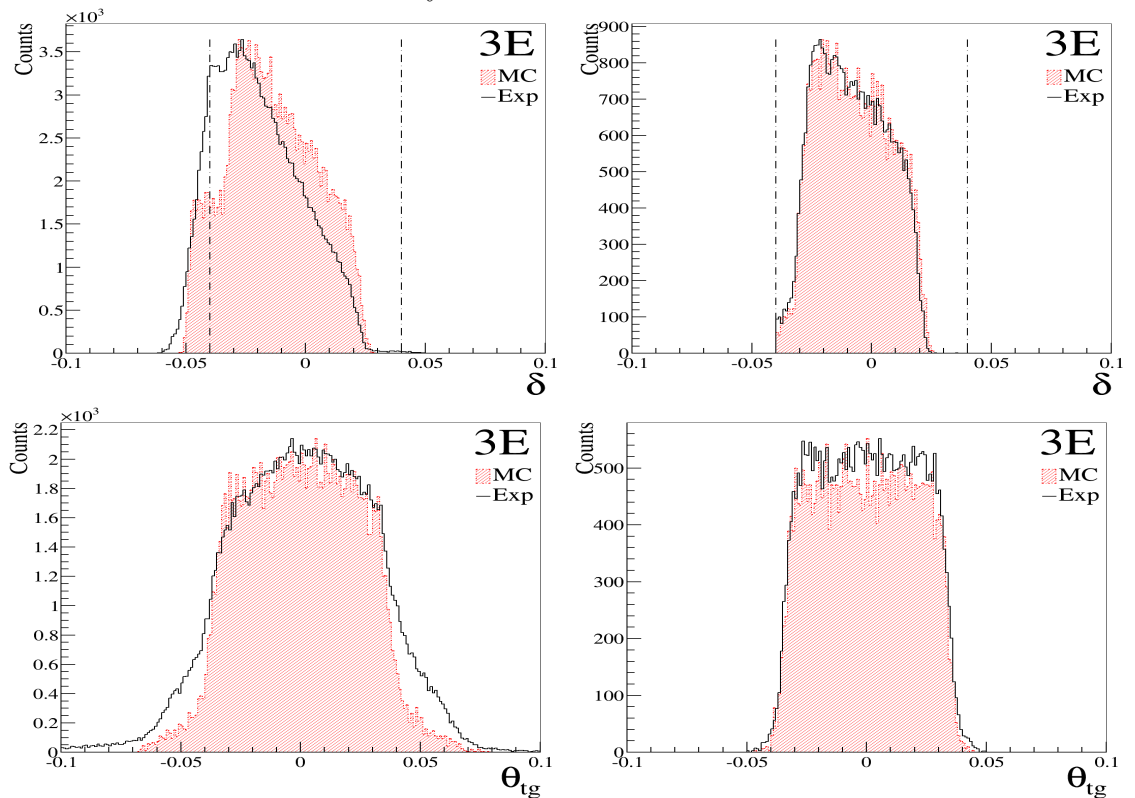


Figure 4.4: The HRS variables δ and θ_{tg} in the HRS coordinate system, including the fiducial cuts as vertical dashed lines. Raw data in the left column and final data in the right.

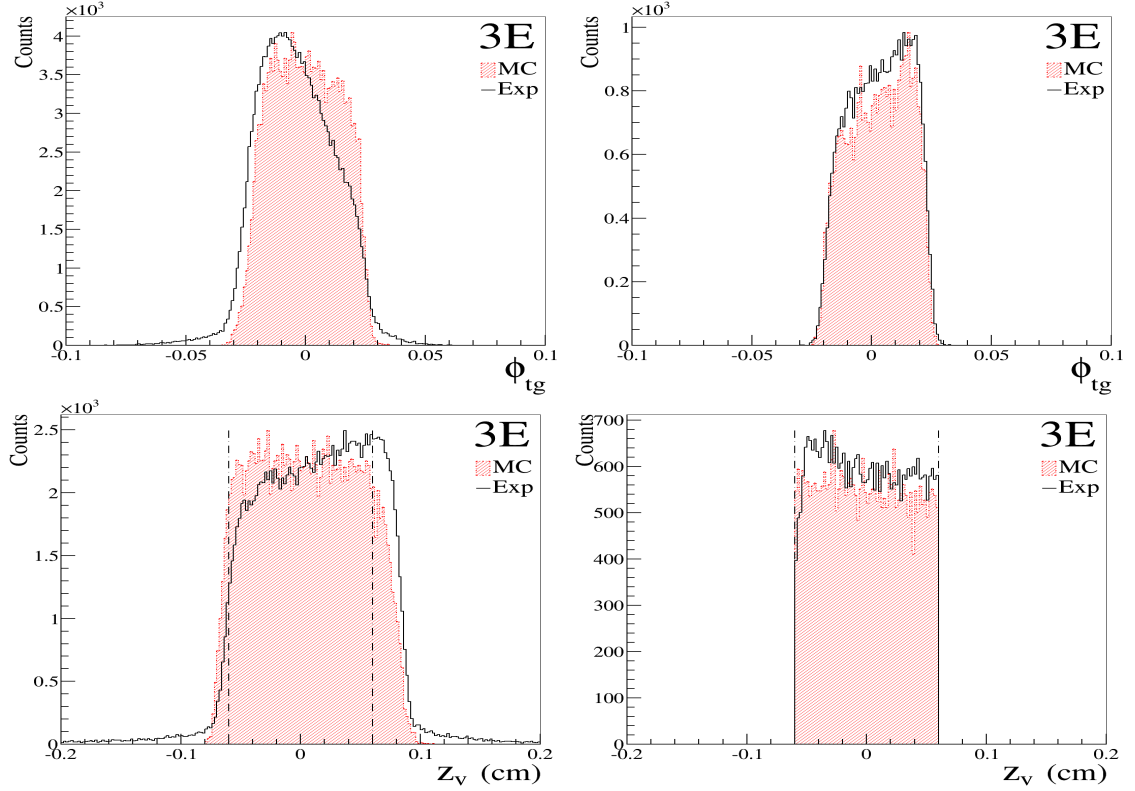


Figure 4.5: The HRS variables ϕ_{tg} and z_v in the HRS coordinate system, including the fiducial cuts as vertical dashed lines. Raw data in the left column and final data in the right.

From the HRS variables it is possible to reconstruct the beam energy $E_{in,e}$ and the scattering energy E_e assuming a two-body reaction as described in Appendix B. The reconstructed beam energy is important for it is with this, in connection with the detector angles and apertures, that the range of s and t is defined. It also works as a first identification of ep events. This approach is effectively a mirroring of the common procedure for ep scattering where the events are identified from a proton missing mass cut. The reconstructed beam energy is shown in Fig. 4.6 and 4.7, with the raw data on the left and the final data on the right. The plots of data from the 3E kinematics depict the important point on page 61 for the analysis of both the ep and π^0 cross sections. The data and MC clearly deviate from each other for the raw data, due to a combination of the incorrect δ acceptance for $|\delta| > 0.04$, and an underestimation of the π^0 cross section or underestimation of the γ flux close to the endpoint. Despite this discrepancy for the raw data, once the event type has been singled out the individual variables the MC and data show good agreement.

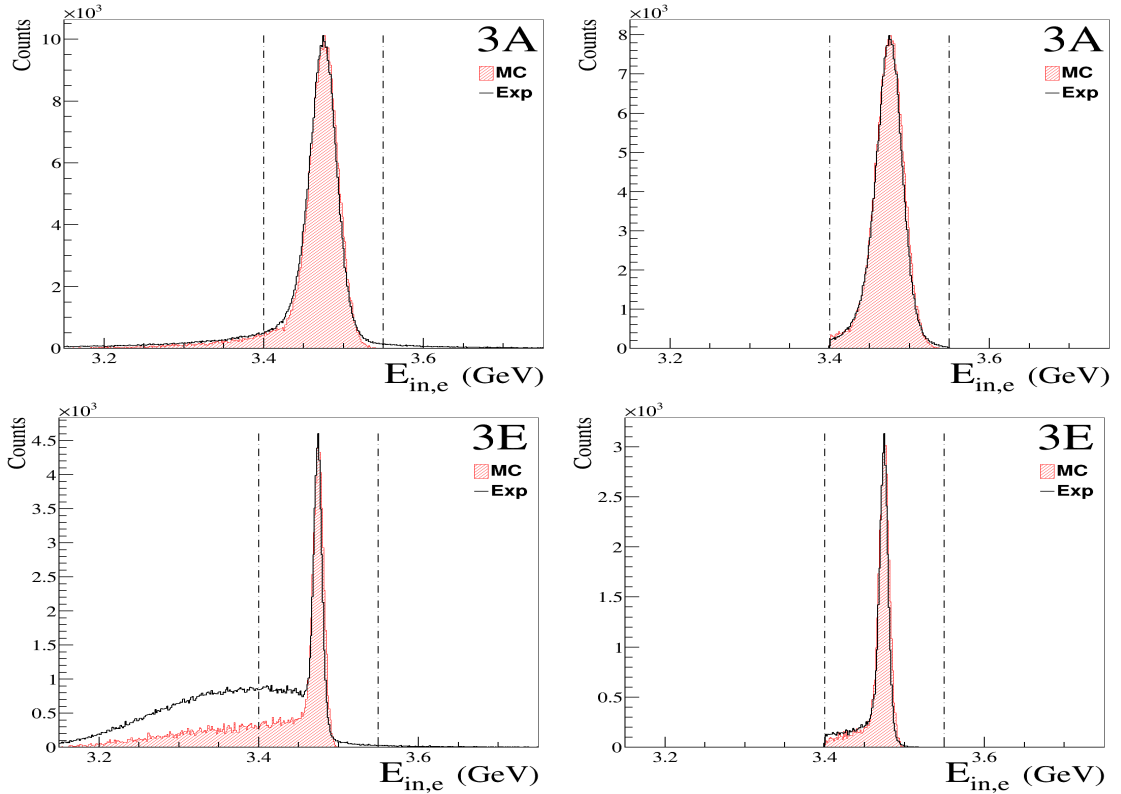


Figure 4.6: The beam energy for 3A and 3E reconstructed from HRS variables, including the beam energy cuts(vertical dashed lines). Raw data in the left column and final data in the right.

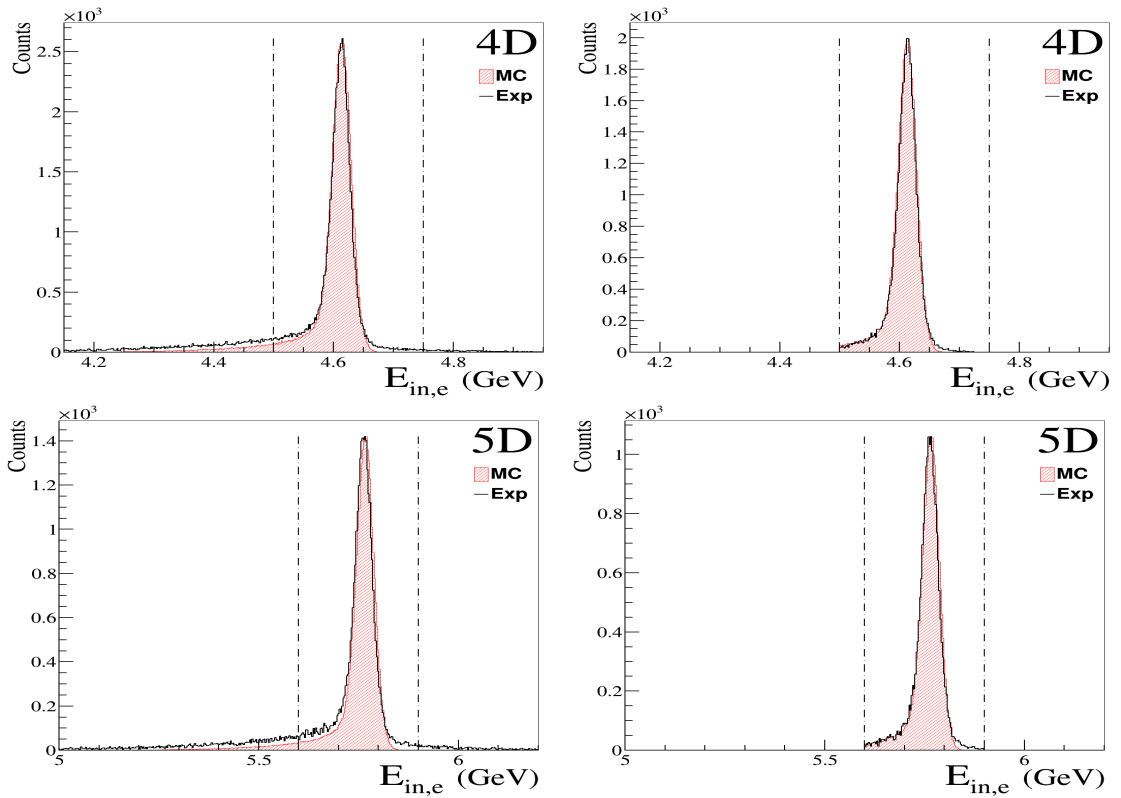


Figure 4.7: The beam energy for 4D and 5D reconstructed from HRS variables, including the beam energy cuts(vertical dashed lines). Raw data in the left column and final data in the right.

4.2.3 ep : Event Identification

Finally, the HRS variables can be used (Appendix B) to predict the hit position on the calorimeter surface. The difference between the predicted and the actual hit for x and y positions on the calorimeter, are shown in Figures 4.8, 4.9, 4.10 and 4.11. The energy difference is shown in Figures 4.12 and 4.13. These are three useful variables that clearly identify the elastic events. Loose cuts ($\sim 3\sigma$) on these variables are sufficient to extract reliable data (Y_{Data}) and MC (Y_{MC}) yields.

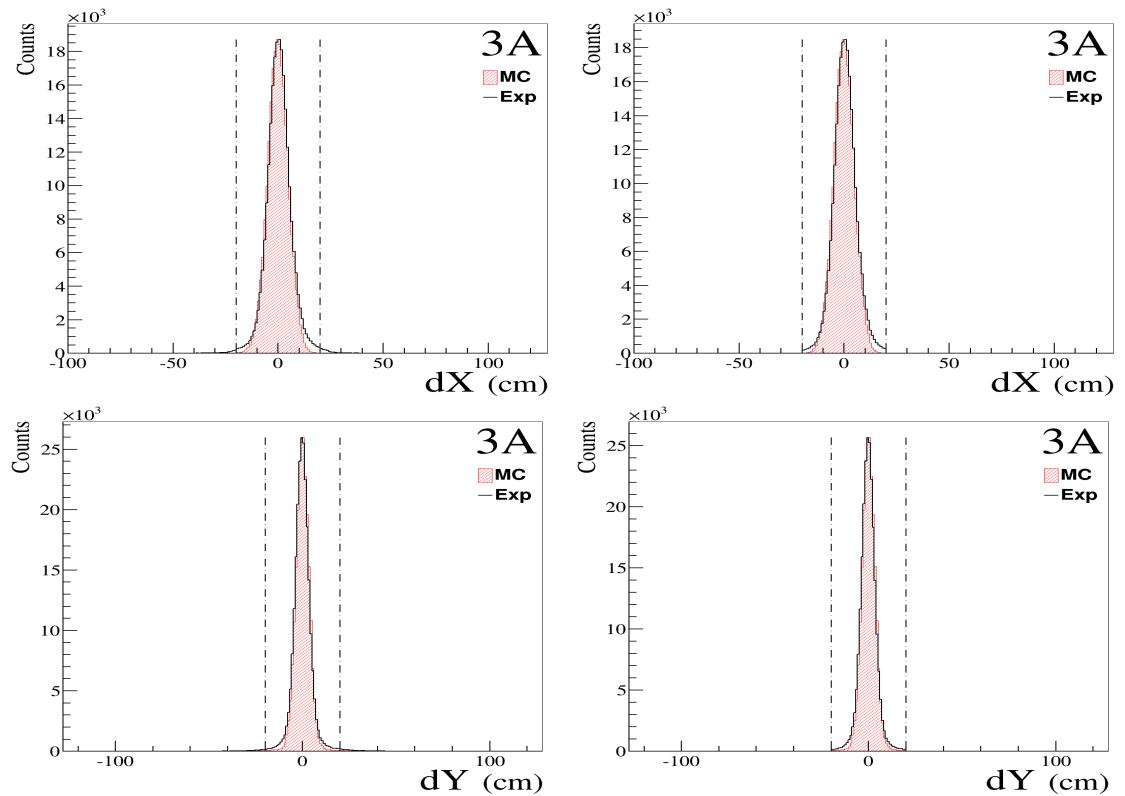


Figure 4.8: The difference between the HRS reconstructed hit position and the calorimeter hit position for 3A, including the applied cuts (vertical dashed lines). Reduced data in the left column and final data in the right.

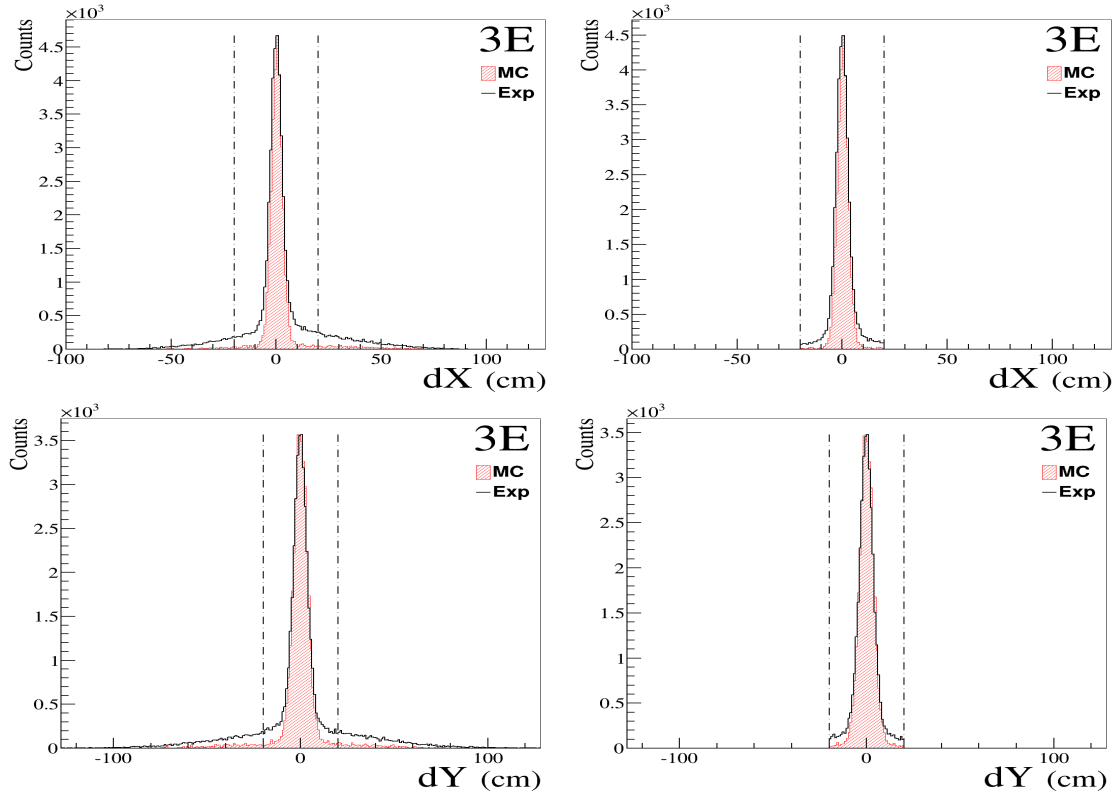


Figure 4.9: The difference between the HRS reconstructed hit position and the calorimeter hit position for 3E, including the applied cuts (vertical dashed lines). Reduced data in the left column and final data in the right.

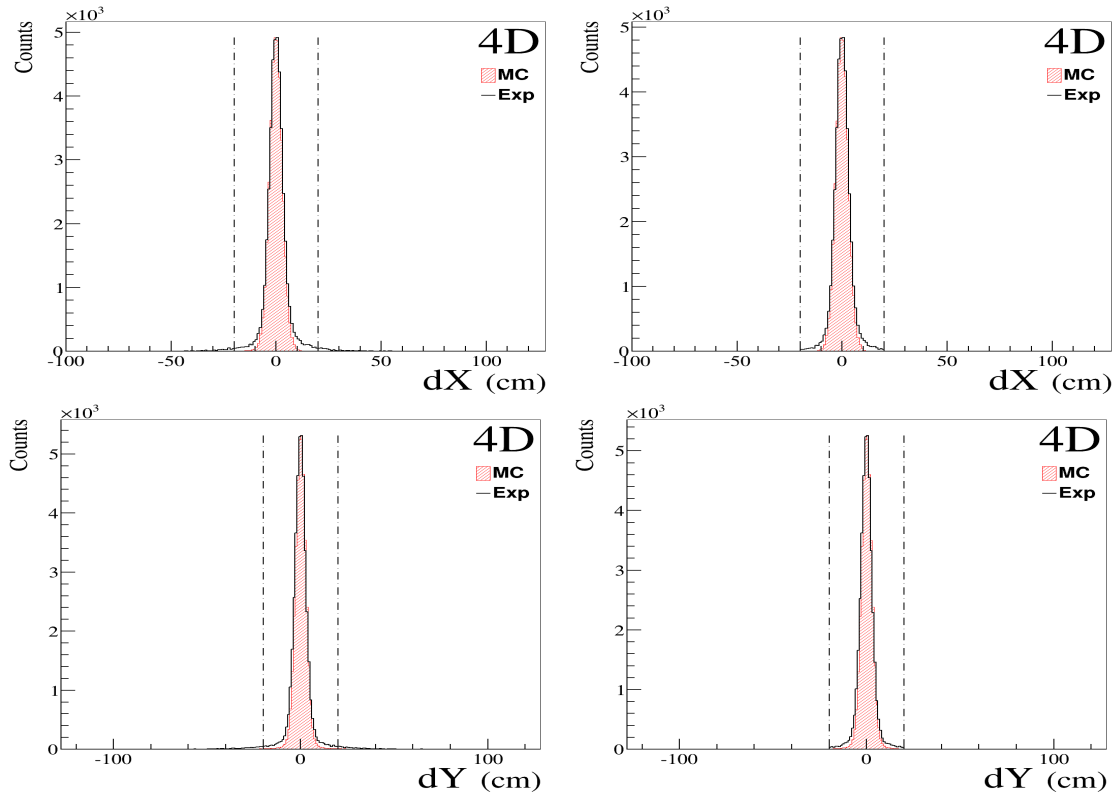


Figure 4.10: The difference between the HRS reconstructed hit position and the calorimeter hit position for 4D, including the applied cuts (vertical dashed lines). Reduced data in the left column and final data in the right.

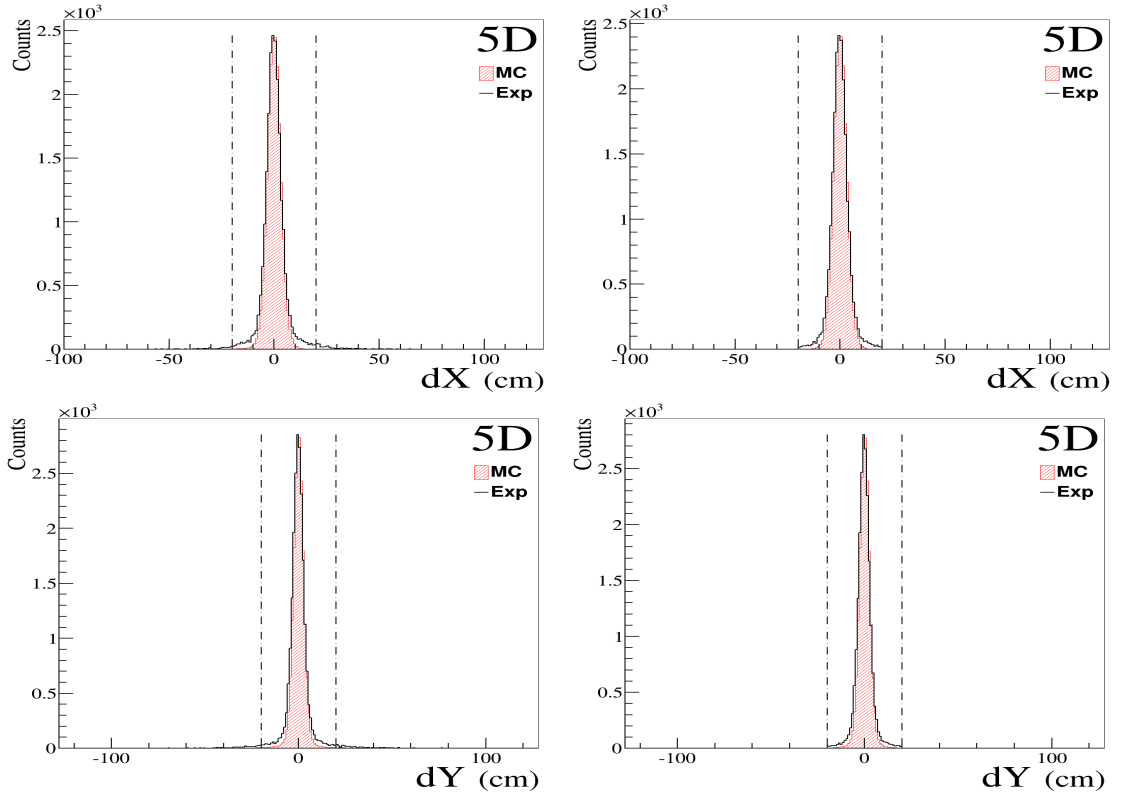


Figure 4.11: The difference between the HRS reconstructed hit position and the calorimeter hit position for 5D, including the applied cuts (vertical lines). Reduced data in the left column and final data in the right.

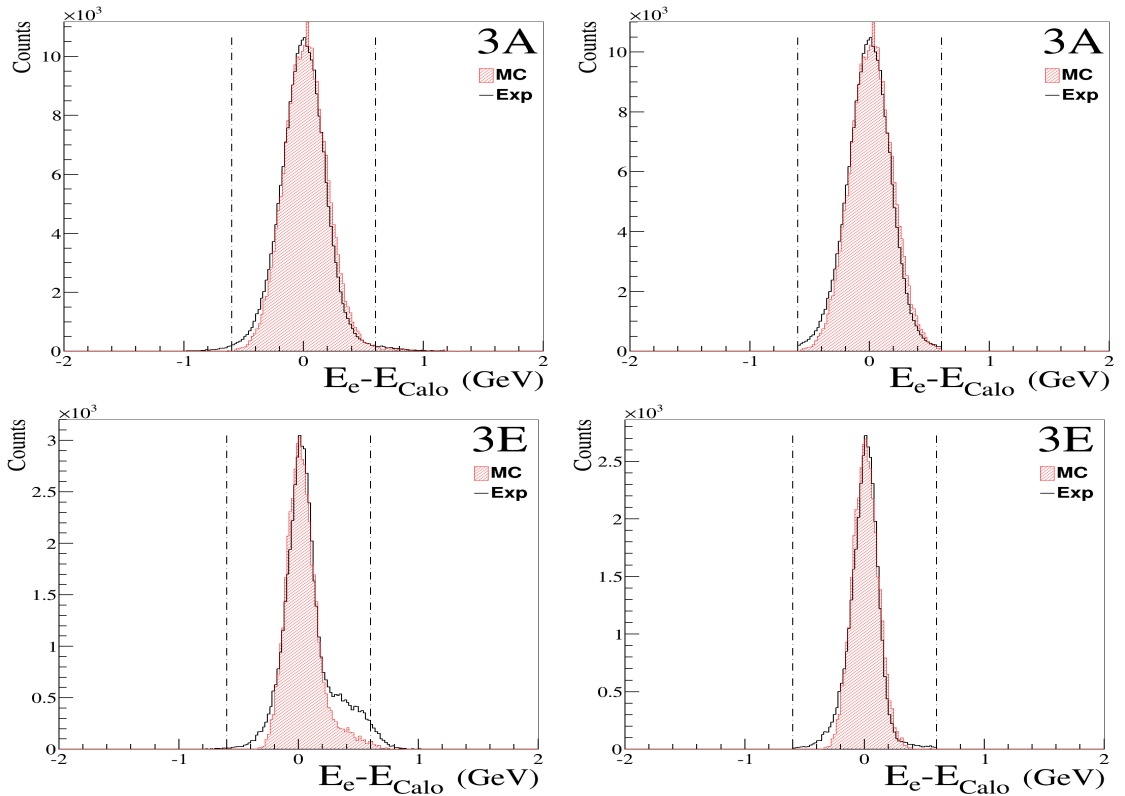


Figure 4.12: The difference between the reconstructed scattering energy, E_e , and the calorimeter energy, E_{Calo} , for 3A and 3E. The applied cuts are included as vertical dashed lines. Reduced data in the left column and final data in the right.

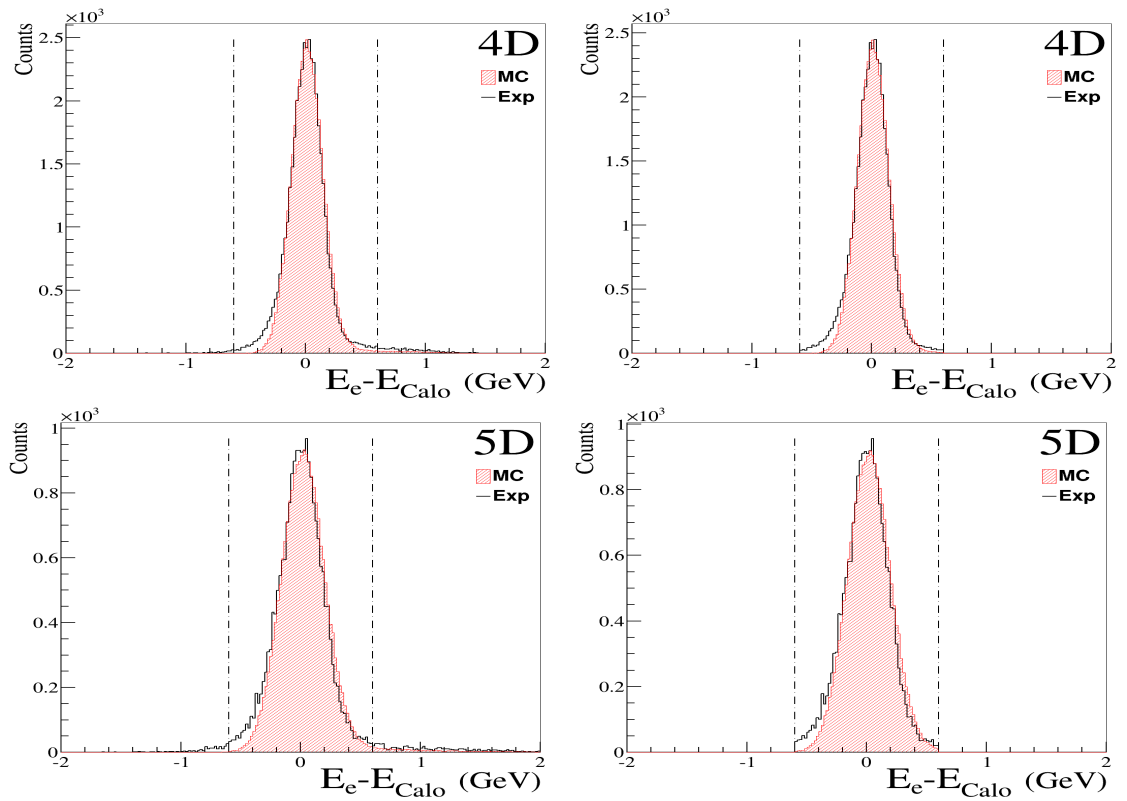


Figure 4.13: The difference between the reconstructed scattering energy, E_e , and the calorimeter energy, E_{Calo} , for 4D and 5D. The applied cuts are included as vertical dashed lines. Reduced data in the left column and final data in the right.

4.2.4 *ep*: Corrections

This section deals with inefficiencies of the detectors and electronics that are not simulated in the MC. These inefficiencies lead to loss of relevant data and can amount to as much as a 10% loss for some kinematic points. The corrections are summarized in Table 4.1 and the process of evaluating each correction is described in the following sections with the exception of the background subtraction which was described previously in Section 4.2.1.

| Kin | Comp. Live % | Track. Eff. % | Trigg. Eff % | Back. Sub. % |
|-----|--------------|---------------|--------------|--------------|
| 2A | 96.4 | 97.7 | 99.2 | 99.6 |
| 2B | 94.9 | 97.5 | 99.0 | 99.7 |
| 2C | 93.7 | 97.3 | 99.2 | 99.2 |
| 3A | 94.7 | 97.5 | 99.6 | 100 |
| 3B | 97.1 | 97.5 | 98.7 | 99.9 |
| 3C | 96.5 | 97.3 | 98.2 | 99.7 |
| 3D | 97.6 | 96.9 | 98.8 | 100 |
| 3E | 94.3 | 96.7 | 98.7 | 99.6 |
| 3F | 95.8 | 95.1 | 98.3 | 99.1 |
| 4A | 92.6 | 97.3 | 98.6 | 100 |
| 4B | 97.4 | 97.3 | 98.9 | 100 |
| 4C | 99.0 | 97.4 | 99.2 | 100 |
| 4D | 93.8 | 97.6 | 98.9 | 99.1 |
| 4E | 99.2 | 97.6 | 98.5 | 100 |
| 4F | 98.8 | 97.1 | 98.5 | 99.7 |
| 4G | 98.9 | 95.5 | 98.7 | 99.3 |
| 4H | 98.2 | 95.0 | 98.2 | 98.2 |
| 5A | 98.0 | 97.0 | 99.4 | 100 |
| 5B | 97.2 | 97.3 | 98.7 | 99.9 |
| 5C | 98.0 | 97.4 | 99.3 | 100 |
| 5D | 98.7 | 97.2 | 98.4 | 99.8 |
| 5E | 97.3 | 97.1 | 98.4 | 99.6 |
| 5F | 98.8 | 97.0 | 98.4 | 99.7 |
| 5G | 99.7 | 98.0 | 98.7 | 99.8 |
| 5H | 98.4 | 96.2 | 97.9 | 99.9 |

Table 4.1: Electron scattering correction factors ϵ_{lt} , ϵ_{track} , ϵ_{trigg} and ϵ_{bs} .

Computer, Detector and Electronic Deadtime

The computer livetime, and thus the deadtime, is very simple to obtain. It is the number of coincidence events (trigger T5) read into the data files divided by the

number of times that trigger has occurred (counted by a fast scaler). See Table 4.1 for the values obtained.

The electronic and detector deadtime correction was not measured directly in this experiment. Later Hall A experiments have included pulsers mounted directly on the detectors in various ways to measure this. Instead, it is simply noted that the trigger rate for the HRS arm (T7) was less than 30 kHz throughout the entire experiment. The electronic deadtime for the trigger planes is typically 100 ns while the response and decay times of a plastic scintillator is a few ns. This equates to a correction with an upper limit of 0.3%. The calorimeter had a much higher total trigger rate, up to 800 kHz, but this is distributed among the 32 *SUM8* groups building the 56 *SUM32* clusters forming the trigger, see Section 2.5.1. Thus the rate for each subsection was roughly a factor 20 smaller throughout the experiment and the pulse width from the calorimeter was 10 ns. In conclusion, this correction is below 1%.

Tracking and Triggering Efficiency

The tracking efficiency is estimated by taking the data that produced a coincidence trigger, a large energy signal in the calorimeter and a proton track that reconstructs to reasonable Hall variables and dividing out by the number of events for the same criteria but with no demand on a good reconstructed track.

Triggering efficiency is estimated by using the S1 and S2 scintillator planes and connected trigger T3 (S1 and S2). The S1 overlaps, geometrically, with the S0 more or less perfectly, but the S2 does not, so it is necessary to limit the study to central regions of the S1 and S2 scintillator planes. The efficiency is given by the ratio of events that triggered all three planes to the number of events that triggered only S1 and S2.

4.2.5 Electron Scattering Results

The results of the analysis of the *ep* scattering cross section show a very good agreement with the expected values. The data here are presented as ratios of the

extracted and expected cross sections. The reason is that the ratio can be compared across all the data points. For this part it was desirable to create some form of gauge of the systematical errors originating from an incomplete knowledge of the setup itself and its reproduction in the MC. Thus a set of four detector limiting cuts (including the original one) are defined as:

1. **Cut 1** (Original)
2. **Cut 2** [Calo] ($|X_{Calo}| < 20$ cm and $|Y_{Calo}| < 20$ cm)
3. **Cut 3** [HRS] ($|\phi_{tg}| < 0.02$ mr, $|\theta_{tg}| < 0.02$ mr and $|\delta| < 0.02$)
4. **Cut 4** [Calo and HRS]

and the analysis is repeated for each of these. The results including the statistical uncertainty are presented in Table 4.2 and are also included in Fig. 4.14 where the mean and total spread is obtained from a Maximum-Likelihood fit. The fact that the mean ratio is close to one and does not change significantly when the range is narrowed down shows that the MC can be relied upon for the cross section normalisation. The total spread is used as an estimate of the systematic errors outlined in Section 5.1.1.

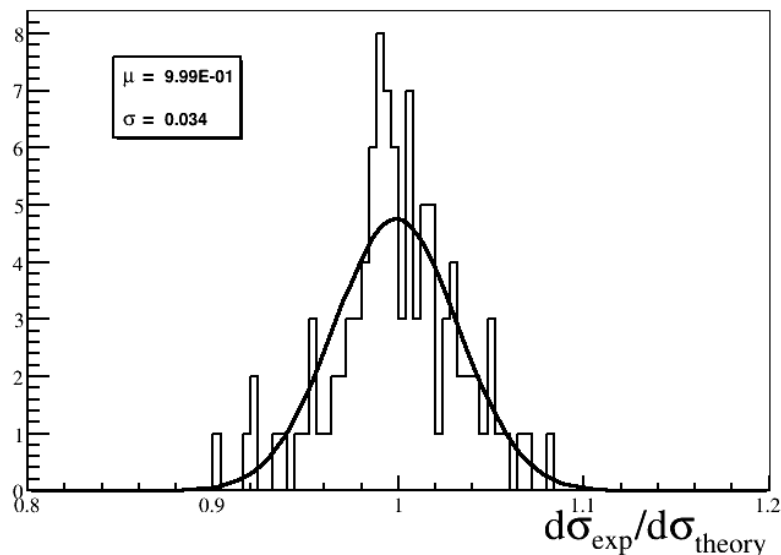


Figure 4.14: The ratio between the cross section($d\sigma_{theory}$) calculated from empirical fits to the form factors and the cross section($d\sigma_{exp}$) obtained from this experiment.

| Kin | Cut 1 | | Cut 2 | | Cut 3 | | Cut 4 | |
|--------------|-------|---------------------|-------|---------------------|-------|---------------------|-------|---------------------|
| | Ratio | $\delta_{stat}(\%)$ | Ratio | $\delta_{stat}(\%)$ | Ratio | $\delta_{stat}(\%)$ | Ratio | $\delta_{stat}(\%)$ |
| 2A | 1.02 | 1.05 | 1.04 | 1.66 | 1.03 | 1.71 | 1.04 | 2.00 |
| 2B | 1.06 | 1.07 | 1.04 | 1.63 | 1.02 | 2.01 | 1.00 | 2.22 |
| 2C | 0.98 | 3.32 | 0.95 | 5.22 | 0.97 | 5.09 | 1.04 | 6.57 |
| 3A | 1.03 | 0.40 | 1.04 | 0.60 | 1.01 | 0.83 | 1.03 | 0.86 |
| 3B | 1.01 | 0.39 | 1.00 | 0.59 | 1.00 | 0.81 | 1.01 | 0.84 |
| 3C | 0.99 | 0.51 | 0.98 | 0.77 | 0.98 | 1.05 | 0.97 | 1.11 |
| 3D | 1.01 | 0.45 | 0.98 | 0.71 | 0.98 | 0.79 | 0.96 | 0.88 |
| 3E | 0.99 | 0.88 | 0.98 | 1.41 | 0.97 | 1.35 | 0.95 | 1.61 |
| 3F | 1.04 | 1.89 | 1.04 | 3.04 | 0.97 | 2.49 | 0.97 | 3.28 |
| 4A | 0.98 | 0.33 | 1.01 | 0.45 | 1.00 | 0.76 | 1.01 | 0.77 |
| 4B | 1.01 | 0.32 | 1.01 | 0.47 | 0.99 | 0.69 | 1.01 | 0.71 |
| 4C | 1.05 | 0.39 | 1.05 | 0.56 | 1.02 | 0.82 | 1.03 | 0.84 |
| 4D | 1.00 | 0.52 | 1.00 | 0.76 | 0.97 | 1.12 | 0.98 | 1.14 |
| 4E | 1.04 | 0.85 | 1.00 | 1.29 | 0.99 | 1.75 | 0.99 | 1.82 |
| 4F | 1.04 | 1.07 | 0.99 | 1.72 | 1.01 | 1.88 | 0.99 | 2.10 |
| 4G | 1.07 | 1.37 | 1.03 | 2.20 | 1.01 | 2.10 | 0.99 | 2.50 |
| 4H | 1.05 | 2.04 | 1.01 | 3.26 | 1.02 | 2.58 | 0.98 | 3.45 |
| 5A | 0.99 | 0.29 | 1.01 | 0.37 | 1.01 | 0.69 | 1.01 | 0.69 |
| 5B | 0.92 | 0.42 | 0.93 | 0.59 | 0.91 | 0.90 | 0.92 | 0.91 |
| 5C | 0.99 | 0.65 | 0.99 | 0.91 | 0.97 | 1.41 | 0.98 | 1.43 |
| 5D | 1.01 | 0.71 | 1.02 | 0.99 | 0.97 | 1.54 | 0.97 | 1.56 |
| 5E | 0.99 | 1.03 | 0.99 | 1.47 | 0.95 | 2.19 | 0.96 | 2.22 |
| 5F | 1.04 | 1.25 | 1.02 | 1.87 | 0.99 | 2.58 | 0.99 | 2.64 |
| 5G | 0.98 | 2.29 | 0.95 | 3.59 | 0.94 | 4.38 | 0.95 | 4.52 |
| 5H | 0.99 | 0.94 | 0.98 | 1.47 | 0.99 | 1.76 | 0.98 | 1.84 |
| <Ratio> | 1.01 | | 1.00 | | 0.99 | | 0.99 | |
| < δ > | 0.033 | | 0.031 | | 0.028 | | 0.03 | |

Table 4.2: Electron cross section ratios.

4.3 π^0 -Photoproduction

The extraction of the π^0 cross section follows largely the above described extraction of the ep cross section. The main differences lies, of course, with the isolation of π^0 events from the main competing reaction channels (ep and Compton).

4.3.1 π^0 : Timing and Background Subtraction

This is performed exactly as in Section 4.2.1 above. The data are shown in Fig. 4.15 and the subtraction fraction is included in Table 4.3 in Section 4.3.4 below.

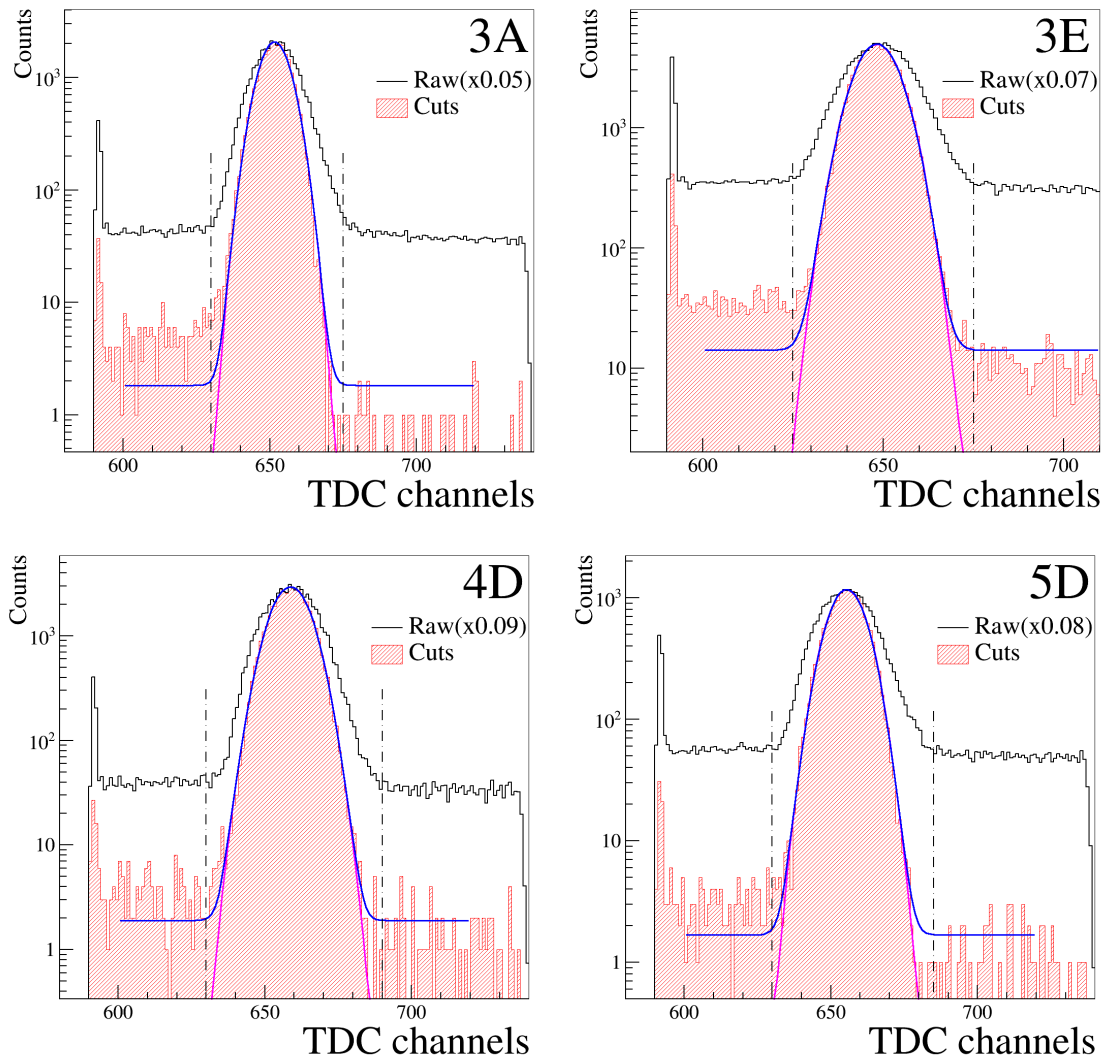


Figure 4.15: The figure shows scaled down raw timing distributions (black), the timing cuts applied (vertical dashed lines) and the timing distributions for final data (shaded red) without the timing cut. The blue curves indicate a fitted Gaussian plus a constant (random background) and the purple curves indicate the Gaussian part.

4.3.2 π^0 : Fiducial and Kinematical Data Reduction

As in the ep part the outer layers of the calorimeter must, for the reasons given in Sec 4.2.2, be excluded. The cuts are visualised in Fig. 4.16 and Fig. 4.17 and are again the same for all kinematic points.

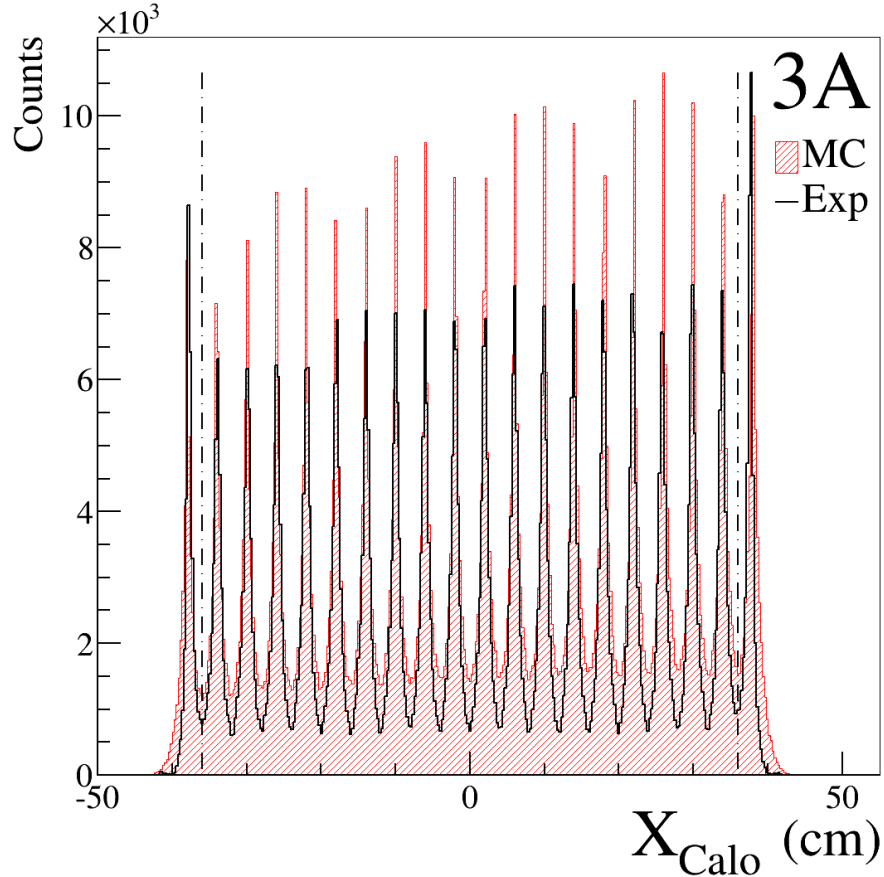


Figure 4.16: The calorimeter hit positions for 3A from raw data (black) and MC (red) with the applied cuts marked by the vertical dashed lines.

The HRS variables presented in Fig. 4.18 are limited in the same fashion as in Section 4.2.2 and for the same reasons. Again the left column of histograms in Fig. 4.18 contains the raw data and the right column contains the final data. In general there is good agreement between MC and experiment after the final cut has been applied.

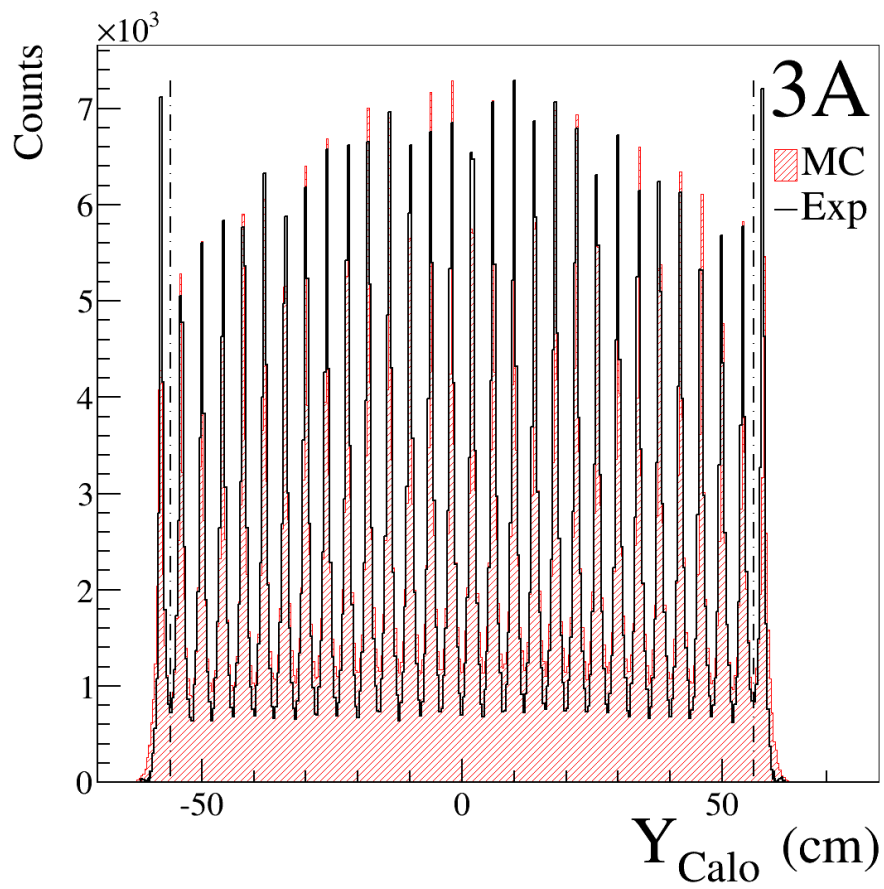


Figure 4.17: The calorimeter hit positions for 3A from raw data (black) and MC (red) with the applied cuts marked by the vertical dashed lines.

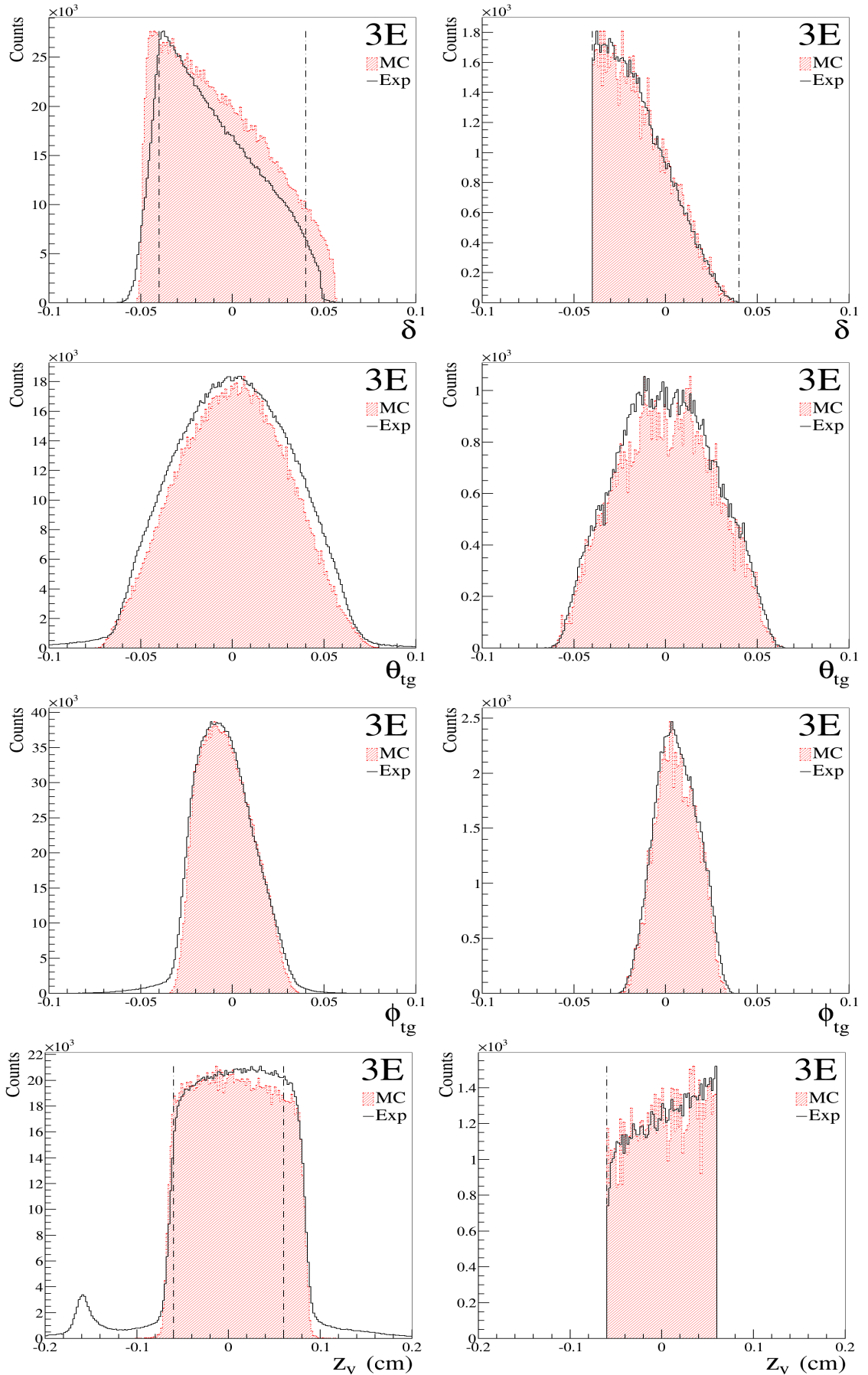


Figure 4.18: The HRS variables, θ_{tg} , ϕ_{tg} , δ and z_v in the HRS coordinate system including the applied cuts as vertical dashed lines. Raw data in the left column and final data in the right.

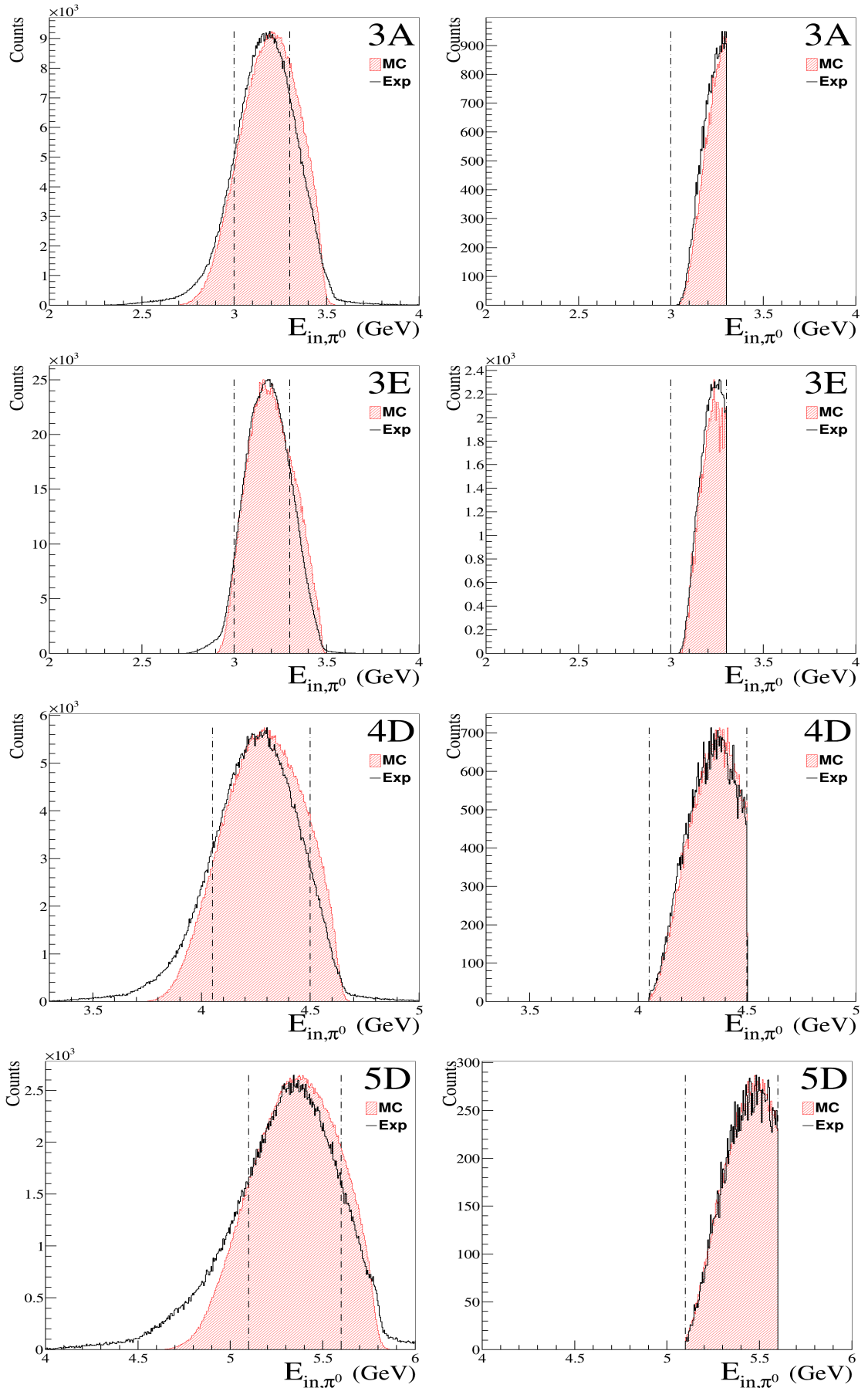


Figure 4.19: The beam energy reconstructed from HRS variables including the applied cuts (vertical dashed lines). Raw data in the left column and final data in the right.

4.3.3 π^0 : Event Identification

In contrast to the ep case the identification of π^0 s is slightly more complex. First of all, in order to remove Compton and ep events, indicated by the white ellipses in Fig. 4.20, from the π^0 events a rather large section of the positive dX side needs to be removed including the centre around the Compton events. It is also necessary to limit the acceptable dXdY values to within a circle. This is because the radius for the distribution of γ s from the π^0 decay in the laboratory frame is limited and the energy of the γ s from the extreme wide angle decays may approach the calorimeter threshold. Outside of this circle random coincidences start to dominate. For clarity the dXdY cut is shown in 2-dim for 3A in Fig. 4.20 and the MC to data comparisons are presented in Figures 4.21 and 4.22.

The difference between the calorimeter energy, E_{Calo} , and the derived photon energy, $E_{\gamma\pi^0}$, is depicted in Fig.4.23. The cut on the positive side is made to exclude low calorimeter energy events that are incompatible with a π^0 event.

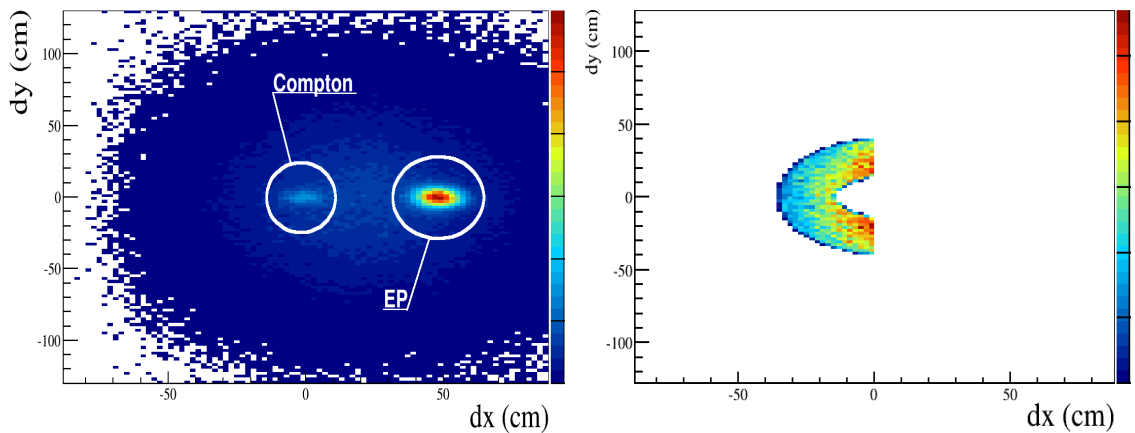


Figure 4.20: 2-dimensional hit position differences for 3A. Reduced data in the left picture and final data in the right. The white circles indicate the electron and Compton scattering peaks but do not correspond to any data cuts.

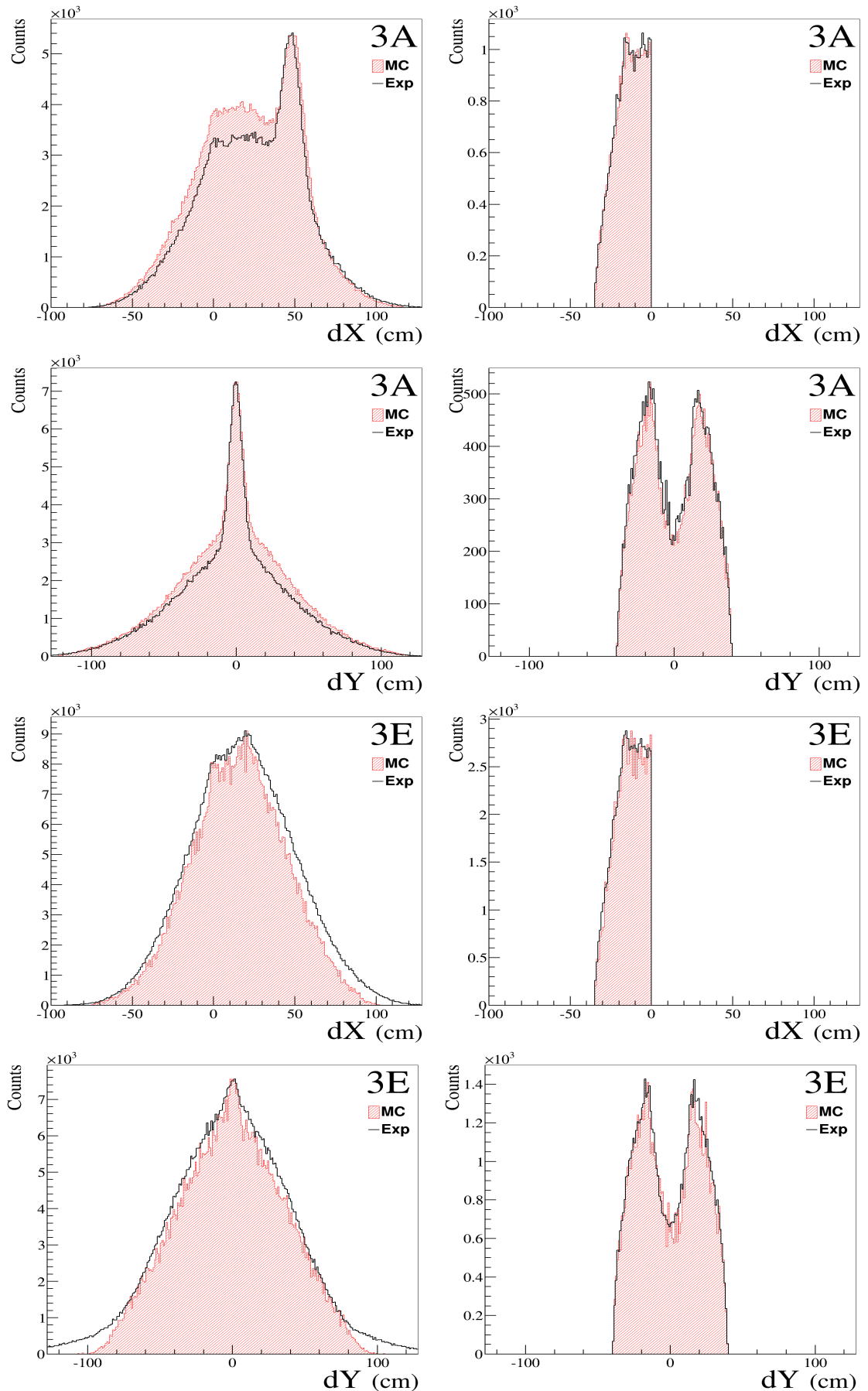


Figure 4.21: The difference between the HRS reconstructed hit position and the calorimeter hit position. Reduced data in the left column and final data in the right.

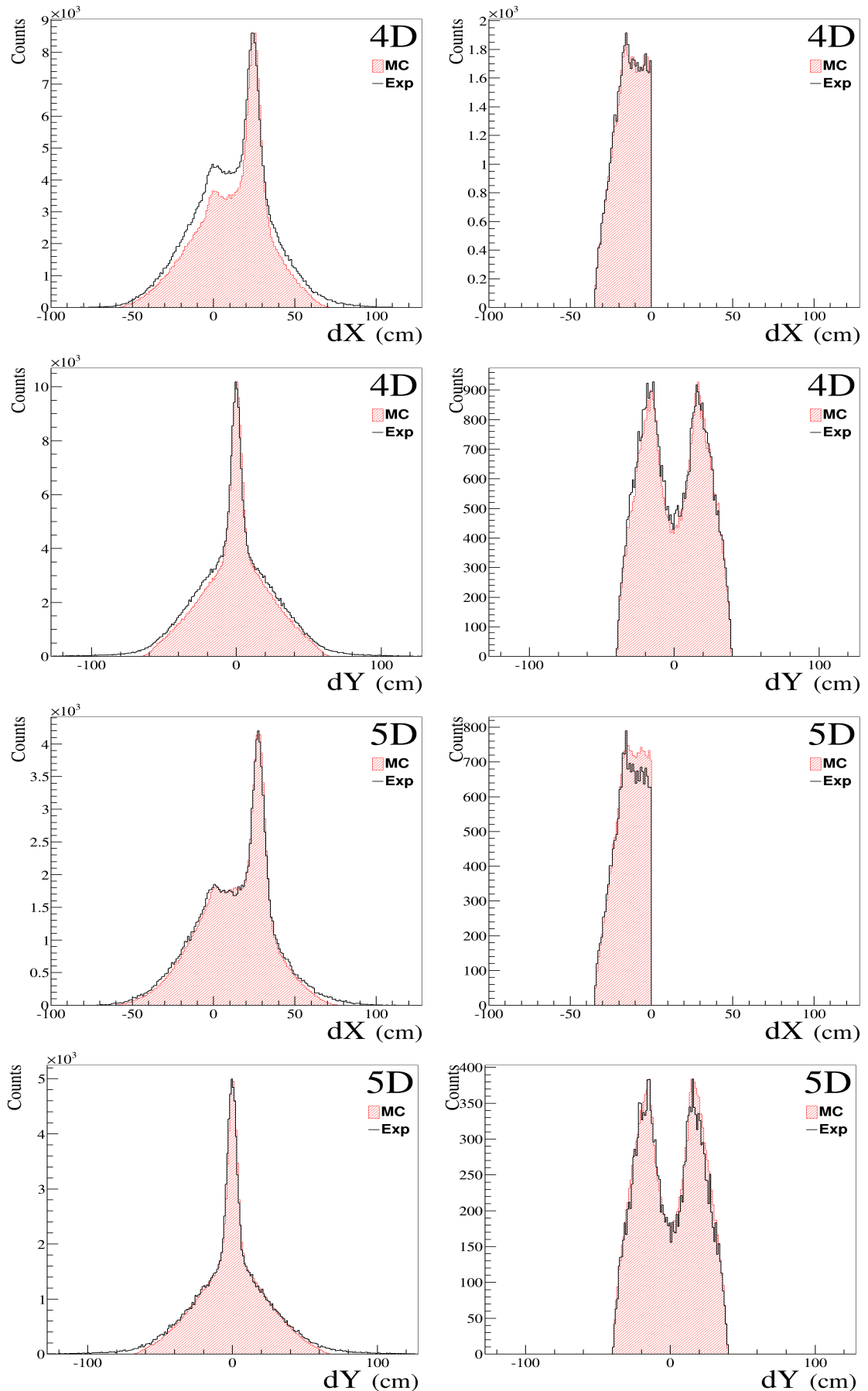


Figure 4.22: The difference between the HRS reconstructed hit position and the calorimeter hit position. Reduced data in the left column and final data in the right.

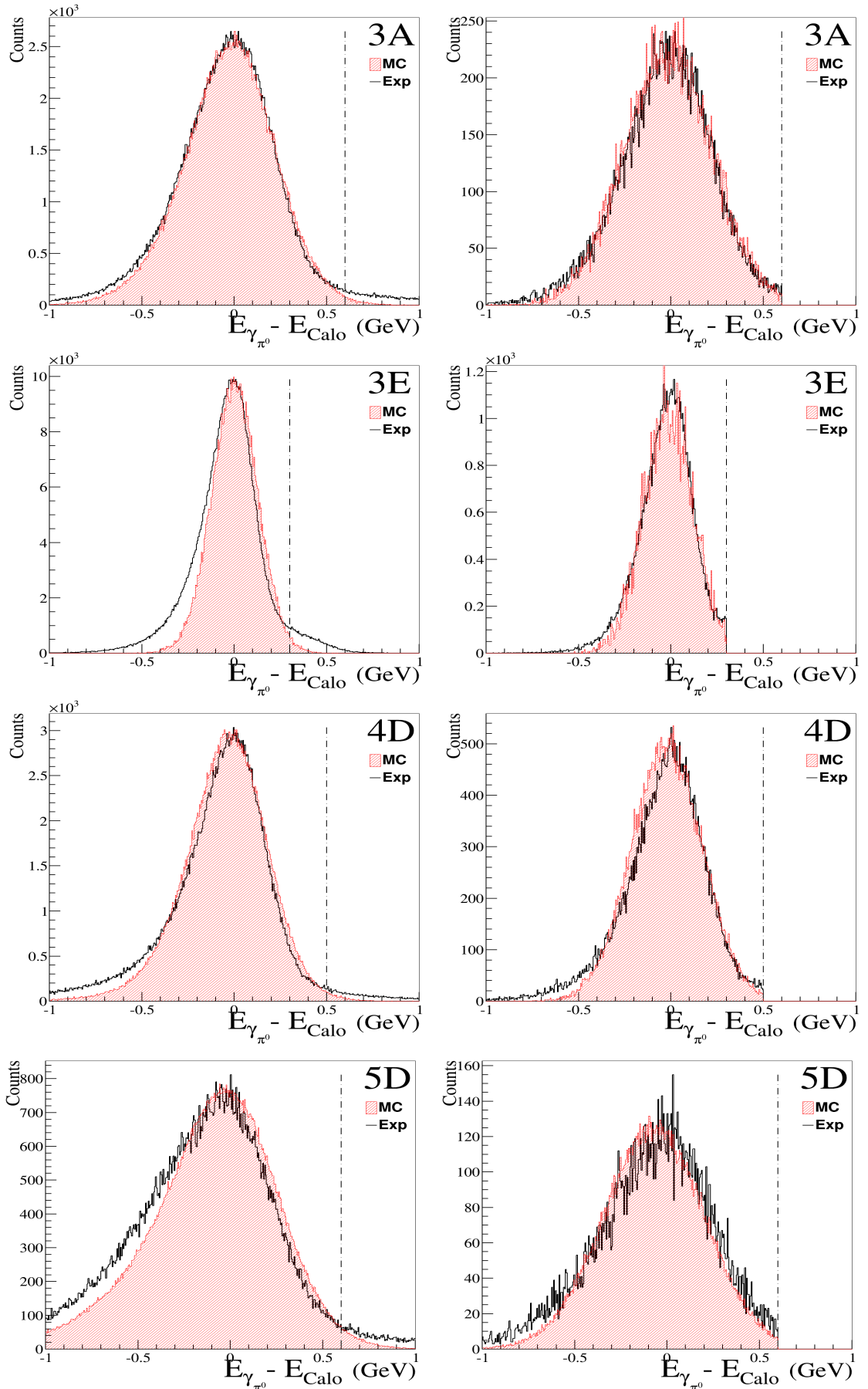


Figure 4.23: The difference between the derived photon energy, $E_{\gamma_{\pi^0}}$, and the calorimeter energy, E_{Calo} , including the applied cut as a dashed vertical line. Reduced data in the left column and final data in the right.

4.3.4 π^0 : Corrections

The correction factors for π^0 data, presented in Table 4.3, were obtained in the same fashion as for the ep data which were outlined in Section 4.2.4.

| Kin | Livetime % | Track. Eff. % | Trigg. Eff % | Back. Sub. % |
|-----|------------|---------------|--------------|--------------|
| 2A | 88.2 | 96.8 | 99.4 | 99.6 |
| 2B | 82.3 | 96.9 | 99.2 | 99.7 |
| 2C | 88.2 | 96.5 | 99.2 | 99.5 |
| 3A | 96.2 | 96.7 | 99.1 | 99.8 |
| 3B | 98.8 | 96.1 | 99.0 | 99.0 |
| 3C | 97.3 | 96.2 | 99.1 | 99.5 |
| 3D | 94.8 | 96.1 | 99.0 | 99.6 |
| 3E | 91.8 | 96.0 | 99.0 | 99.2 |
| 3F | 93.3 | 95.8 | 99.0 | 99.2 |
| 4A | 97.8 | 96.6 | 99.0 | 99.9 |
| 4B | 98.7 | 95.1 | 99.1 | 99.0 |
| 4C | 97.1 | 95.1 | 98.9 | 98.8 |
| 4D | 97.8 | 95.1 | 98.8 | 99.8 |
| 4E | 95.0 | 94.7 | 98.8 | 99.6 |
| 4F | 90.2 | 94.7 | 98.9 | 99.3 |
| 4G | 96.7 | 95.5 | 99.0 | 99.5 |
| 4H | 93.3 | 95.1 | 99.1 | 99.5 |
| 5A | 98.4 | 96.3 | 99.0 | 98.9 |
| 5B | 97.5 | 95.9 | 99.2 | 99.2 |
| 5C | 97.0 | 95.2 | 98.9 | 99.5 |
| 5D | 95.1 | 93.9 | 98.7 | 99.5 |
| 5E | 94.1 | 93.9 | 98.7 | 99.6 |
| 5F | 93.9 | 93.6 | 98.6 | 99.6 |
| 5G | 97.8 | 93.6 | 98.6 | 99.8 |
| 5H | 96.0 | 93.2 | 98.5 | 99.7 |

Table 4.3: π^0 correction factors ϵ_{lt} , ϵ_{track} , ϵ_{trigg} and ϵ_{bs} .

 π^0 -Electroproduction

There exists other possible reaction channels that could look very similar to Compton scattering and π^0 photoproduction. The most likely candidate is π^0 electroproduction. The electroproduction cross section, $\delta^3\sigma/\delta E_e\delta\Omega_e\delta\Omega_{\pi^0}$, using the same electron energy notations as before and $\delta\Omega_{e,\pi^0}$ as the scattered electron/ π^0 solid angle, may be written [111] as

$$\delta^3\sigma/\delta E_e\delta\Omega_e\delta\Omega_{\pi^0} = \Gamma[\delta\sigma_T/\delta\Omega_{\pi^0} + \epsilon\delta\sigma_L/\delta\Omega_{\pi^0} + \epsilon\delta\sigma_P/\delta\Omega_{\pi^0} \cos(2\phi_{\pi^0}) + \sqrt{2\epsilon(1+\epsilon)}\delta\sigma_I/\delta\Omega_{\pi^0} \cos(\phi_{\pi^0})] \quad (4.4)$$

where Γ is the virtual photon flux factor given by

$$\Gamma = (\alpha/2\pi^2Q^2)(E_\gamma/[1-\epsilon])(E_e/E_{in,e}). \quad (4.5)$$

Here E_γ is the photon energy and the polarization factor ϵ is calculated from

$$\epsilon = [1 + (2|q|^2/Q^2)\tan^2(\theta_e/2)]^{-1}. \quad (4.6)$$

with the momentum of the virtual photon given by q and the electron scattering angle by θ_e . The $\delta\sigma_{T,L,P,I}/\delta\Omega$ are the transverse, longitudinal, polarization and interference cross sections. Only the transverse term remains as $Q^2 \rightarrow 0$ and at this limit eq. 4.4 should provide a connection between electro- and photoproduction. For this correction it is assumed that the cross section for production from low virtuality photons is the same as for real photons. The connected uncertainty is discussed further in Section 5.1.1. The virtual photon flux can be calculated to first order in m_e^2 via

$$\begin{aligned} \Gamma = (\alpha/4\pi^2\omega)[(E_{in,e}2 + E_e^2)/(2E_{in,e}2(m_e^2\omega^2/4E_{in,e}2E_e^2 + \sin^2(\theta_e/2))) \\ - E_em^2\omega^2/(4E_{in,e}3E_e^2(m_e^2\omega^2/4E_{in,e}2E_e^2 + \sin^2(\theta_e/2)))^2 \\ - (E + E_e)^2/(4E_{in,e}2(m_e^2\omega^2/4E_{in,e}2E_e^2 + \sin^2(\theta_e/2)))] \end{aligned} \quad (4.7)$$

which is also from Ref. [111] and here $\omega = E_{in,e} - E_e$. This result can then be compared to the bremsstrahlung flux. The percentage of virtual photon flux varies between 3.7% and 4.1% so a general correction of 4% has been included in the final results.

Chapter 5

Results and Discussion

“All that we see or seem is but a dream within a dream.” - E. A. Poe

In this chapter the results of the π^0 analysis is presented along with the estimations of the systematic uncertainties. Following this the applicability of scaling relations to the data is tested and compared with perturbative QCD (pQCD) predictions and kinematic dependencies from GPD derived results are examined. These results are discussed and also compared with previous measurements.

5.1 π^0 Results

The results for the π^0 cross section extracted via the method described in the previous Chapter 4 can be found in Table 5.1 and in Fig.5.1. The raw yields, accumulated charge and Monte Carlo cross section can be found in Table D.1 in Appendix D. This section will present an estimation of the systematic uncertainties.

5.1.1 Systematic Uncertainties

One systematic uncertainty is the error in the incident beam flux. First, the flux of electrons striking the radiator, i.e. the flux of the original electron beam, is given by the calibrated BCM monitors. These devices are calibrated every 2-3 months and the results have been extensively studied by the Hall A technical personnel and found to vary by 0.5%, which has been taken as the systematic error on the electron

| Kin | $d\sigma_{dt}$ | δ_{dt} | t | $\cos \theta_{cm}$ | s | E_{in}^{low} | E_{in}^{high} |
|-----|----------------|---------------|--------|--------------------|--------|----------------|-----------------|
| 2A | 959 | 12 | -1.649 | -0.016 | 4.868 | 2.000 | 2.250 |
| 2B | 768 | 6 | -2.013 | -0.241 | 4.868 | 2.000 | 2.250 |
| 2C | 232 | 2 | -2.605 | -0.605 | 4.868 | 2.000 | 2.250 |
| 3A | 82.8 | 0.7 | -1.995 | 0.221 | 6.792 | 3.000 | 3.300 |
| 3B | 10.4 | 0.2 | -2.627 | -0.025 | 6.792 | 3.000 | 3.300 |
| 3C | 16.7 | 0.2 | -3.039 | -0.186 | 6.792 | 3.000 | 3.300 |
| 3D | 30.7 | 0.2 | -3.695 | -0.442 | 6.792 | 3.000 | 3.300 |
| 3E | 46.3 | 0.5 | -4.028 | -0.572 | 6.792 | 3.000 | 3.300 |
| 3F | 54.8 | 0.4 | -4.348 | -0.697 | 6.792 | 3.000 | 3.300 |
| 4A | 28.40 | 0.16 | -2.030 | 0.437 | 8.903 | 4.050 | 4.500 |
| 4B | 2.11 | 0.03 | -2.571 | 0.287 | 8.903 | 4.050 | 4.500 |
| 4C | 2.00 | 0.04 | -3.087 | 0.144 | 8.903 | 4.050 | 4.500 |
| 4D | 3.58 | 0.02 | -3.676 | -0.020 | 8.903 | 4.050 | 4.500 |
| 4E | 3.10 | 0.02 | -4.383 | -0.216 | 8.903 | 4.050 | 4.500 |
| 4F | 3.45 | 0.02 | -5.031 | -0.396 | 8.903 | 4.050 | 4.500 |
| 4G | 4.99 | 0.04 | -5.478 | -0.520 | 8.903 | 4.050 | 4.500 |
| 4H | 10.71 | 0.05 | -5.925 | -0.644 | 8.903 | 4.050 | 4.500 |
| 5A | 1.153 | 0.020 | -2.612 | 0.433 | 10.920 | 5.100 | 5.600 |
| 5B | 0.832 | 0.012 | -3.184 | 0.309 | 10.920 | 5.100 | 5.600 |
| 5C | 1.107 | 0.012 | -3.731 | 0.190 | 10.920 | 5.100 | 5.600 |
| 5D | 0.815 | 0.006 | -4.414 | 0.042 | 10.920 | 5.100 | 5.600 |
| 5E | 0.764 | 0.006 | -5.028 | -0.092 | 10.920 | 5.100 | 5.600 |
| 5F | 0.834 | 0.005 | -5.442 | -0.182 | 10.920 | 5.100 | 5.600 |
| 5G | 1.101 | 0.006 | -5.934 | -0.289 | 10.920 | 5.100 | 5.600 |
| 5H | 1.105 | 0.005 | -6.461 | -0.403 | 10.920 | 5.100 | 5.600 |

Table 5.1: π^0 photoproduction cross section results. Units are nb/GeV², GeV² and GeV for the cross section, Mandelstam variables and beam energies respectively.

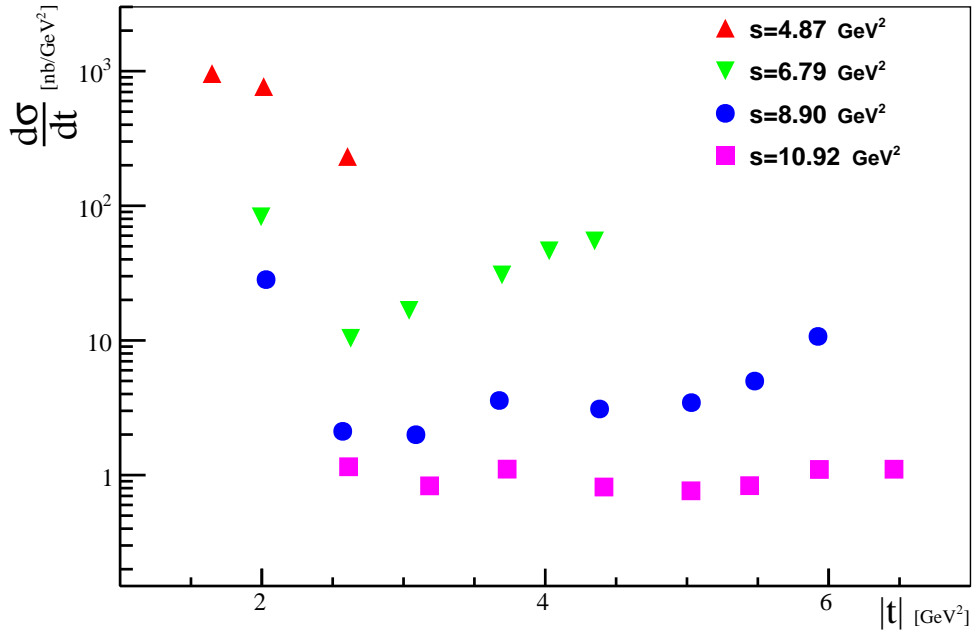


Figure 5.1: $\frac{d\sigma}{dt}$ vs. $|t|$. Note that the error bars are smaller than the size of the data symbols.

beam current (δ_{Curr}). Second, the calculation of the photon flux is expected to have an error $\delta_{Flux} = 3\%$ [96].

Another error originates from the limitation on the understanding of the experimental setup, in real life and thus also in the simulation. The results from ep scattering (see Table. 4.2 and Fig. 4.14), specifically the spread, are used here. The spread is attributed to uncertainties in the detector responses due to positioning uncertainties, resolutions used in the simulation, tracking efficiency, triggering efficiency, live time and random subtraction. The statistical uncertainty and the electron flux uncertainties will also contribute to this spread, but these contributions have not been deconvoluted. Thus the systematic error in the understanding of the setup is an upper limit. This uncertainty (δ_{Equip}) is thus estimated to be equal to the spread from the fit to the electron results i.e. 3.4%.

As mentioned in the beginning of Chapter 4, it is important to study the effects on the MC simulation of a different input π^0 cross section. The main results are compared with the results obtained with a cross section differing by a factor of two, a uniform cross section and a cross section without scaling. The inclusion of η photoproduction is also investigated. As can be seen from Table 5.2 the cross section

is fairly stable. The largest deviation, roughly 3.5%, occurs when using a uniform cross section and for the rest the deviation is around 1-2%. The error here ($\delta_{d\sigma}$) is taken to be 3.5%.

The correction for electroproduction is based on the assumption that the electroproduction cross section for low Q^2 tends towards, and in the $Q^2 \rightarrow 0$ limit is equal to, the photoproduction cross section. This behaviour is expected, but not verified, for this kinematic region. Because the cross section is not known experimentally, the uncertainty associated with this correction ($\delta_{e\pi^0 p}$) covers the possibility that it doesn't contribute at all or that the contribution is a factor of two larger. Larger contributions would have been seen in the ep scattering data. Thus the attributed 4% uncertainty is a conservative estimate.

In total, the systematic uncertainty of the π^0 photoproduction cross section is:

$$\begin{aligned} \delta &= \sqrt{\delta_{Curr}^2 + \delta_{Flux}^2 + \delta_{Equip}^2 + \delta_{d\sigma}^2 + \delta_{e\pi^0 p}^2} \\ &= \sqrt{0.5^2 + 3^2 + 3.4^2 + 3.5^2 + 4^2} = 7.0\%. \end{aligned} \quad (5.1)$$

5.2 Kinematic Dependencies of the Cross Section

5.2.1 pQCD

The s-scaling dependence for the cross section for π^0 -photoproduction is expected, according to eq. 1.22, from pQCD and constituent counting rules, to be s^{-7} . The experimental values were extracted at five different centre-of-mass scattering angles, evenly distributed between 80 and 120 degrees. For each angle a first or second order polynomial fit was made to the adjacent data points in θ_{cm} . For most cases three points were used but for some only two could be considered. The procedure is seen in Figs. 5.2, 5.3 and 5.4. The results for the scaling parameter are plotted in Fig. 5.5.

| Kin | $d\sigma_{Main}$ | $d\sigma_{2.d\sigma}$ | $d\sigma_{0.5.d\sigma}$ | $d\sigma_{NoScal}$ | $d\sigma_{Uni}$ | $d\sigma_{\eta}$ |
|-----|------------------|-----------------------|-------------------------|--------------------|-----------------|------------------|
| 2A | 995 | 1011 | 952 | 980 | 985 | 1020 |
| 2B | 796 | 781 | 777 | 781 | 781 | 803 |
| 2C | 241 | 237 | 240 | 234 | 234 | 238 |
| 3A | 86.0 | 84.1 | 85.1 | 86.4 | 83.1 | 85.8 |
| 3B | 10.8 | 10.6 | 10.4 | 10.7 | 10.6 | 10.8 |
| 3C | 17.4 | 17.1 | 17.2 | 17.0 | 17.0 | 17.3 |
| 3D | 31.8 | 32.0 | 31.2 | 31.2 | 31.0 | 31.4 |
| 3E | 48.1 | 47.1 | 49.6 | 47.1 | 46.9 | 49.0 |
| 3F | 56.9 | 57.2 | 57.5 | 56.1 | 55.8 | 56.1 |
| 4A | 29.43 | 29.26 | 28.62 | 29.11 | 28.42 | 29.24 |
| 4B | 2.20 | 2.21 | 2.11 | 2.18 | 2.14 | 2.20 |
| 4C | 2.08 | 2.06 | 2.03 | 2.05 | 2.02 | 2.06 |
| 4D | 3.72 | 3.78 | 3.69 | 3.64 | 3.63 | 3.69 |
| 4E | 3.22 | 3.25 | 3.22 | 3.12 | 3.12 | 3.19 |
| 4F | 3.59 | 3.57 | 3.62 | 3.49 | 3.44 | 3.52 |
| 4G | 5.19 | 5.13 | 5.21 | 5.04 | 4.97 | 5.10 |
| 4H | 11.14 | 10.72 | 11.27 | 10.83 | 10.65 | 10.91 |
| 5A | 1.200 | 1.259 | 1.095 | 1.197 | 1.061 | 1.204 |
| 5B | 0.866 | 0.893 | 0.830 | 0.853 | 0.806 | 0.858 |
| 5C | 1.153 | 1.172 | 1.112 | 1.130 | 1.092 | 1.136 |
| 5D | 0.849 | 0.854 | 0.821 | 0.835 | 0.822 | 0.837 |
| 5E | 0.796 | 0.791 | 0.803 | 0.779 | 0.778 | 0.782 |
| 5F | 0.869 | 0.867 | 0.870 | 0.849 | 0.844 | 0.847 |
| 5G | 1.146 | 1.158 | 1.144 | 1.115 | 1.112 | 1.123 |
| 5H | 1.151 | 1.147 | 1.118 | 1.119 | 1.110 | 1.124 |

Table 5.2: Systematic variation of the final π^0 cross section on the assumed initial cross section input to the MC. The $d\sigma_{Main}$ column contains the main results of this analysis. The following four columns are the results obtained with various modifications of the MC input cross section. $d\sigma_{2.d\sigma}$ corresponds to a doubling of the MC input cross section, $d\sigma_{0.5.d\sigma}$ to a halving, $d\sigma_{NoScal}$ to a cross section without incident energy scaling and $d\sigma_{Uni}$ is obtained with a uniform cross section. Finally, the last column holds the results when η photoproduction have been included in the MC. Note: the electroproduction correction has not been applied.

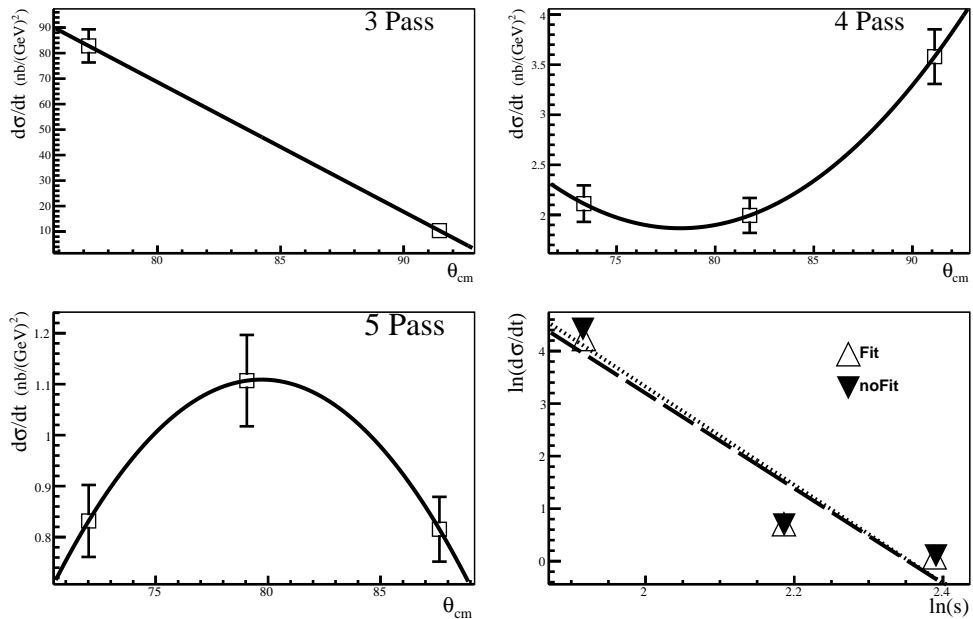
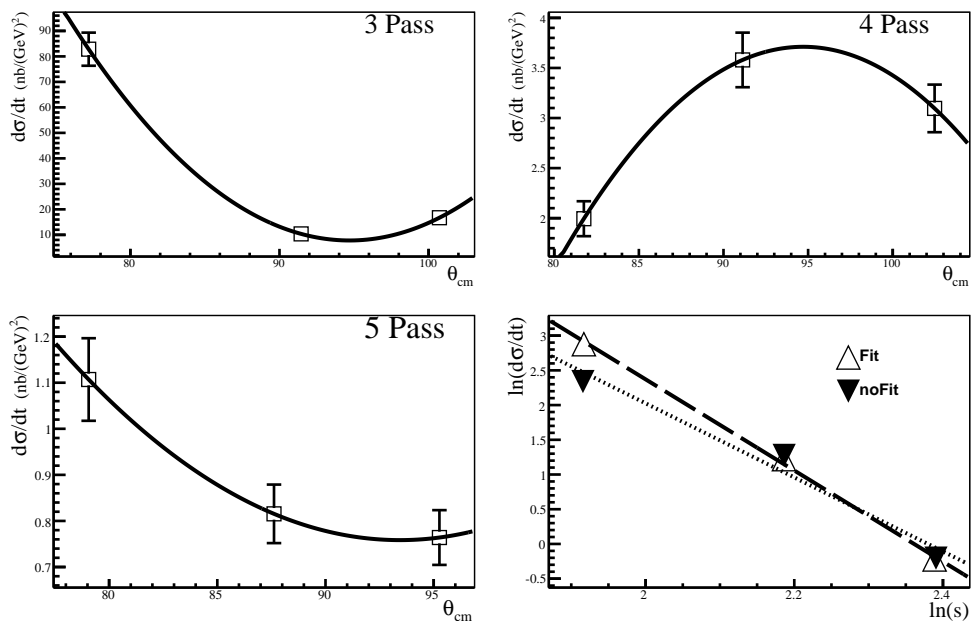
(a) $\theta_{cm} = 80^\circ$ (b) $\theta_{cm} = 90^\circ$

Figure 5.2: The fitting steps used in extracting the scaling power at $\theta_{cm} = 80^\circ$ and 90° . For each angle a first or second order polynomial is fitted to the three (sometimes two) data points closest to the angle for all beam energies where this angle was available. These fits are shown in the top and bottom-left plots. The result of this is plotted as empty triangles on a log-log scale in the bottom-right plot along with a linear fit shown as a dashed line from which the scaling power is extracted. As a comparison the value for the kinematic point closest to the angle for each beam energy is also plotted along with a linear fit to these data points as a dotted line.

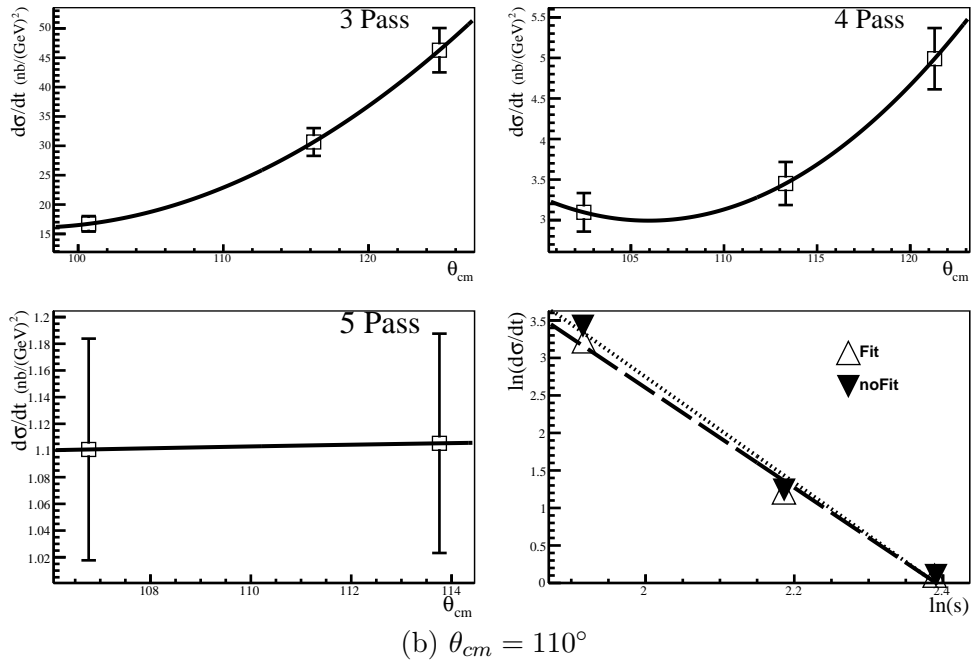
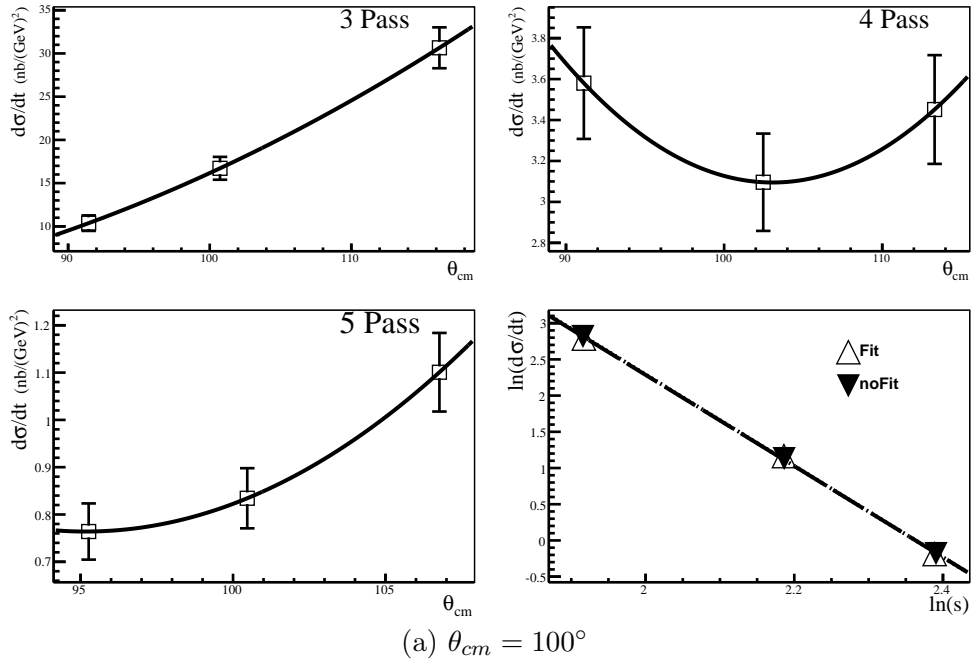


Figure 5.3: The fitting steps used in extracting the scaling power at $\theta_{cm} = 100^\circ$ and 110° . The steps are explained in Fig. 5.2.

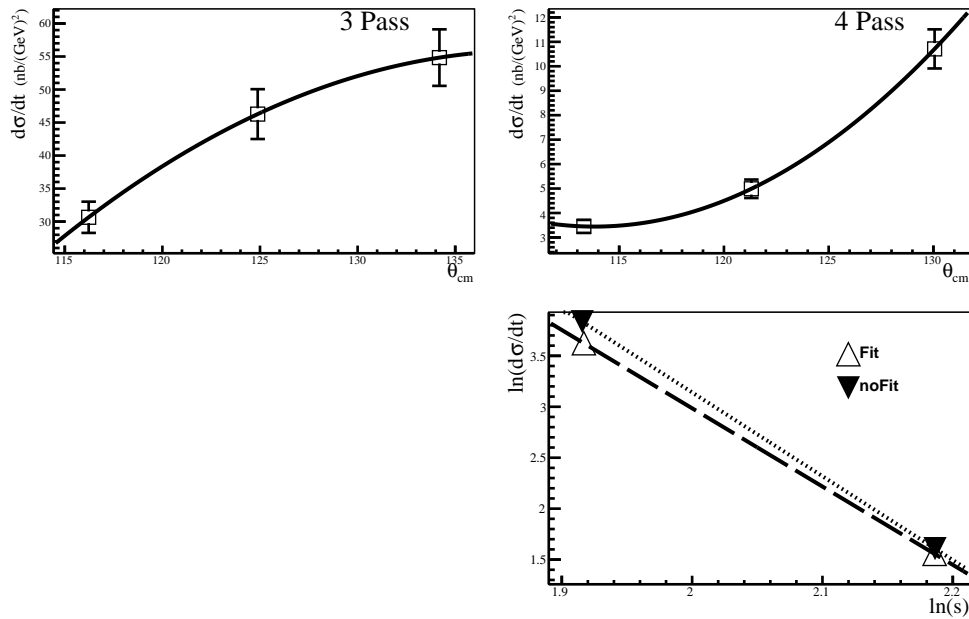


Figure 5.4: The fitting steps used in extracting the scaling power at $\theta_{cm} = 120^\circ$. The steps are explained in Fig. 5.2.

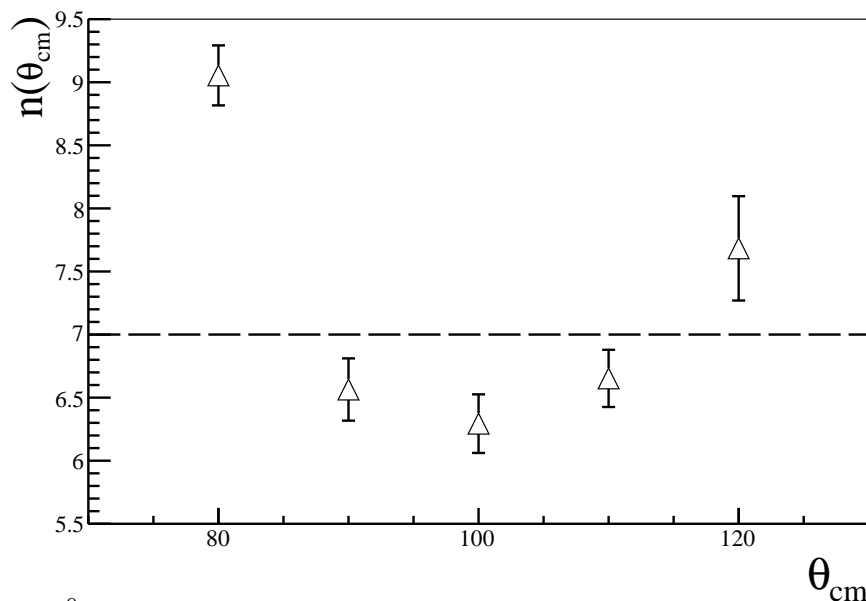


Figure 5.5: π^0 scaling factor n in eq.1.22 is shown as a function of θ_{cm} for values between 80 and 120 degrees. The straight dashed line is the pQCD(1.3.2) prediction for π^0 photoproduction.

In contrast to the results obtained for the Compton channel[54] the scaling parameter only appears relatively insensitive to the angle, with a value roughly 6.5, in the angular range 90 to 110 deg. The other two angles especially at 80 degrees, differ substantially.

It is of course very important to compare the results of this experiment with previous ones. The measurements of Anderson et. al.[66] and Shupe et. al. [49], have overlapping kinematic regimes. The former found agreement ($n = 7.6 \pm 0.7$) with pQCD and the latter disagreement ($n = 8.0 \pm 0.1$). In order to study the behaviour of the total data set the cross section values are scaled by the pQCD factor s^{-7} and shown in Fig. 5.6. There is a clear region around $\cos\theta_{cm} = 0$ where some of the higher s data are not inconsistent with s^{-7} scaling, but there is a considerable amount of spread in the data points even here. It is clear that s^{-7} scaling does not give a good overall description of the data.

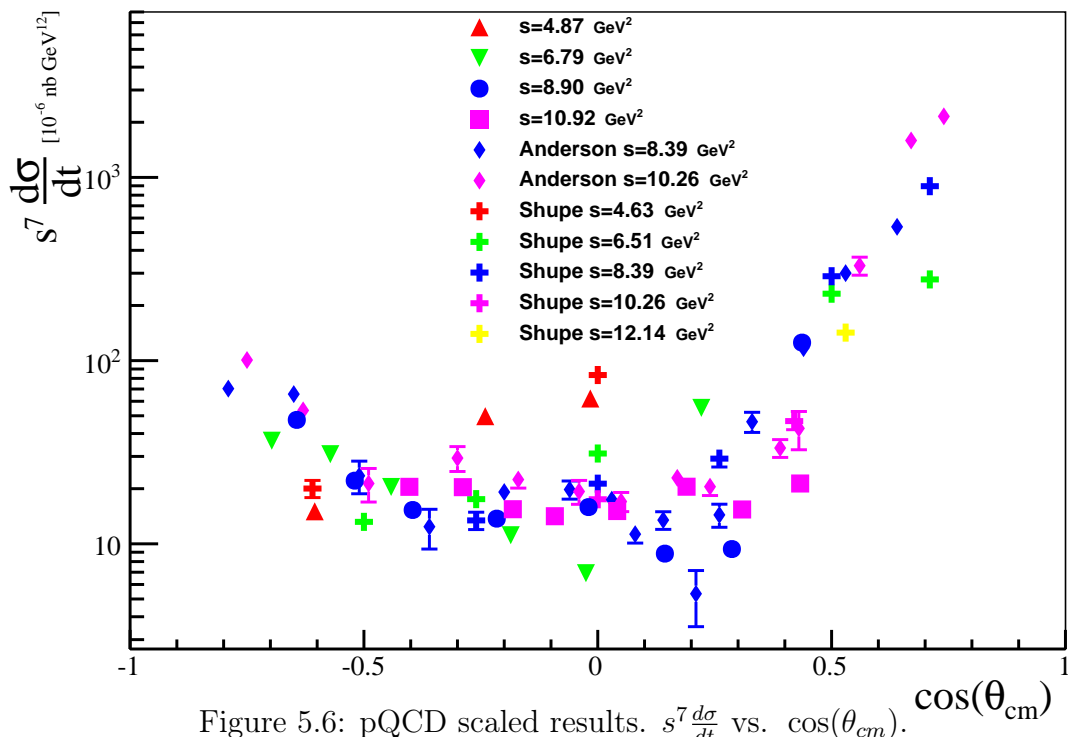


Figure 5.6: pQCD scaled results. $s^7 \frac{d\sigma}{dt}$ vs. $\cos(\theta_{cm})$.

5.2.2 GPDs

The results of Kroll et. al[40], restated in eq. 1.19, should allow an extraction of t -dependant π^0 form factors. The result is presented in Fig. 5.7. Here the results from Ref.[62] have been included as well, albeit with some constraints(high s and wide-angles) put on the data used. Overall the results from the different experiments are fairly consistent and fall approximately on a single curve, independent of s . This curve appears to show a significant dip at $|t| \approx 2.5 \text{ GeV}^2$, but at present it is not

clear if this represents interesting physics.

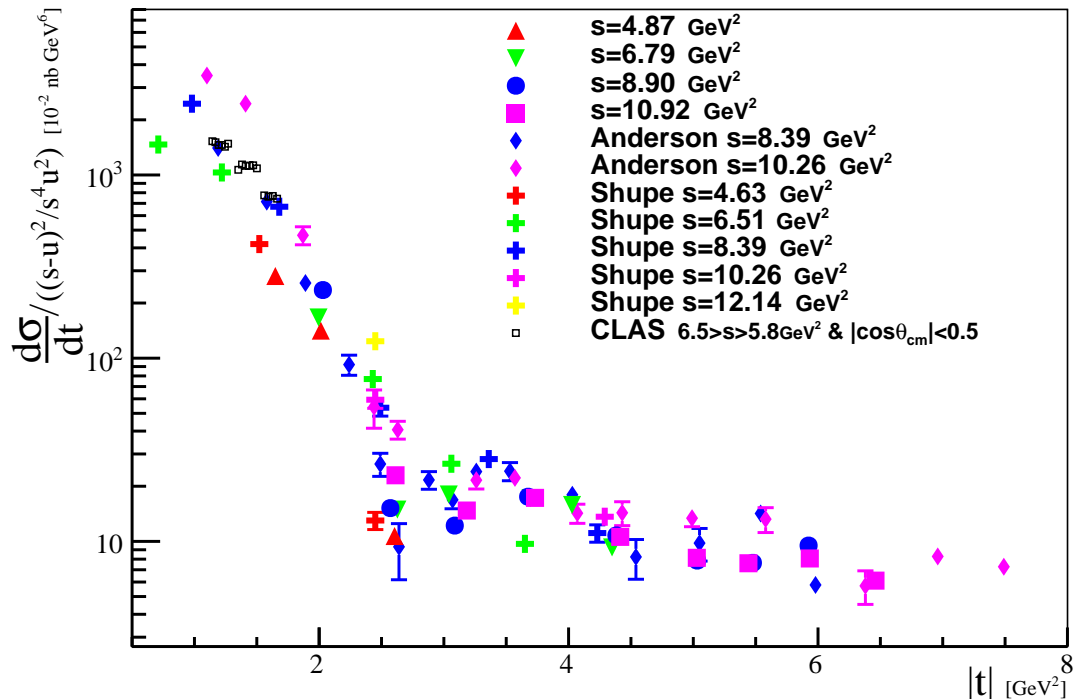


Figure 5.7: GPD scaled results. $\frac{d\sigma/dt}{(s-u)^2/s^4u^2}$ vs. $|t|$.

5.3 Conclusions and Discussion

The results presented here on π^0 -photoproduction in Fig. 5.5 are in poor agreement with a simple scaling law. The compilation of wide-angle π^0 -photoproduction data in Fig. 5.6 shows that the data sets in the wide angle regime have non-negligible differences and that the s^{-7} scaling law of pQCD is an insufficient description of the evolution of the π^0 -photoproduction cross section. Some of the discrepancies between the various measurements could potentially be reconciled if indeed the cross section oscillates around some mean scaling, as seen in pp-scattering[45]. Investigating this possibility requires a larger number of datapoints than is currently available. In the immediate future there are preliminary results from a CLAS measurement using higher beam energies that, once finalised, could perhaps shed some light on this issue. There is also a new wide angle Compton and π^0 -photoproduction experiment planned for Hall-C with the higher energy CEBAF beam. This will extend the measurements into previously untested kinematics and provide a good comparison

with the results presented in this thesis.

It will also be interesting to see whether these new measurements agree with predictions using a GPD based kinematic factor yielding approximately a t -dependent only structure. GPD based predictions have in the past differed from pion experiments by orders of magnitude. This is because the asymptotic value of a , see eq. 1.21, is used in eq. 1.19 as there is presently no other quantitative estimation of that parameter. Assuming the handbag model is applicable these results could be used to test models of this variable, or extract its value for comparison with other experiments.

In short, the results found through the experiment and analysis presented here do not, by themselves or in connection with previous π^0 -photoproduction data, provide a conclusive answer regarding the dominating reaction mechanism and/or the applicability of pQCD and Handbag models. It does add significantly to the world data set and will thus make a valuable contribution to the development of both experiments and theory towards solving these open questions.

Appendix A

Coordinate Systems

The experimental hall coordinate system, denoted in Fig.A.1 as “hall”, is defined so that the z-axis points along the central axis of the electron beam, the y-axis points vertically upwards and the x-axis is defined by $z_{hall} \times y_{hall}$. The origin is the centre of the hydrogen target, which should coincide with the centre of the hall and the rotation centre of the spectrometers.

In the Calorimeter coordinate system, denoted in Fig.A.1 as “calo”, the origin is the same as the “hall” system and the y-axes coincide as well. The vector pointing from the origin to the centre of the calorimeter is defined as the z-axis and the x-axis again is defined as $z_{calo} \times y_{calo}$. In short, the “calo” system is the “hall” system rotated around its y-axis by an angle Θ_{calo} .

The HRS coordinate system, also known as the transport or target system and in Fig. A.1 called “tg”, shares its origin with the other two coordinate systems. Its z-axis is defined by the vector pointing from the origin to the central¹ point of the spectrometer entrance, which is identical to the z-axis obtained when rotating the hall system around its y-axis by an angle Θ_{HRS} . The x-axis is pointing vertically downwards and the y-axis is given by $x_{tg} \times z_{tg}$. In the main text the variables in this coordinate system is referred to as target variables.

There are two other important coordinate systems in use which relate to the detector stack of the HRS. Their definitions are clearly formulated in the ESPACE manual[112]

¹This is the central point of the central hole in the sieve slit used for dedicated optics runs.

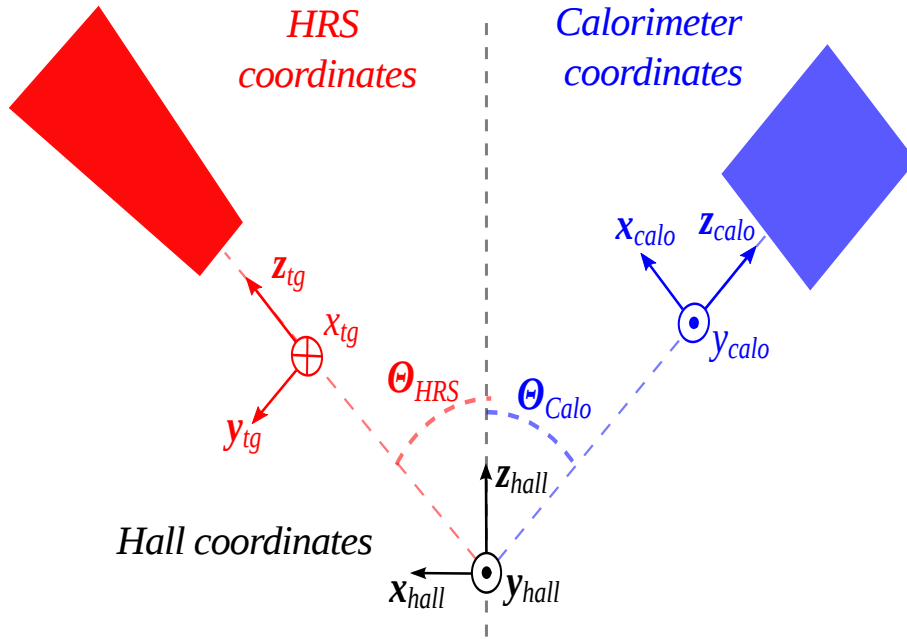


Figure A.1: Coordinate systems and their relation to each other.

and they are quoted below. The two coordinate systems' relation to the VDCs and to each other is visualised in fig.A.2. Note that the variables in the Focal-Plane coordinate system are simply called focal plane variables in the main text.

“The origin of the spectrometer detector coordinate system is defined by the intersection of wire 184 in the first plane and the projection on the first wireplane of wire 184 in the second plane (assuming 368 wires in each plane). The z axis is perpendicular to the wireplanes and its direction is fixed by demanding that its product with the central spectrometer ray is larger than zero. The x axis is defined as the projection on the first wire plane of the vector difference between the spectrometer central ray and a ray for which the momentum has been increased by an infinitesimal amount. Its direction is fixed by requiring an increase in momentum. It would be optimal if the x - z plane would coincide with the spectrometer symmetry plane.” -ESPACE manual[112].

“The spectrometer Focal-Plane coordinate system shares its origin with the detector system and the x - z planes coincide. However, its z -axis (and therefore also its x -axis) has a different orientation. The z axis

is defined as the projection of the local central ray on the x-z plane. The consequence is that x and z are a function of the fractional particle momentum $\Delta p/p$.” -ESPACE manual²[112].

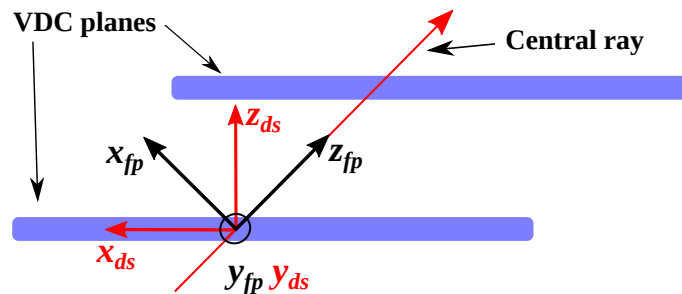


Figure A.2: Coordinate systems for the detector stack in the HRS

²In the last sentence of this quotation, just after "x and z" a word "axis" has been omitted from the original text as this is an obvious typo.

Appendix B

Reaction Reconstruction

A fundamental part of this analysis is the recreation of the scattered/photoproduced particle-X kinematics from the proton data assuming X is either a scattered gamma/electron or a photoproduced π^0 . Since in general the central momentum P_{HRS} as well as the angle of the HRS, Θ_{HRS} , is known it is possible to reconstruct the proton four-momentum in the lab frame. First one calculates the angle of the proton trajectory with respect to the central z axis in the HRS system

$$\cos \theta_z^{HRS} = \frac{1}{\sqrt{1 + \tan^2 \theta_{tg} + \tan^2 \phi_{tg}}} \quad (\text{B.0.1})$$

where $\theta_{tg} \equiv dx_{tg}/dz_{tg}$ and $\phi_{tg} \equiv dy_{tg}/dz_{tg}$. The three-momentum vector components in the HRS system are given by

$$\begin{aligned} p_x^* &= P_p \cos \theta_z^{HRS} \tan \theta_{tg}, \\ p_y^* &= P_p \cos \theta_z^{HRS} \tan \phi_{tg}, \\ p_z^* &= P_p \cos \theta_z^{HRS} \end{aligned} \quad (\text{B.0.2})$$

where $P_p = \delta \cdot P_{HRS} + P_{HRS}$ is the proton momentum, and δ is the fractional momentum deviation from the central momentum. The vector is transformed into

the Hall frame by

$$\begin{aligned}
 p_x &= p_y^* \cos \Theta_{HRS} + p_z^* \sin \Theta_{HRS} \\
 p_y &= -p_x^* \\
 p_z &= -p_y^* \sin \Theta_{HRS} + p_z^* \cos \Theta_{HRS}
 \end{aligned}
 \tag{B.0.3}$$

where Θ_{HRS} is the spectrometer angle. It is now trivial to calculate the protons scattering angle with respect to the z-axis of the hall,

$$\cos \theta_z = p_z / P_p.
 \tag{B.0.4}$$

Having derived these quantities for the proton one can compute the energy of the incoming particle as well as the energy and momentum of X by

$$\begin{aligned}
 E_{in,X} &= \frac{M_p(E_p - M_p) + M_X^2}{M_p - E_p + P_p \cos \theta_z} \\
 E_X &= E_{in,X} - E_p + M_p \\
 P_X &= \sqrt{E_X^2 - M_X^2}
 \end{aligned}
 \tag{B.0.5}$$

where M_p is the proton mass and M_X is either the electron/ γ mass ($M_e \approx M_\gamma = 0$) or the π^0 mass ($M_\pi \approx 134.97$). The scattering angles can then be calculated via

$$\begin{aligned}
 \cos \theta_X &= \frac{E_{in,X} E_X - M_p(E_p - M_p) - \frac{1}{2} M_X^2}{E_{in,X} \cdot P_X} \\
 \sin \phi_X &= -\frac{p_y}{P_X \sin \theta_X}.
 \end{aligned}
 \tag{B.0.6}$$

Next, the four-vector of the scattered/produced particle X is obtained through

$$\begin{aligned}
 p_{X,x} &= -P_X \sin \theta_X \cos \phi_X \\
 p_{X,y} &= P_X \sin \theta_X \sin \phi_X \\
 p_{X,z} &= P_X \cos \theta_X.
 \end{aligned}
 \tag{B.0.7}$$

and after rotation by the Calorimeter angle Θ_{Calo} one gets

$$\begin{aligned}
 p_{Calo,x} &= p_{e,x} \cos \Theta_{Calo} + p_{e,z} \sin \Theta_{Calo} \\
 p_{Calo,y} &= p_{e,y} \\
 p_{Calo,z} &= -p_{e,x} \sin \Theta_{Calo} + p_{e,z} \cos \Theta_{Calo}
 \end{aligned} \tag{B.0.8}$$

which are the momentum components in the Calorimeter frame. The angles in this frame are

$$\begin{aligned}
 \tan \theta_{Calo} &= \frac{p_{Calo,x}}{p_{Calo,z}} \\
 \sin \phi_{Calo} &= \frac{p_{Calo,y}}{p_{Calo,z}}
 \end{aligned} \tag{B.0.9}$$

which gives the projected hit positions

$$\begin{aligned}
 X_{HRS} &= x_0 + D\theta_{Calo} \\
 Y_{HRS} &= D\phi_{Calo}
 \end{aligned} \tag{B.0.10}$$

with

$$\begin{aligned}
 x_0 &= z_v \sin \Theta_{Calo} \\
 D &= D_0 - z_v \cos \Theta_{Calo} \\
 z_v &= -y_{tg} / (\sin \Theta_{HRS} + \phi_{tg} \cdot \cos \Theta_{HRS})
 \end{aligned} \tag{B.0.11}$$

where D_0 is the distance from the target to the Calorimeter. The hit positions measured by the calorimeter itself are denoted X_{Calo} and Y_{Calo} and the difference of these positions

$$\begin{aligned}
 dX &= X_{Calo} - X_{HRS} \\
 dY &= Y_{Calo} - Y_{HRS}
 \end{aligned} \tag{B.0.12}$$

are essential to the analysis.

Finally, it is useful to use the angle between the reconstructed X momentum

vector and the vector pointing from the reaction vertex in the target to the hit position on calorimeter to predict the energy of a single detected photon from the pion decay via

$$E_{\gamma_{\pi^0}} = \frac{m_{\pi^0}/2}{\gamma(1 - \beta \cos \theta_{\gamma,\pi^0})} \quad (\text{B.0.13})$$

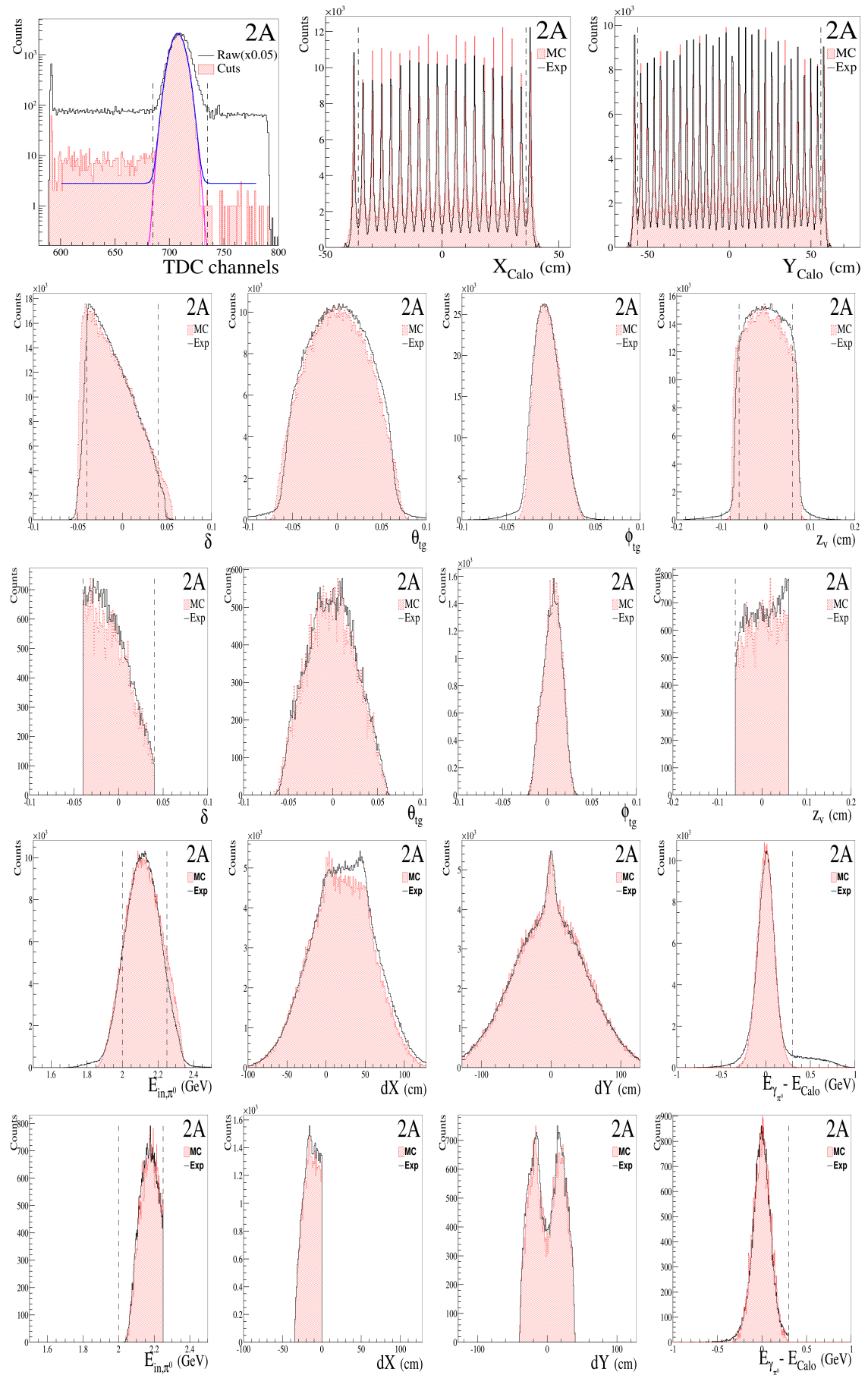
where θ_{γ,π^0} is the angle between the reconstructed X vector and the vector from the reaction vertex to the calorimeter hitposition. $E_{\gamma_{\pi^0}}$ can then be compared to the energy deposit measured in the calorimeter.

Appendix C

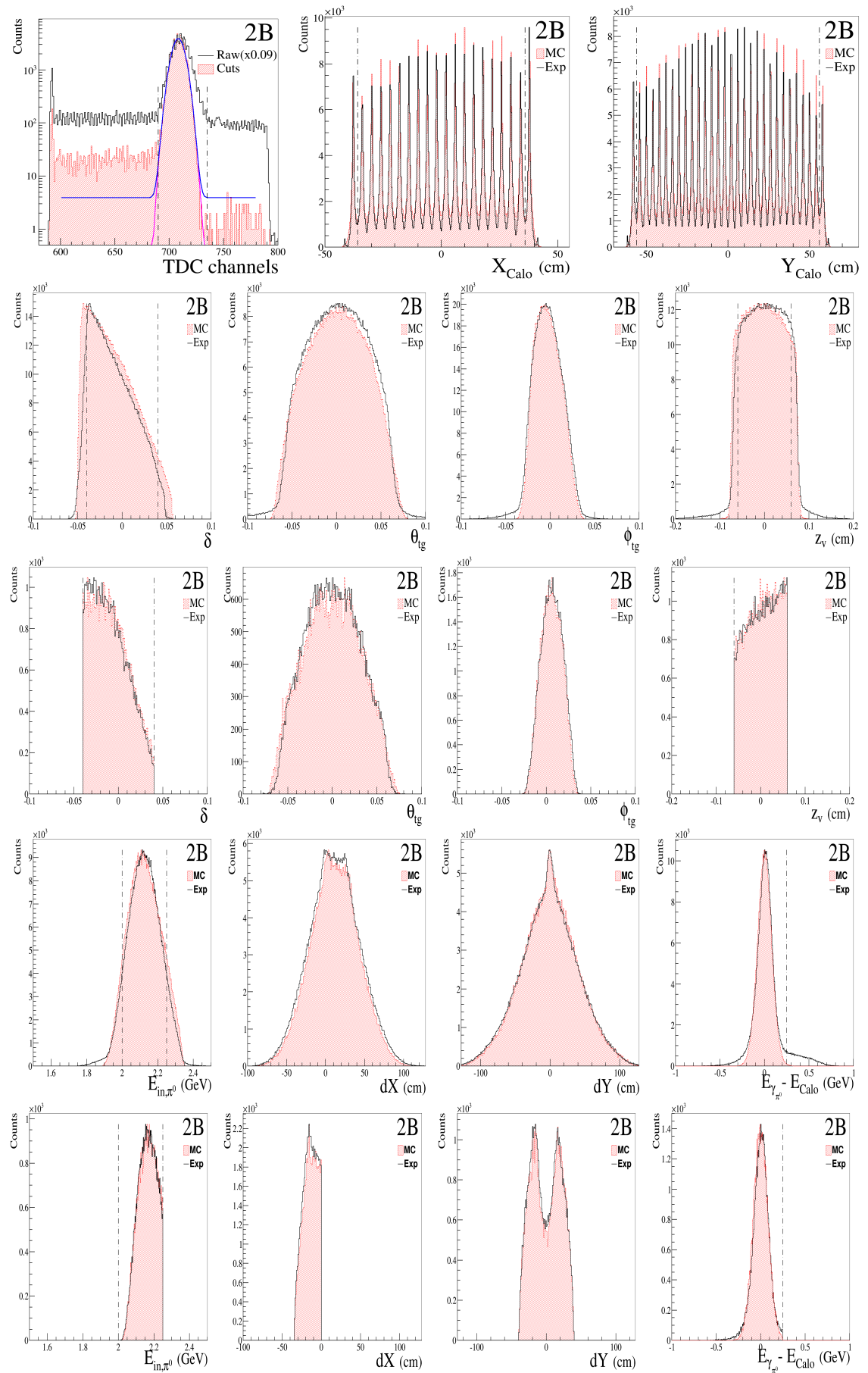
Distributions for all Kinematic Points

Chapter 4 showed only the plots from four kinematic points. In the following, plots corresponding to those shown in Section 4.3 are presented for all kinematic points. The one exception is the 2-dimensional hit position seen in Fig. 4.20. The first row shows the timing and raw calorimeter hit positions. The second and third rows show the raw and final distributions of the HRS variables. The fourth and fifth rows show the reduced and final distributions of the reconstructed beam energy, hit position differences in X and Y and energy difference.

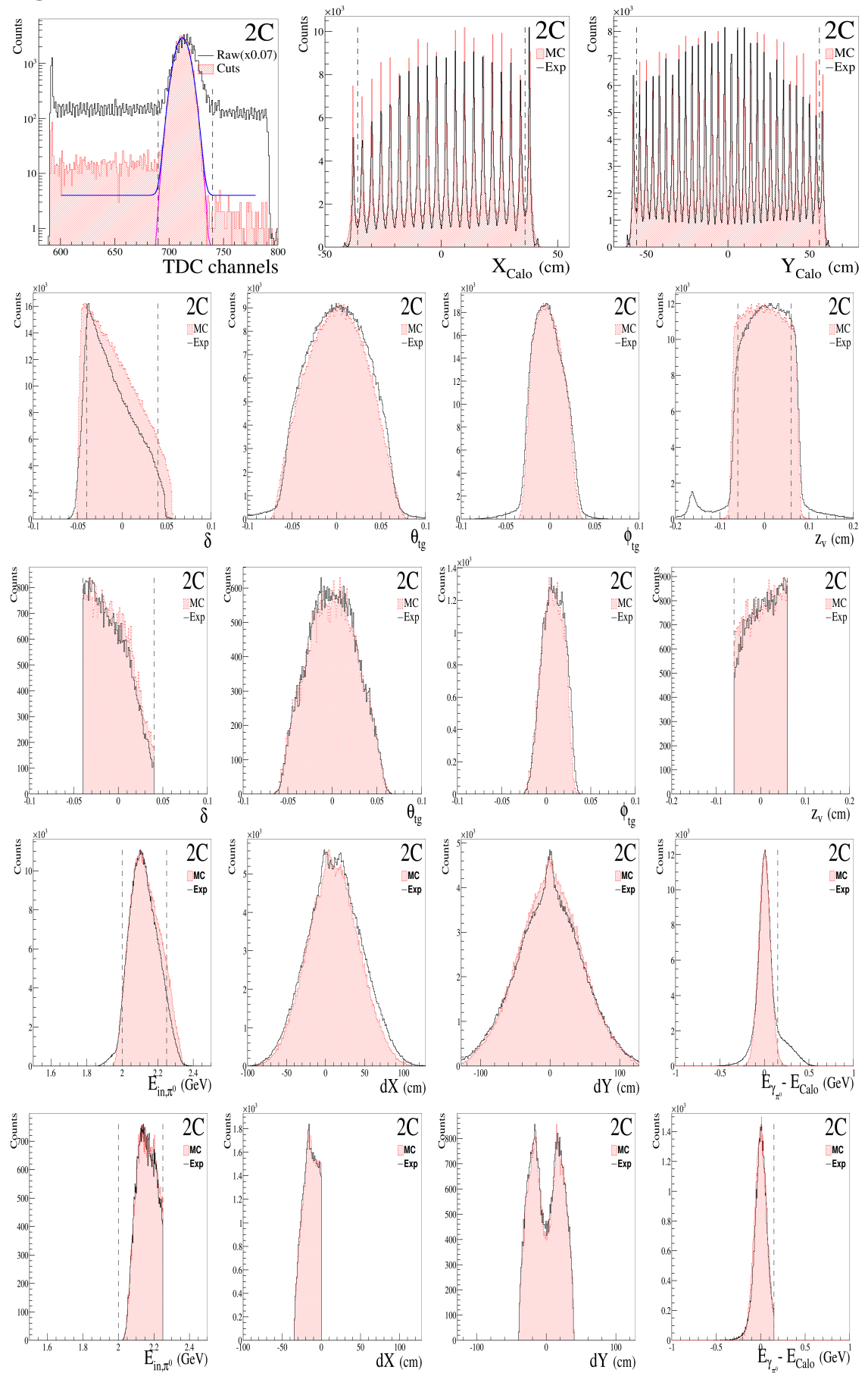
2A



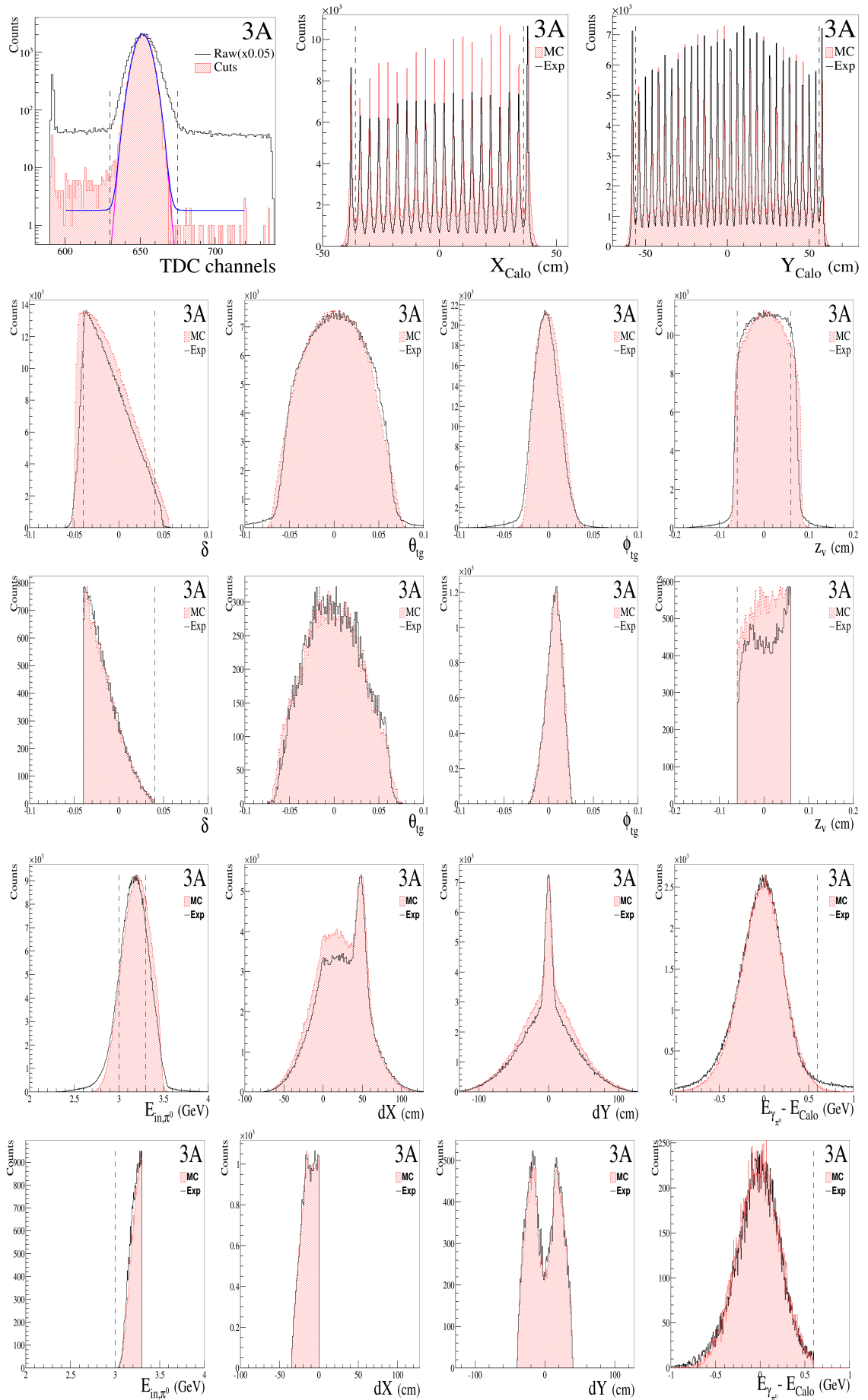
2B



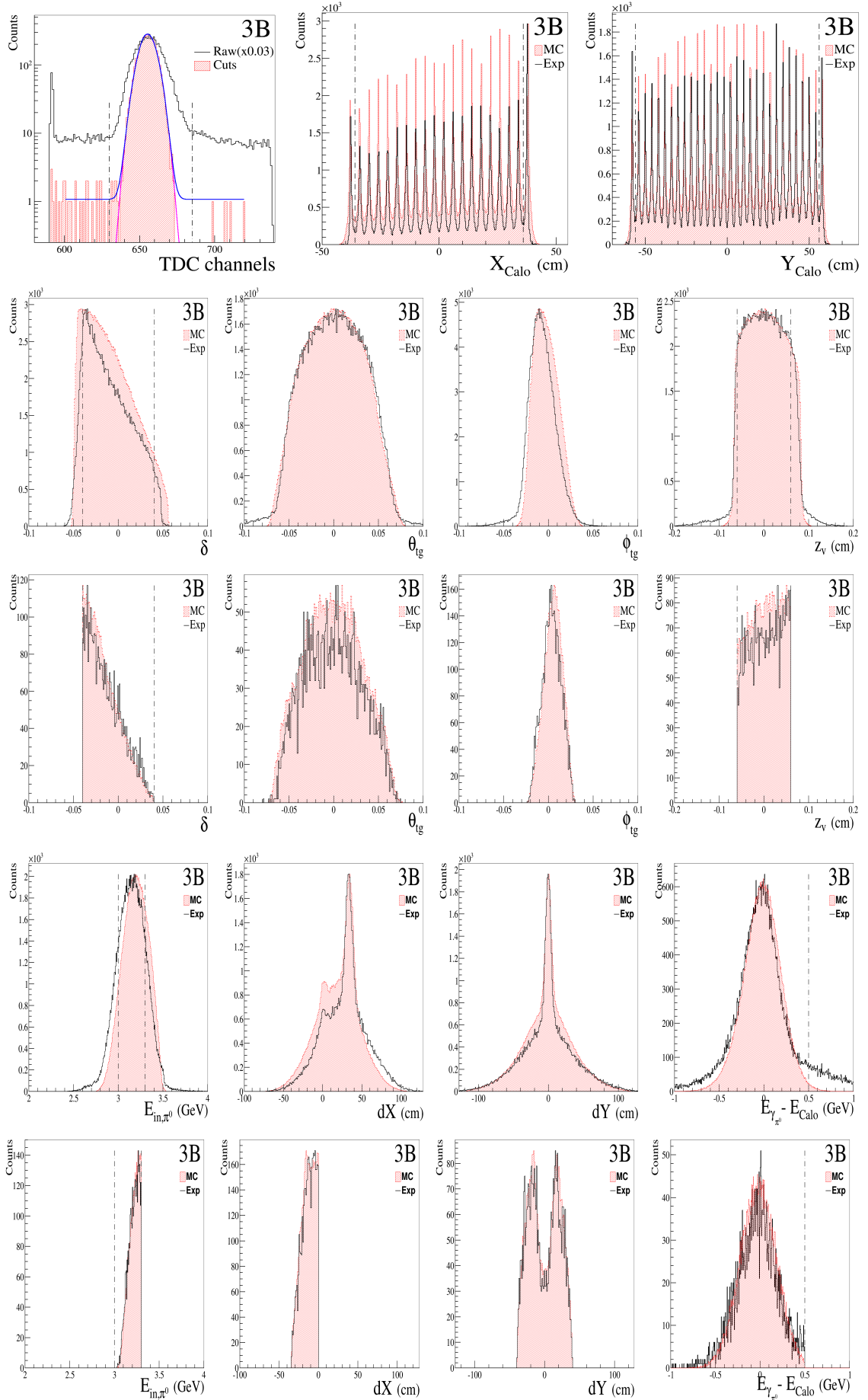
2C



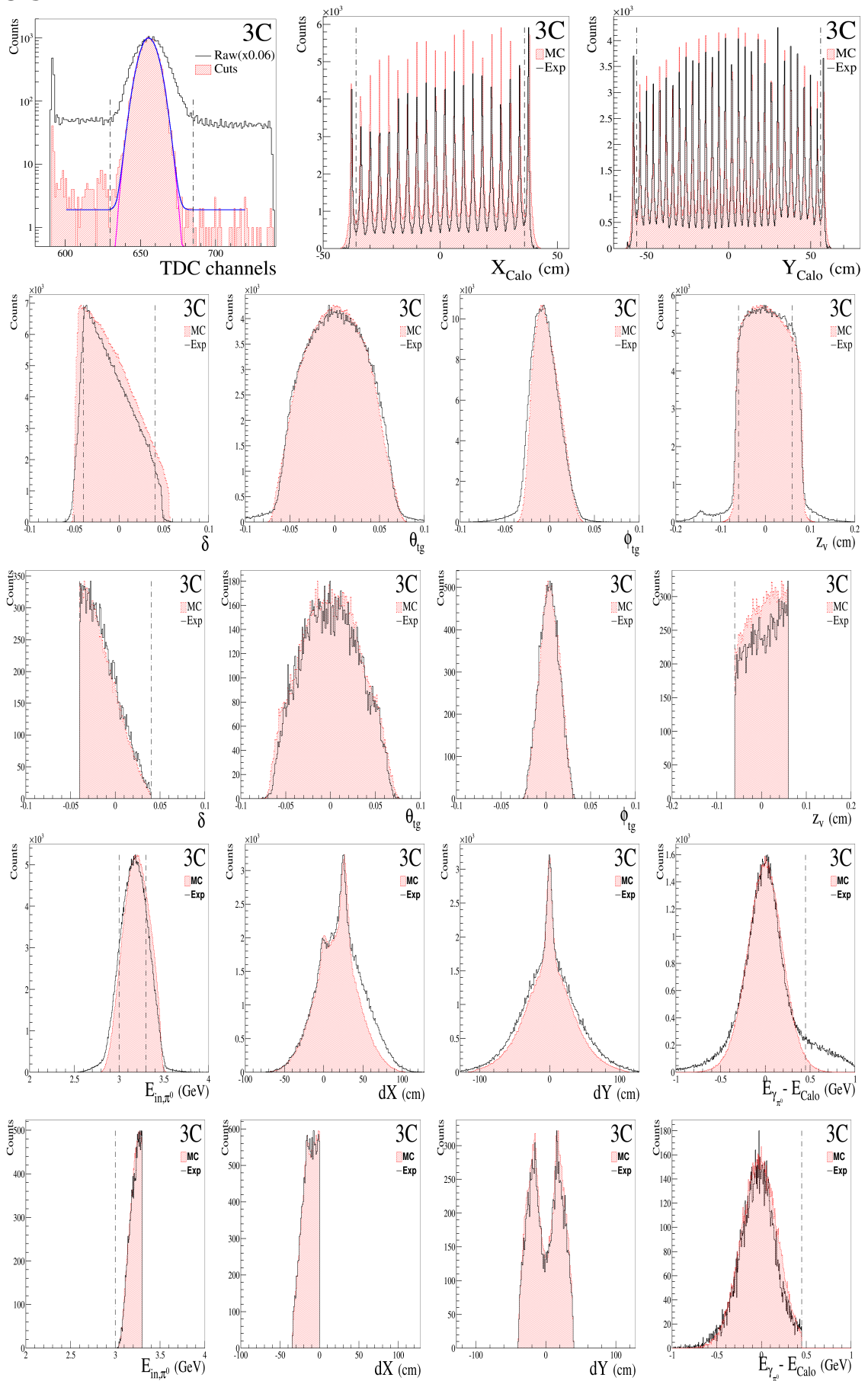
3A



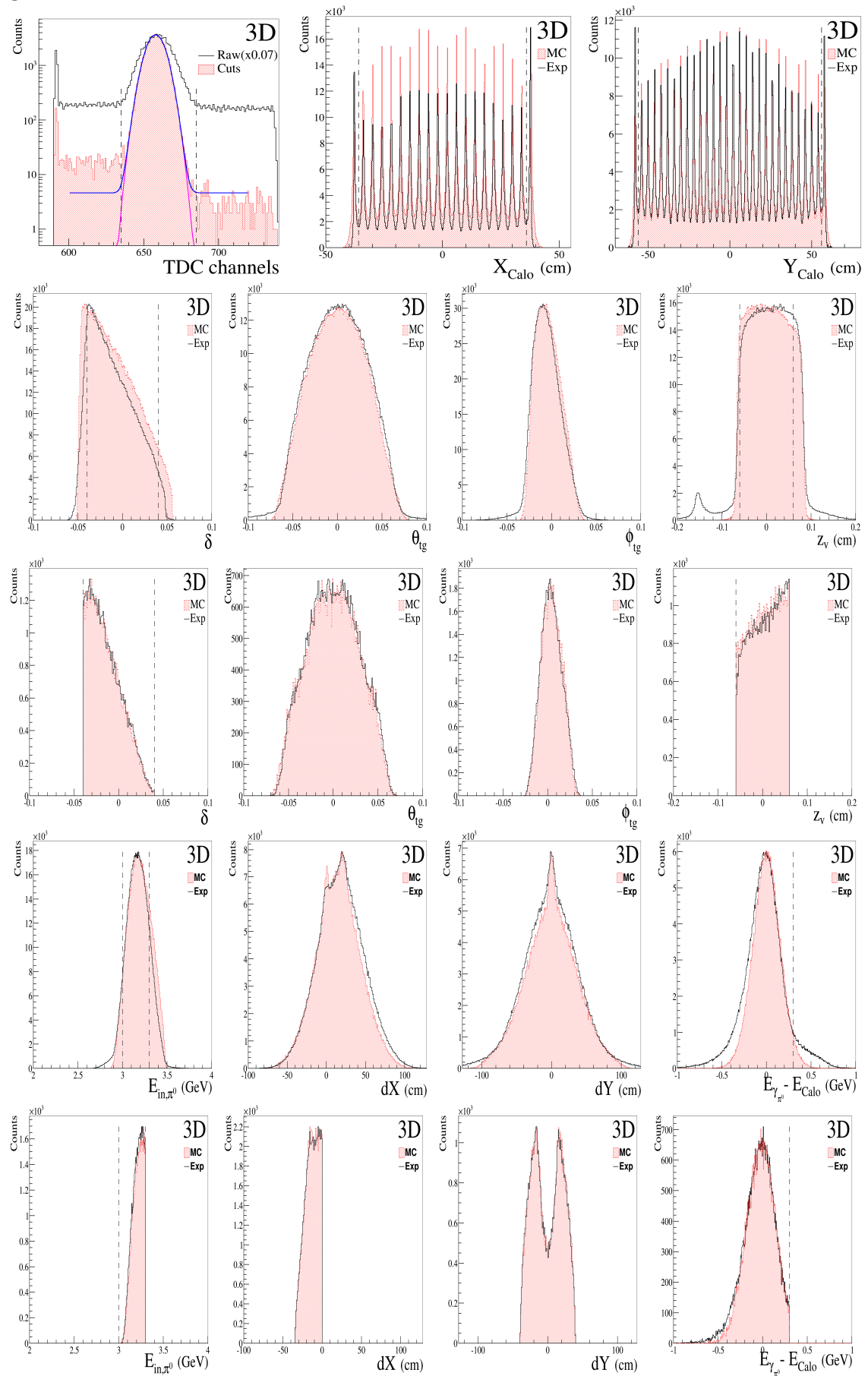
3B



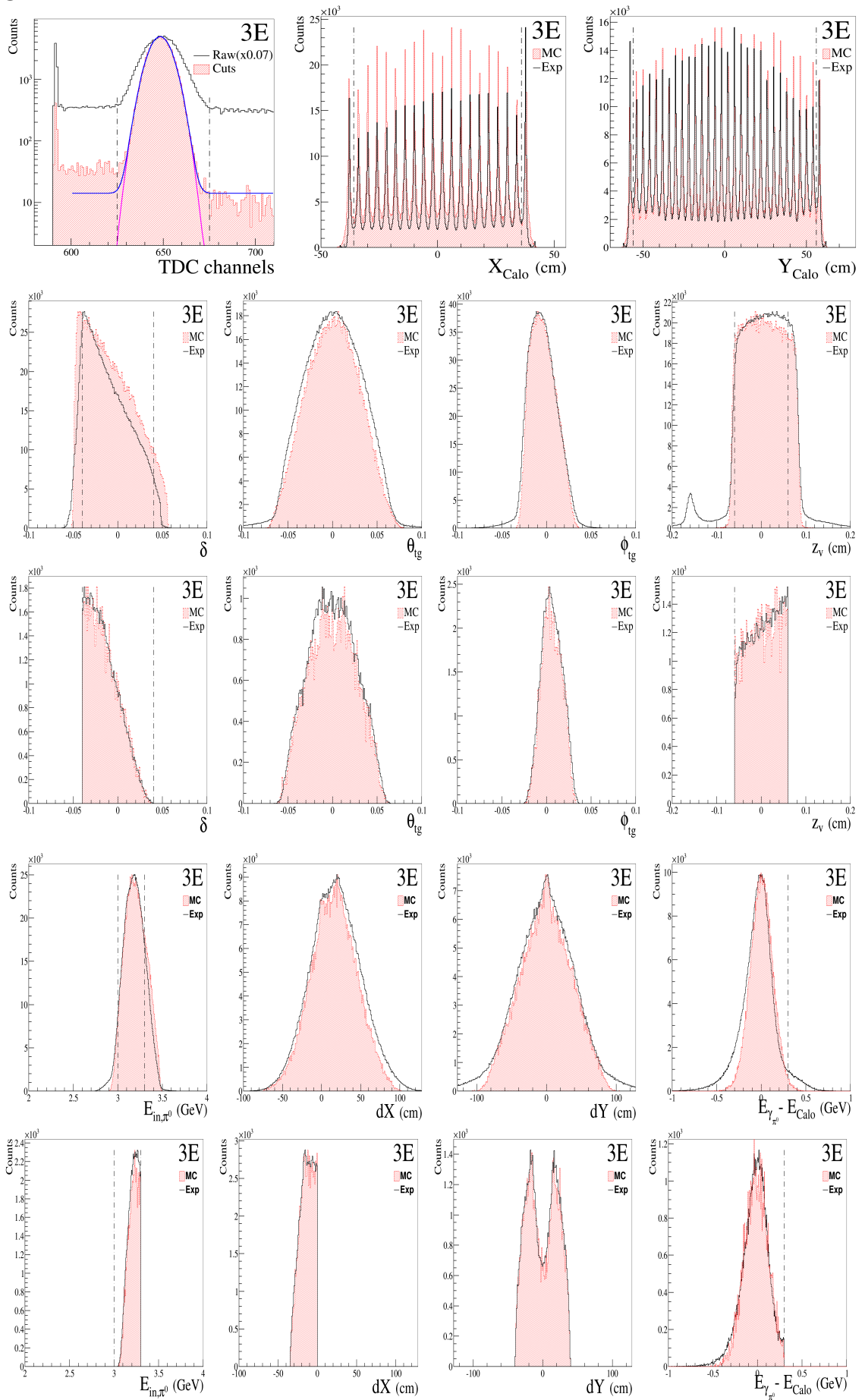
3C

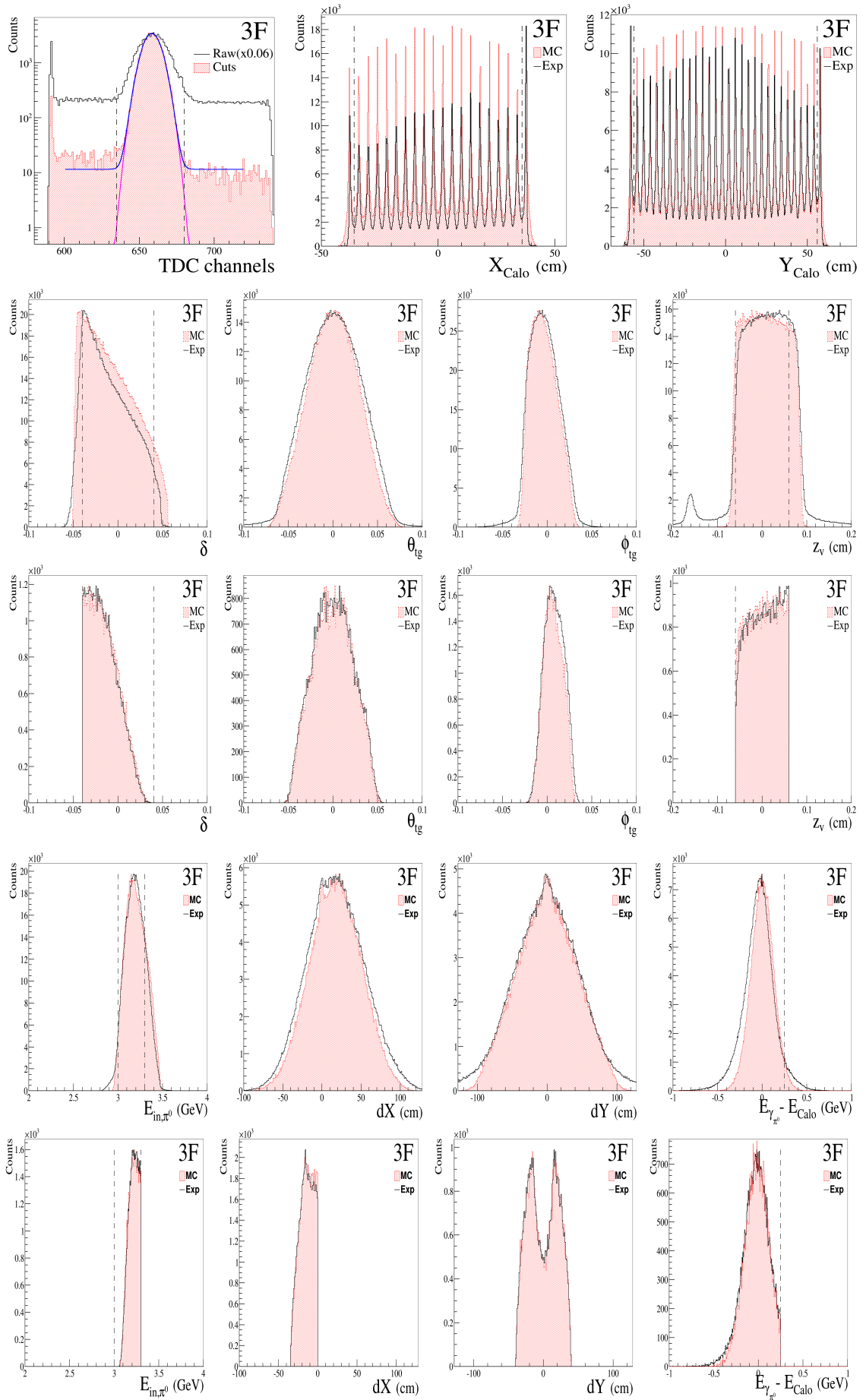


3D

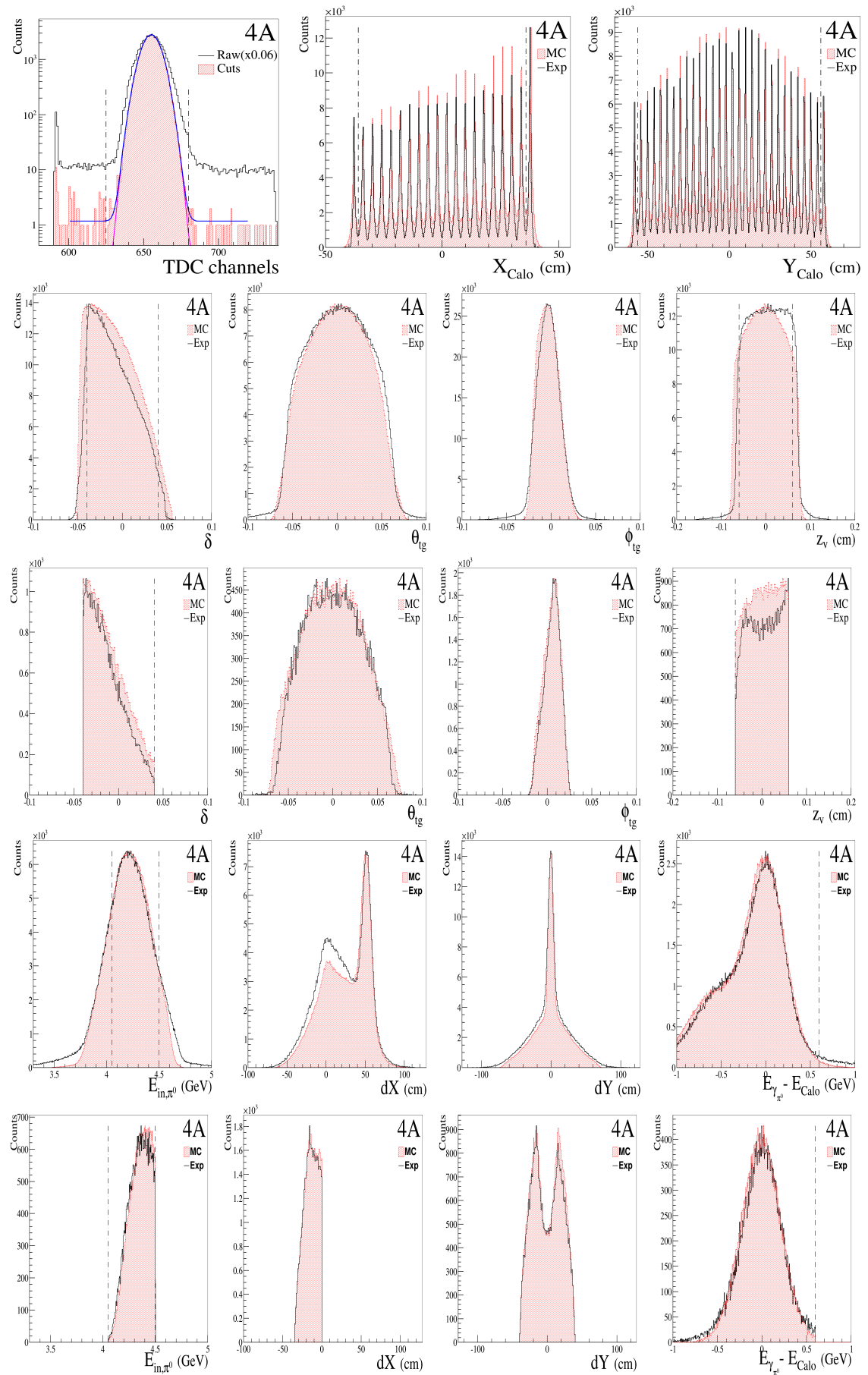


3E

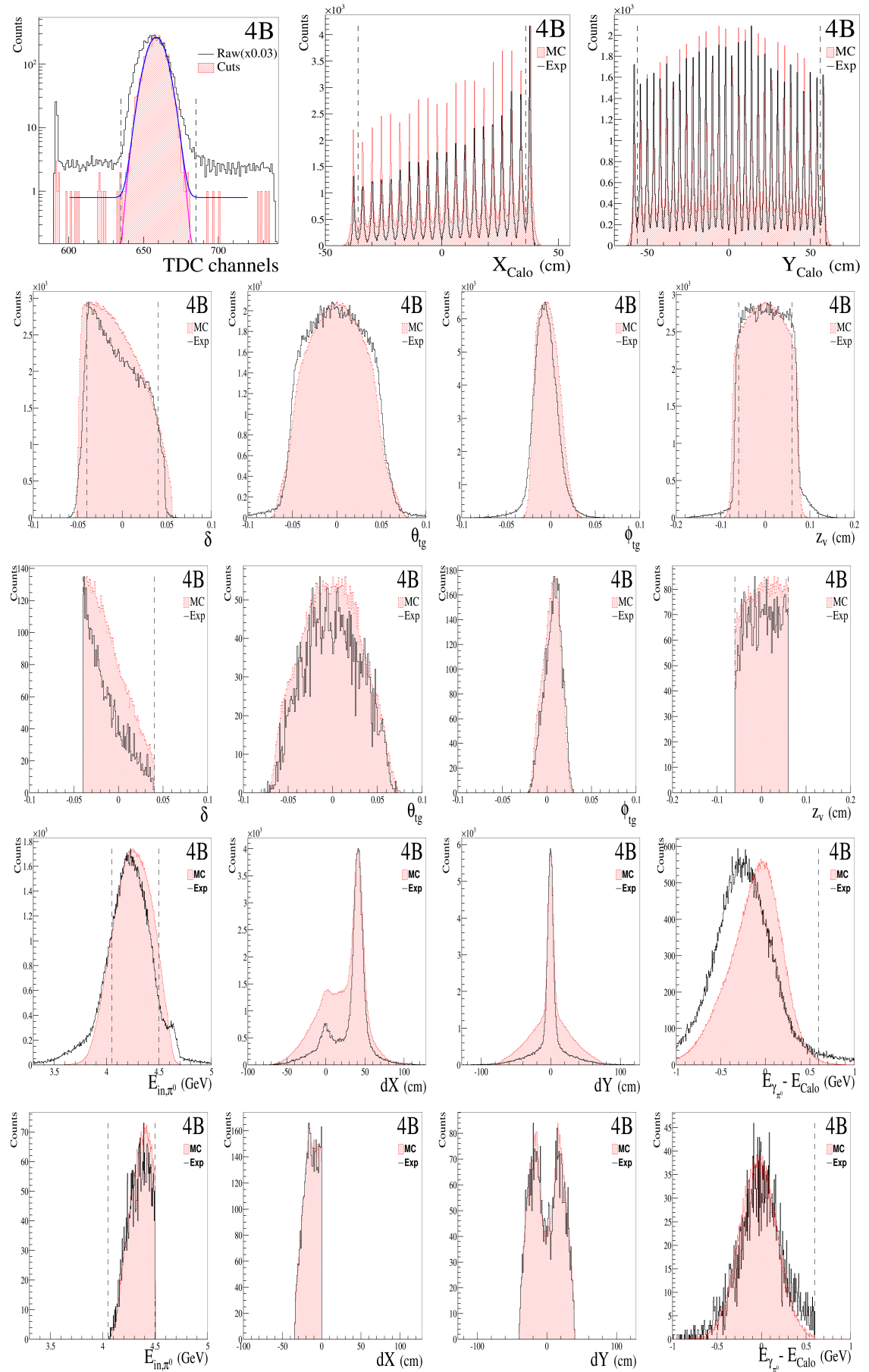


3F


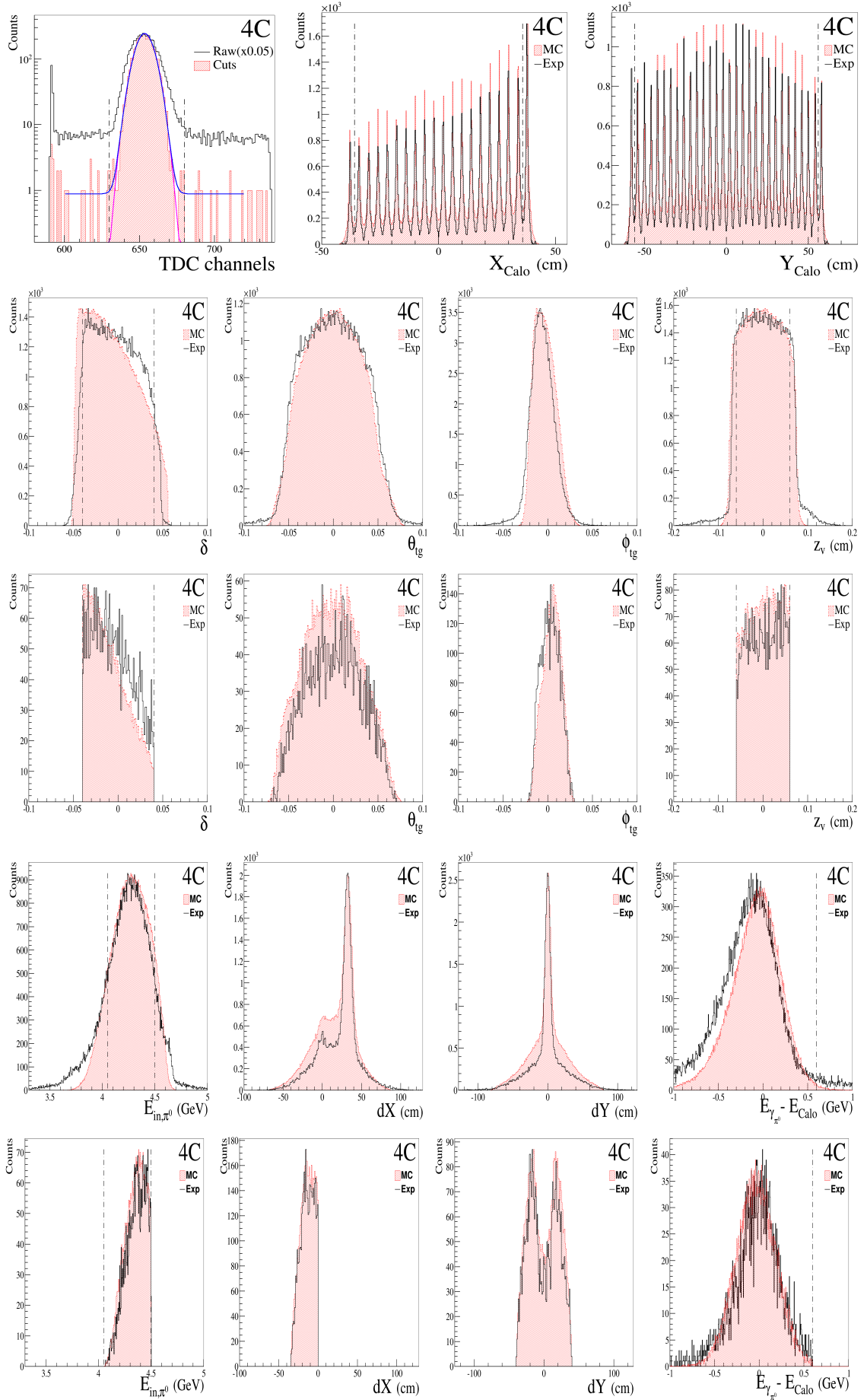
4A



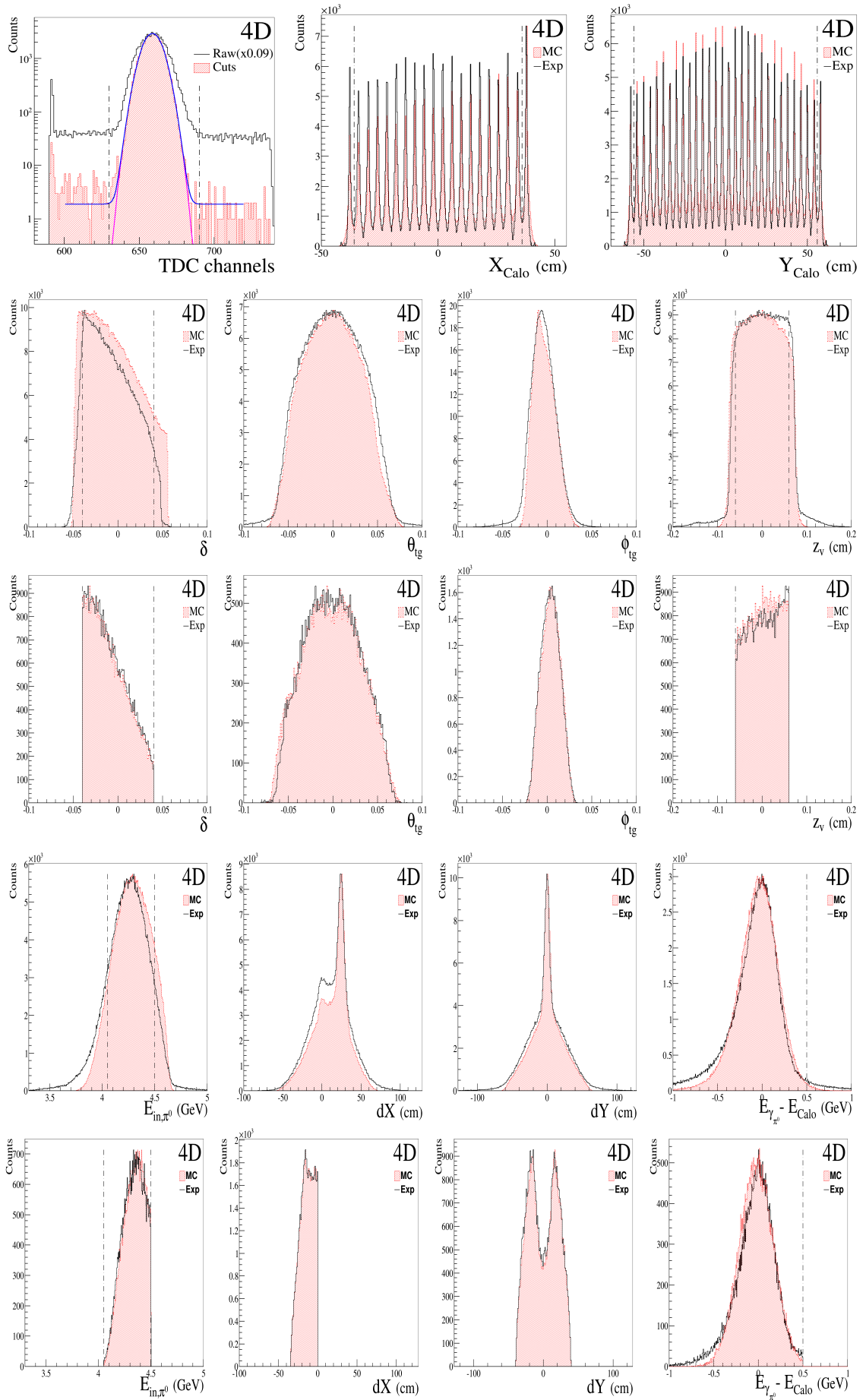
4B

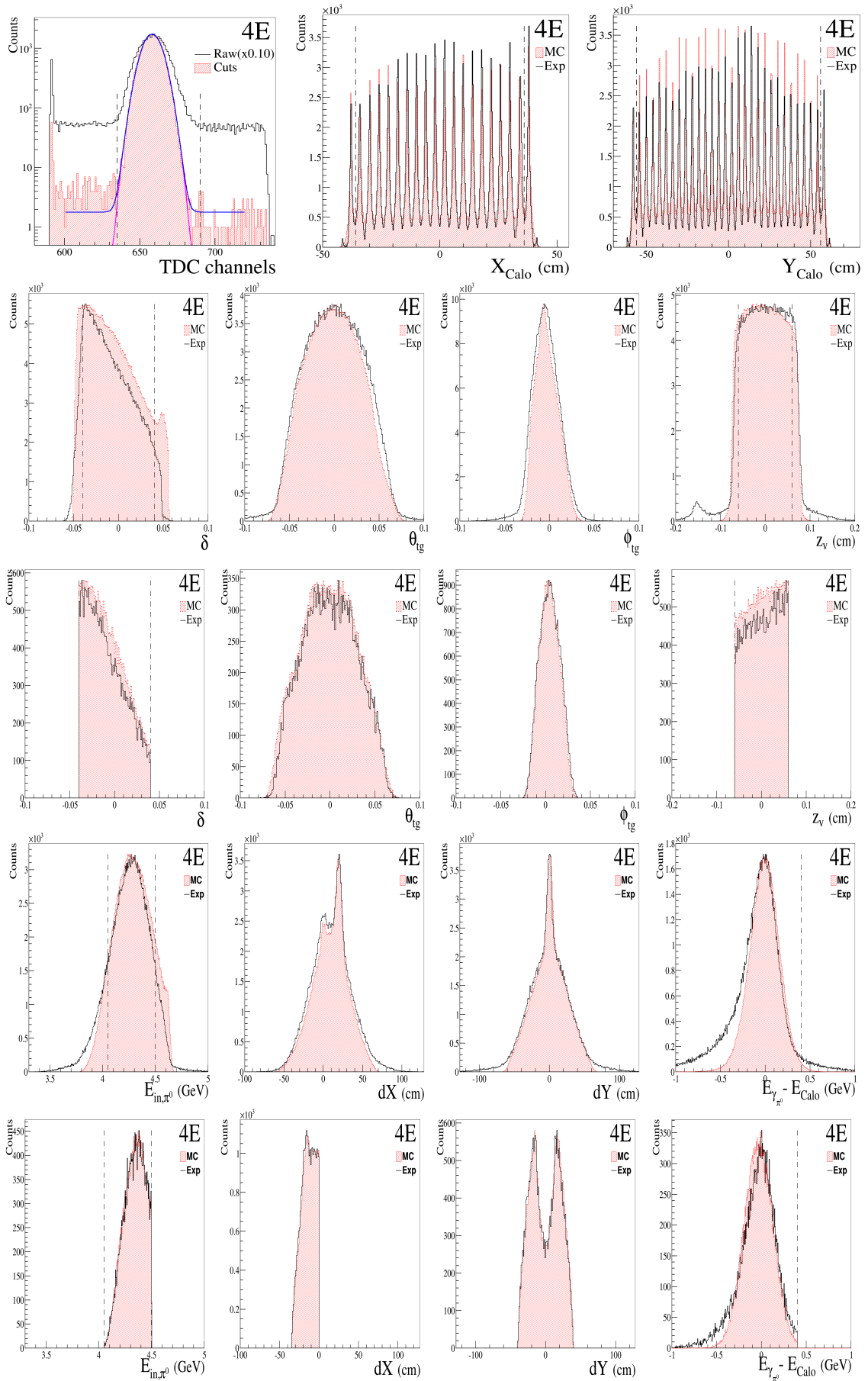


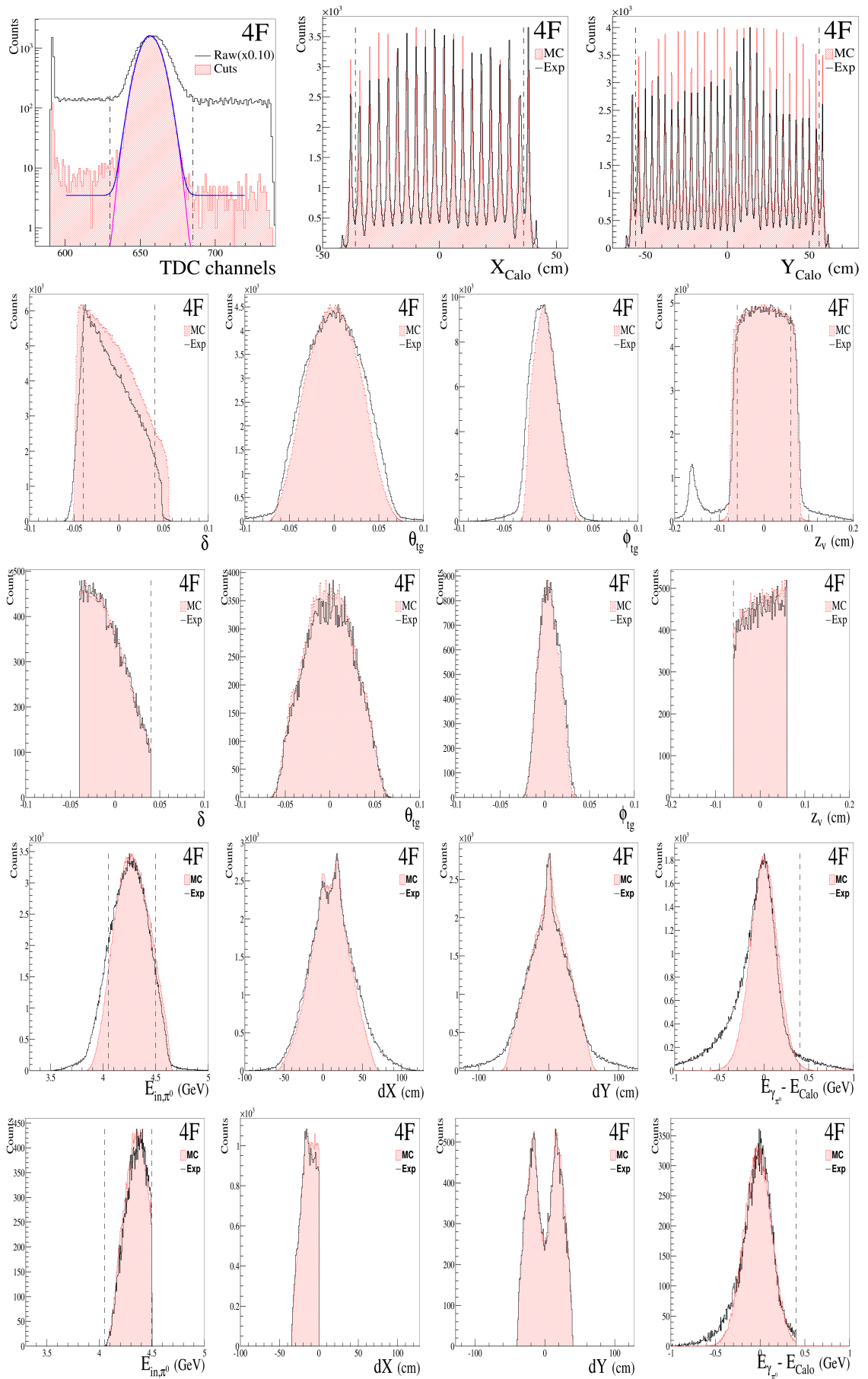
4C



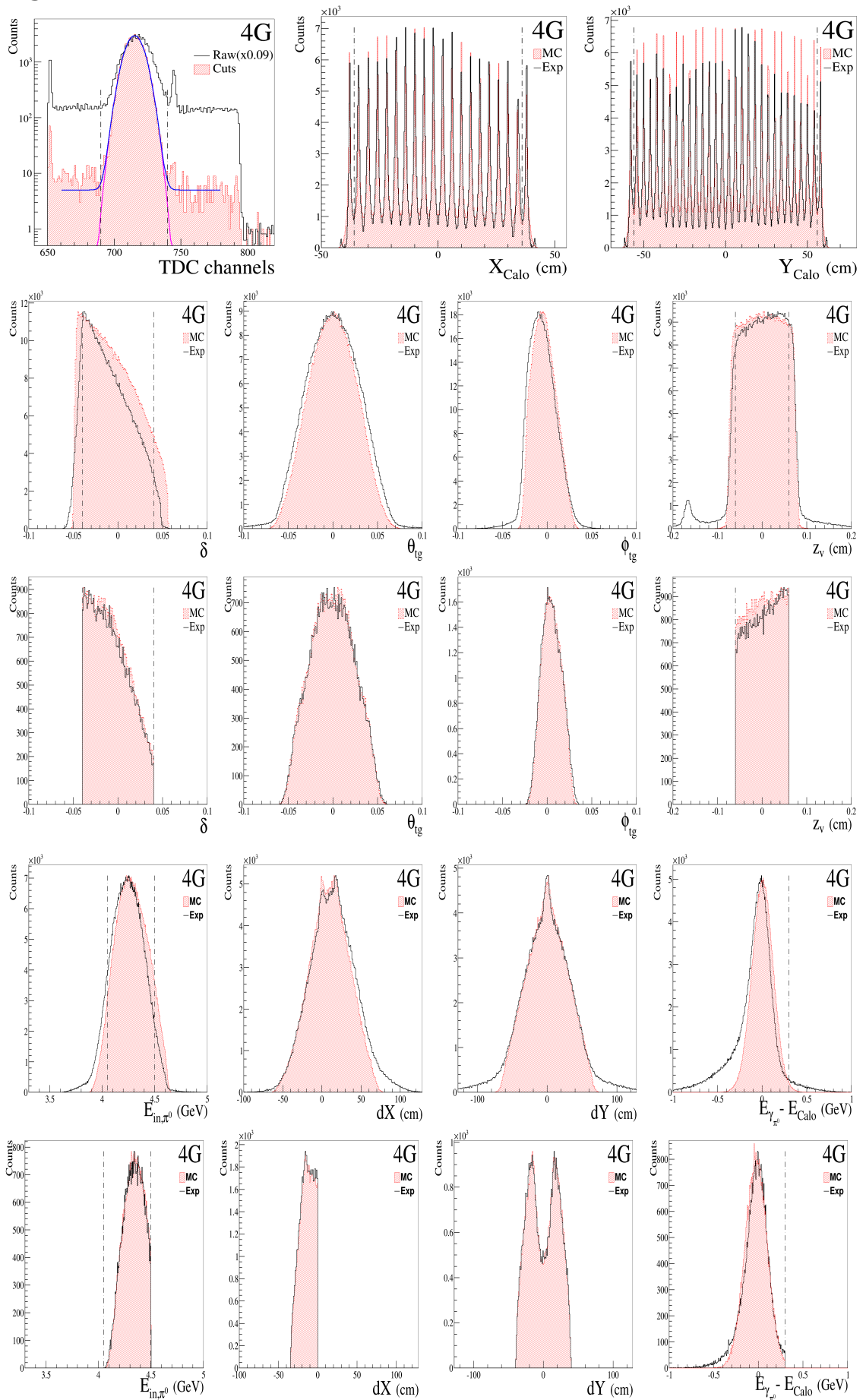
4D



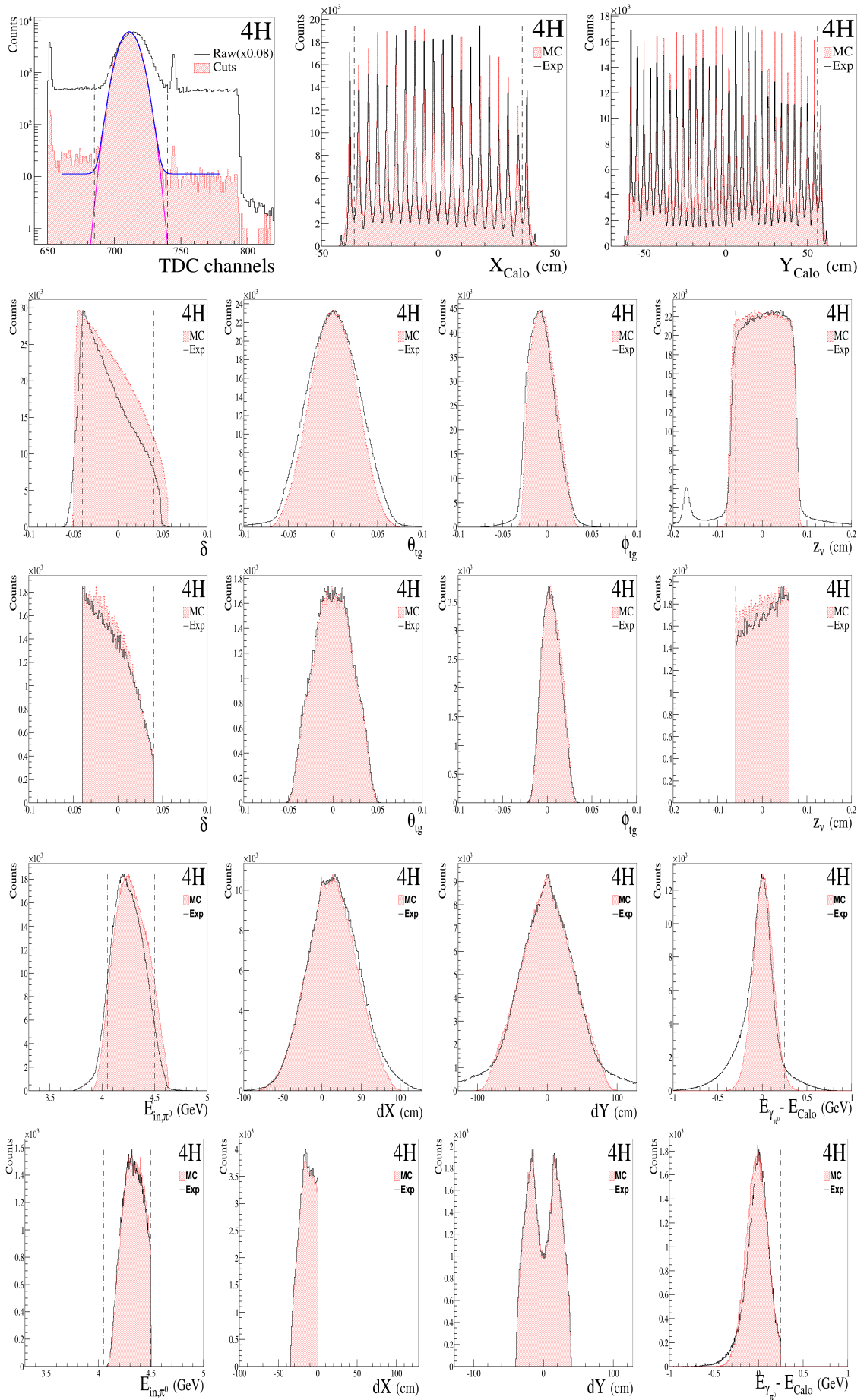
4E


4F


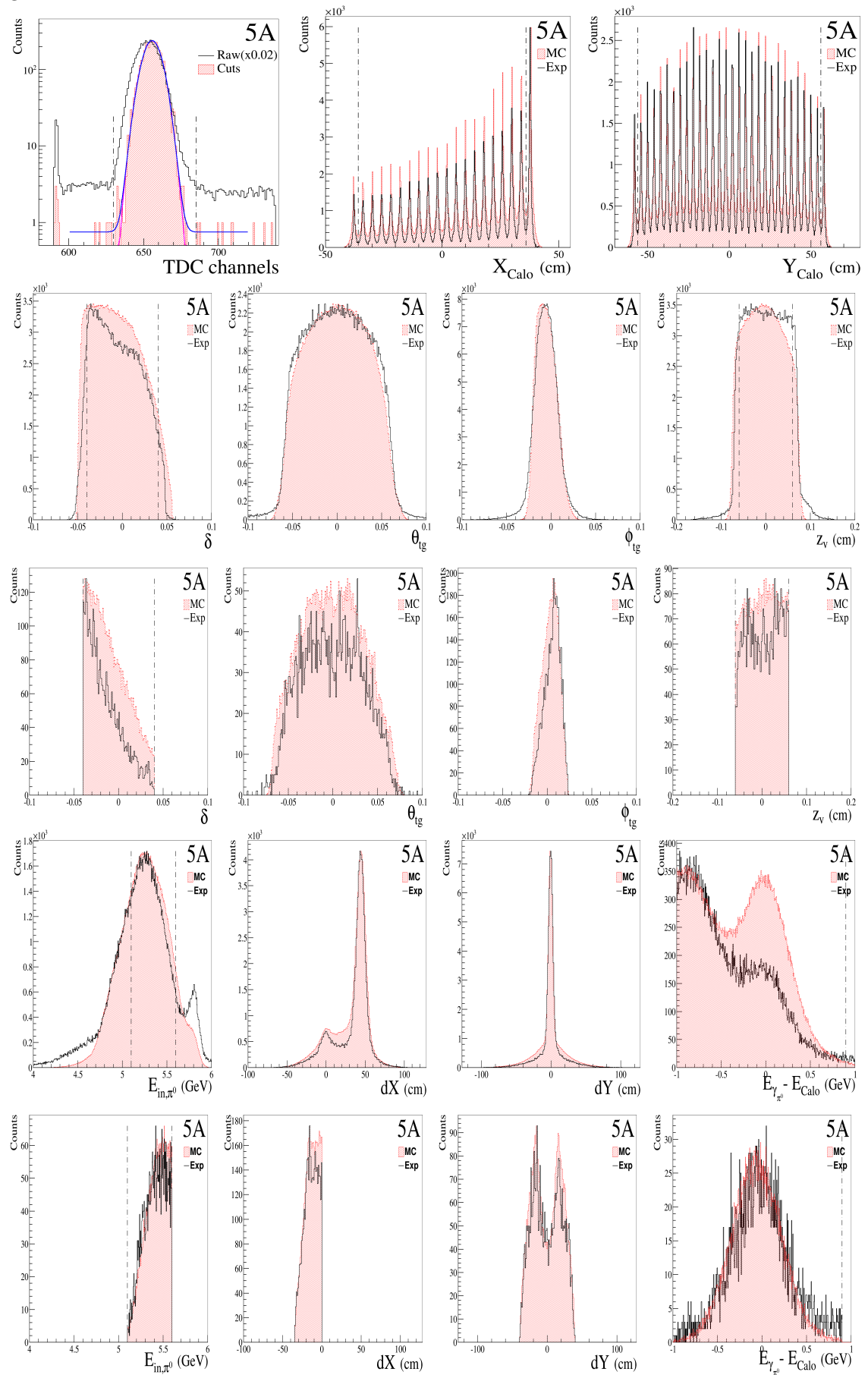
4G



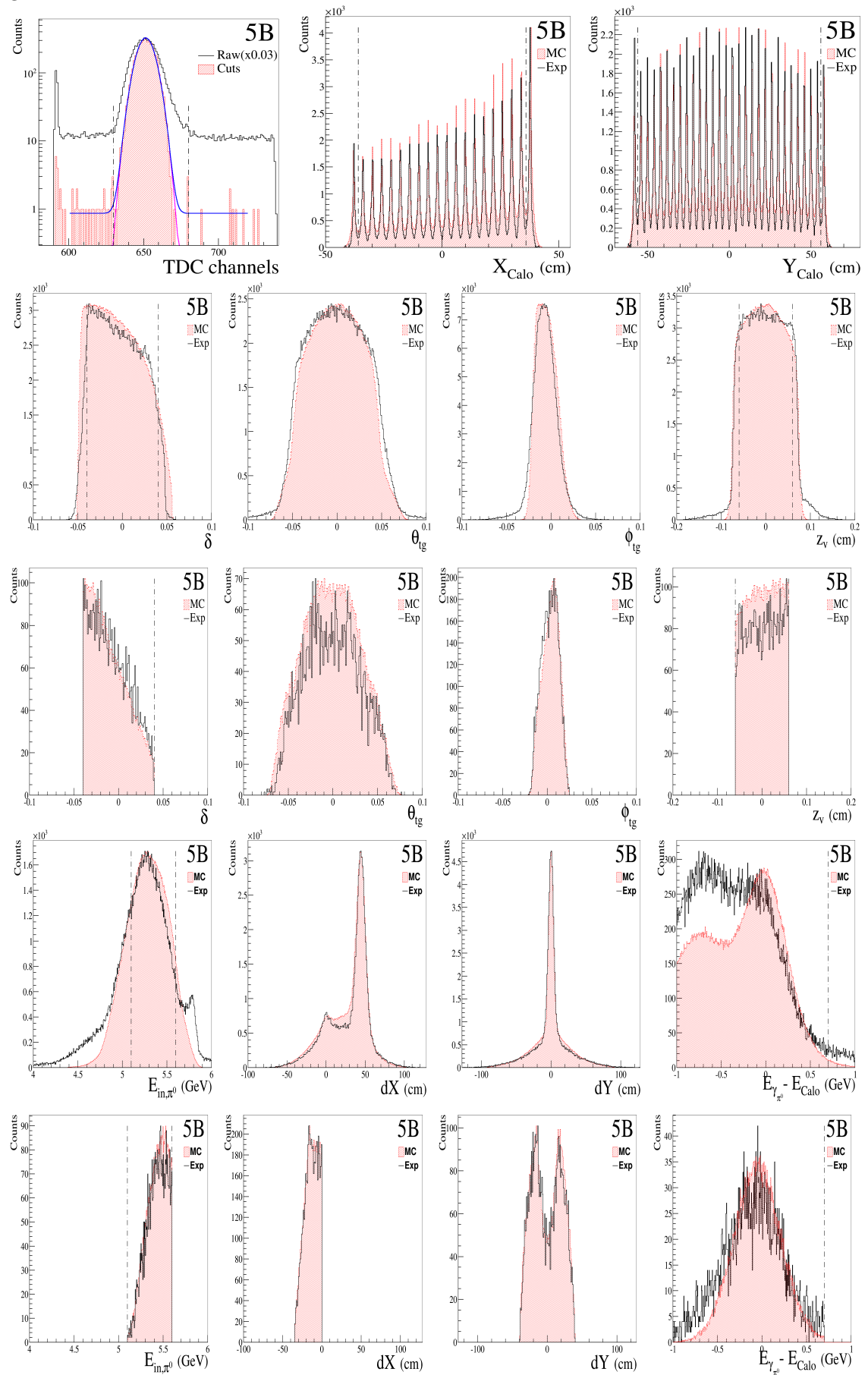
4H



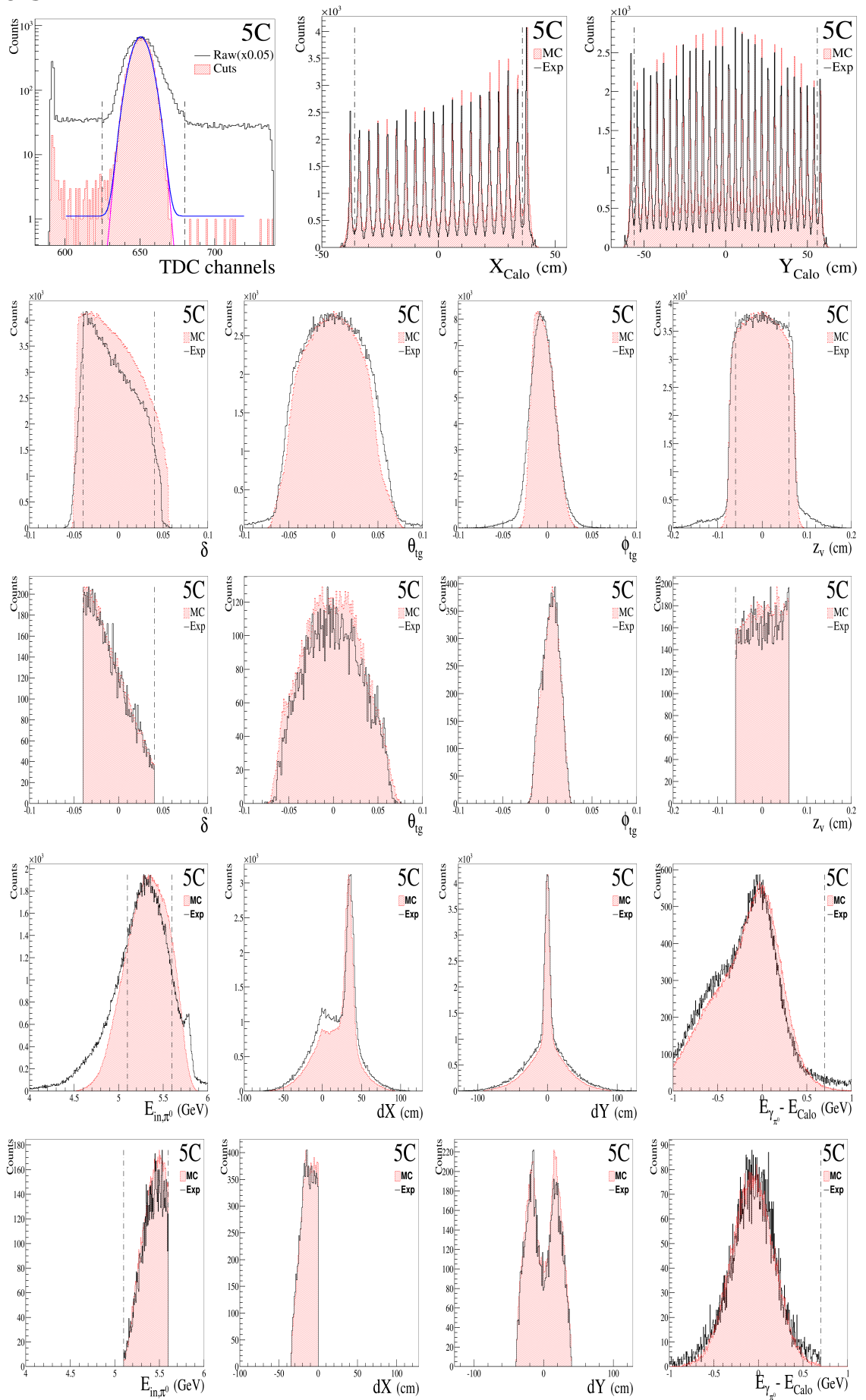
5A



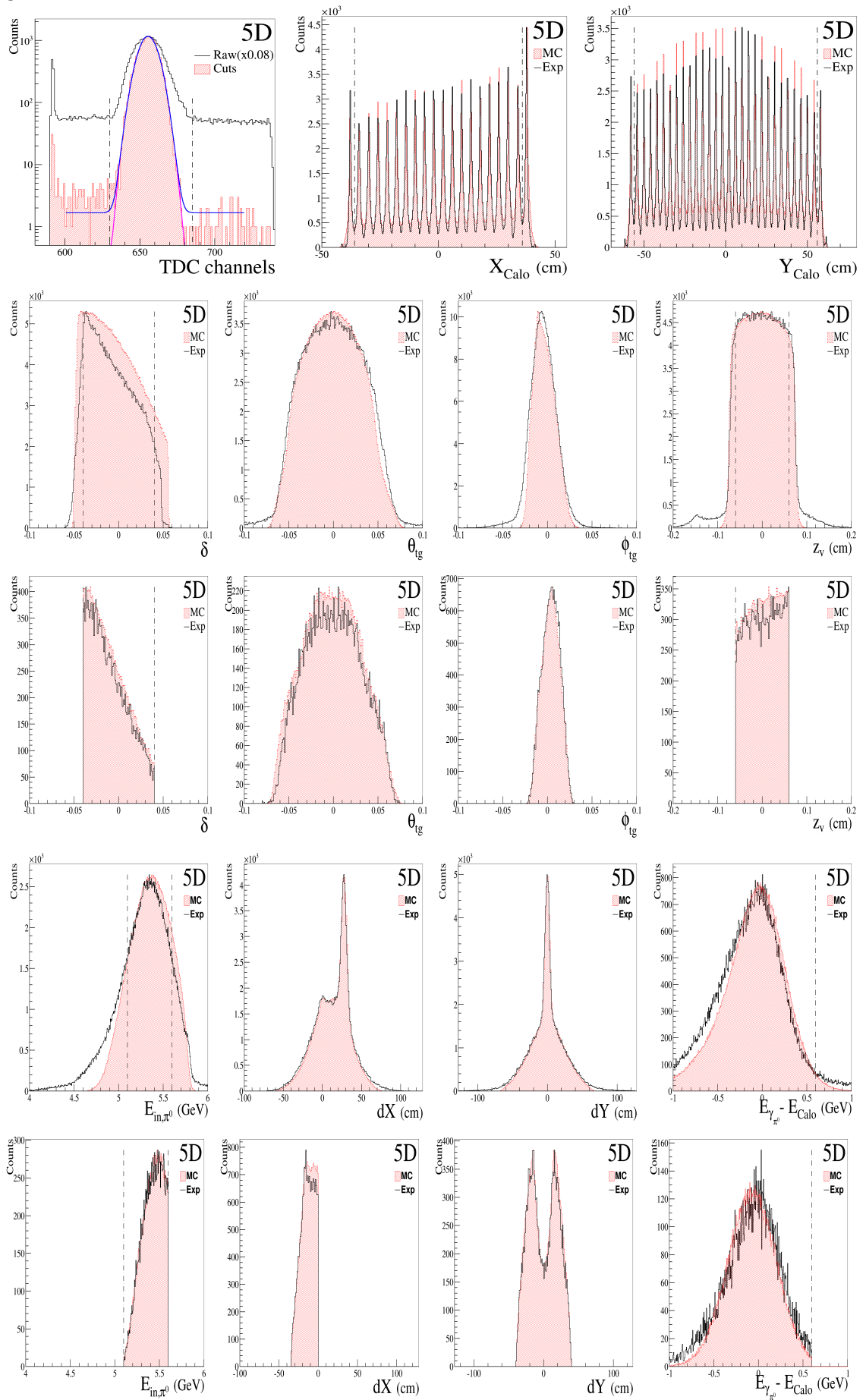
5B

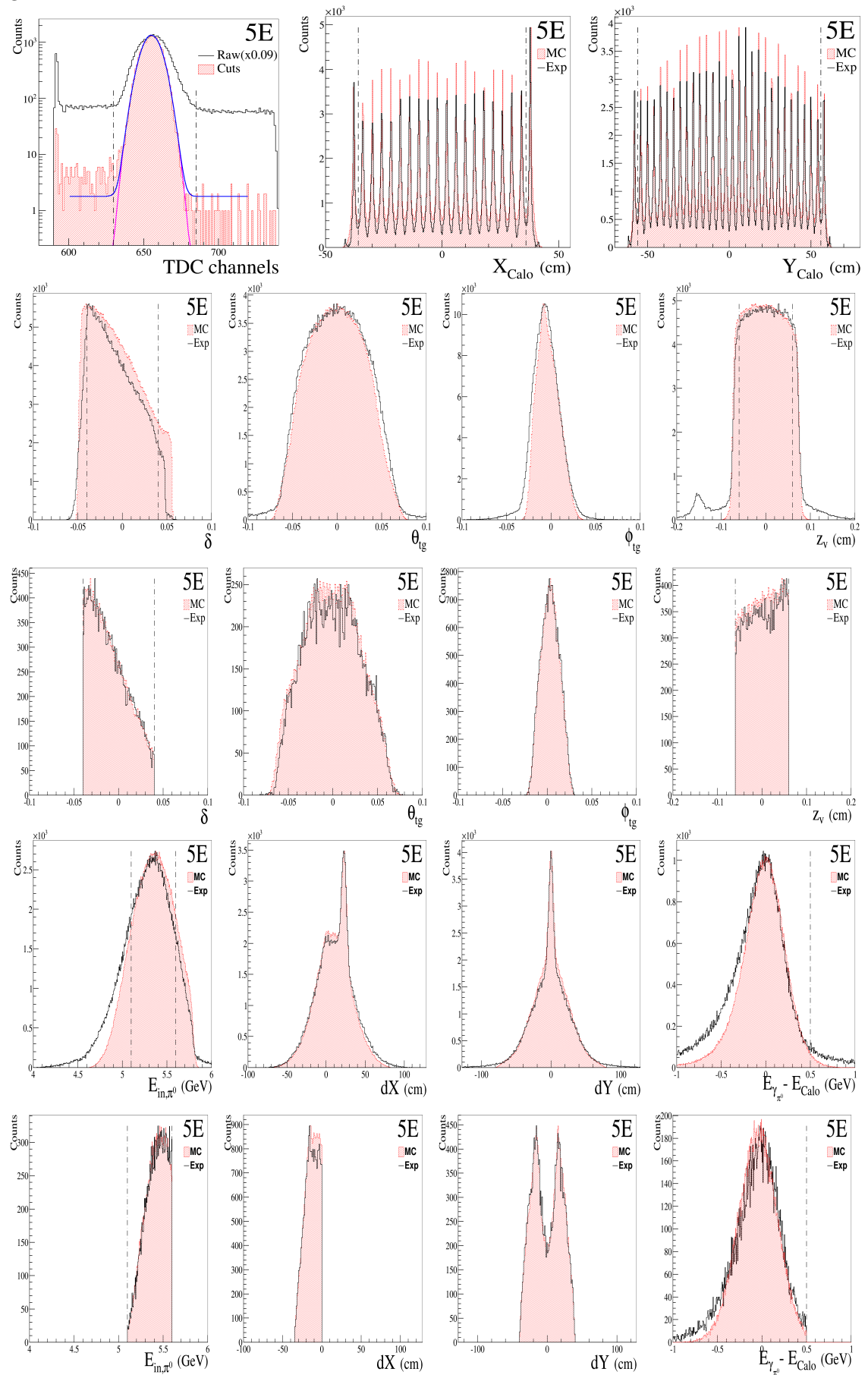


5C

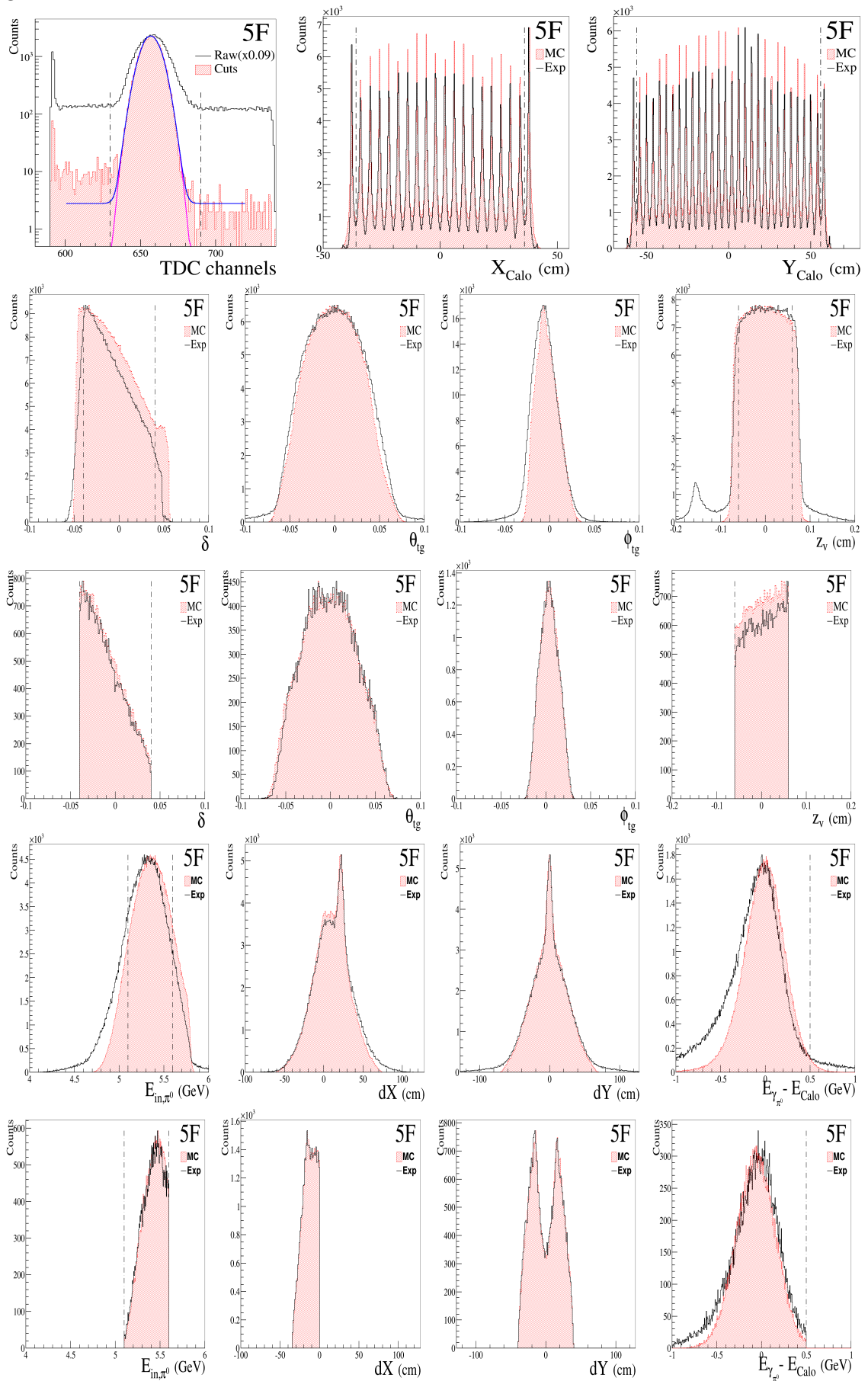


5D

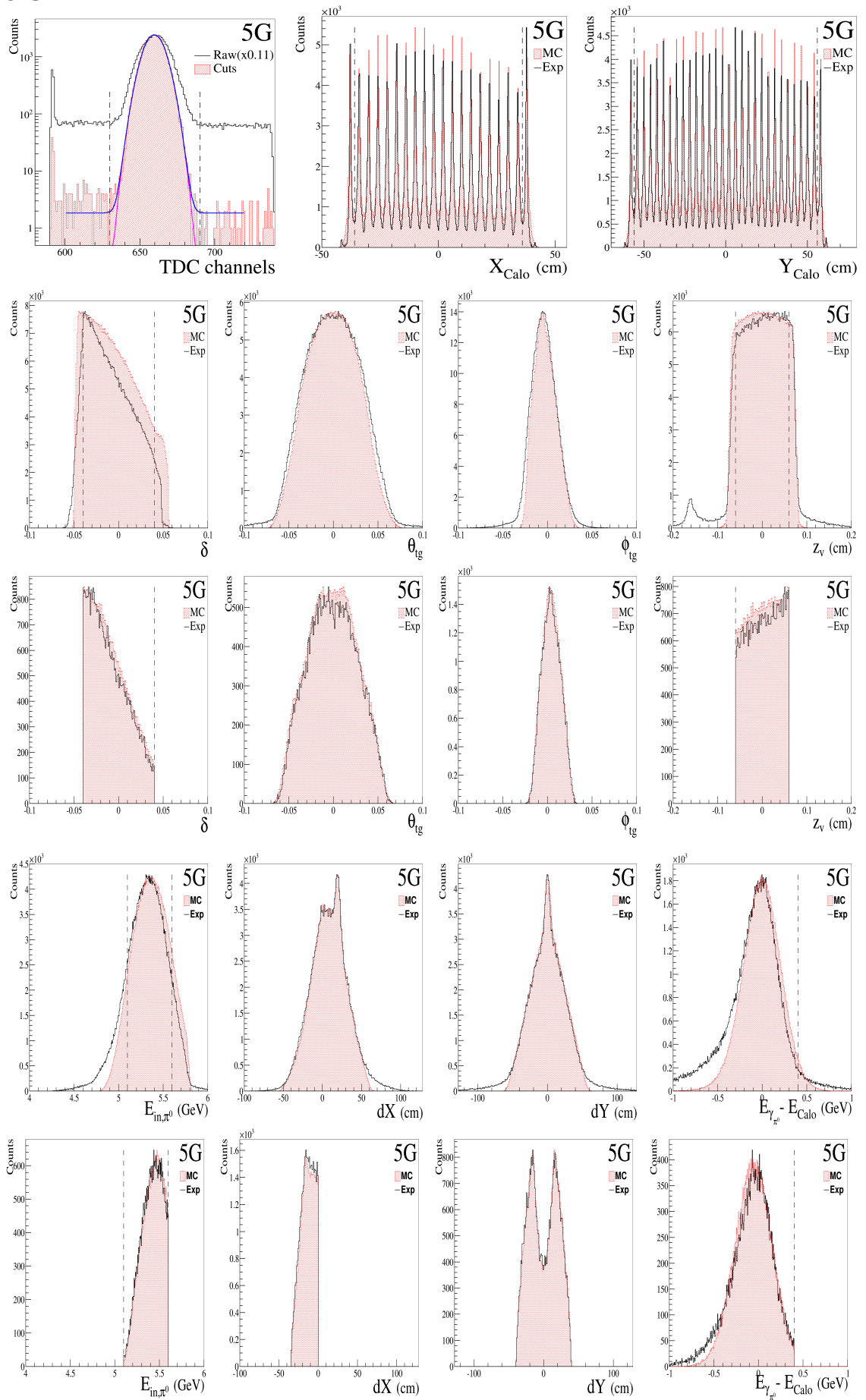


5E


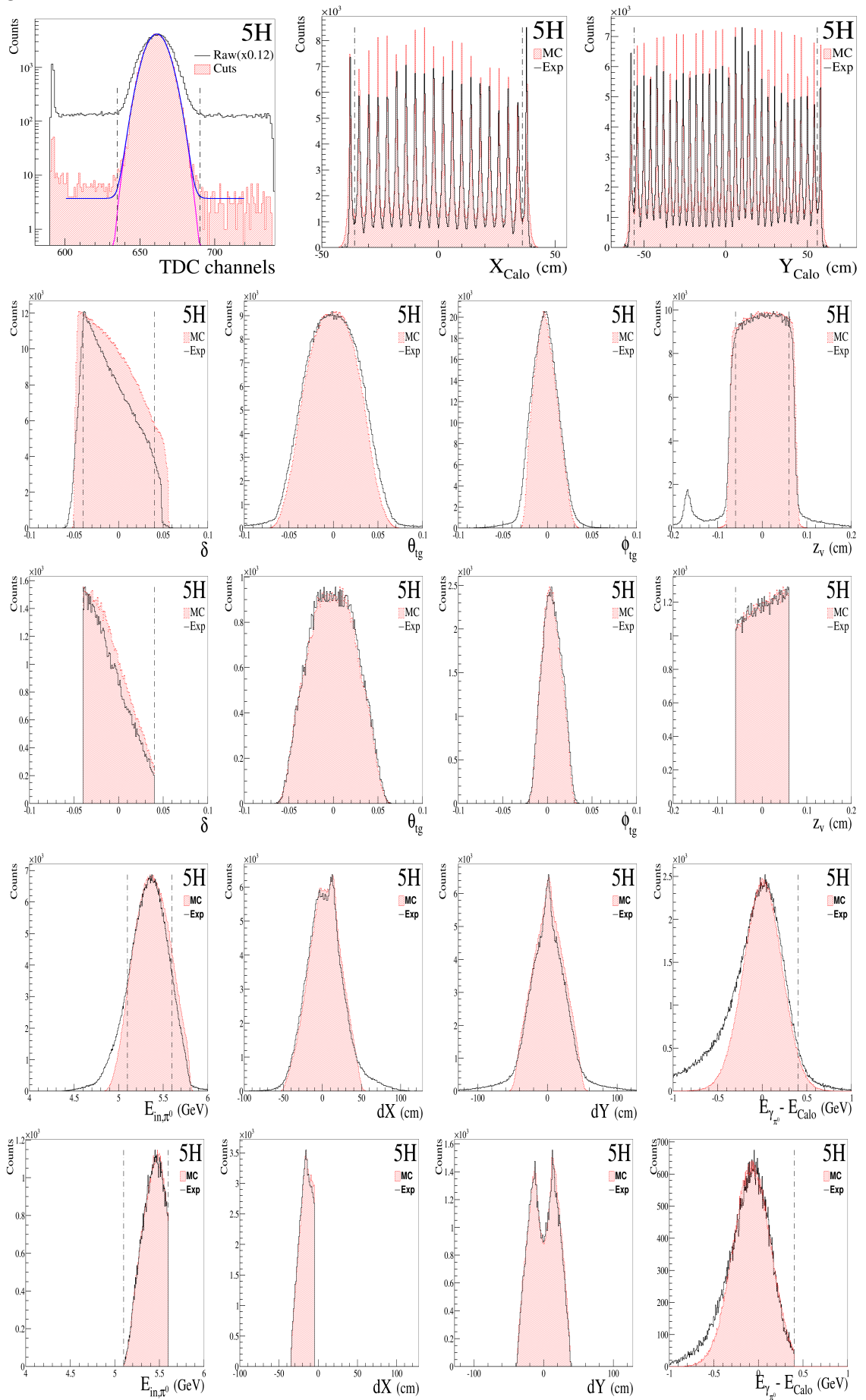
5F



5G



5H



Appendix D

Raw yields, Accumulated Charge and Monte Carlo Cross Section

| | Y_{Data} | Y_{MC} | C_{Data} | C_{MC} | $d\sigma_{dt}$ |
|----|------------|----------|------------|----------|----------------|
| 2A | 39608 | 7966 | 0.0245 | 0.00457 | 910 |
| 2B | 55908 | 27665 | 0.0137 | 0.00596 | 714 |
| 2C | 44705 | 28901 | 0.0325 | 0.00820 | 522 |
| 3A | 26525 | 30002 | 0.0901 | 0.0946 | 85.5 |
| 3B | 3904 | 50023 | 0.0505 | 0.429 | 15.3 |
| 3C | 14339 | 83109 | 0.0736 | 0.586 | 11.7 |
| 3D | 54467 | 30387 | 0.134 | 0.126 | 17.0 |
| 3E | 72911 | 8354 | 0.139 | 0.0275 | 24.3 |
| 3F | 50001 | 22453 | 0.102 | 0.0585 | 39.3 |
| 4A | 43046 | 102611 | 0.183 | 0.627 | 19.2 |
| 4B | 3979 | 79915 | 0.187 | 1.17 | 6.55 |
| 4C | 3671 | 30754 | 0.118 | 0.582 | 3.21 |
| 4D | 46513 | 62315 | 0.508 | 1.11 | 2.10 |
| 4E | 27860 | 98278 | 0.274 | 1.31 | 2.11 |
| 4F | 26342 | 94271 | 0.259 | 0.916 | 3.06 |
| 4G | 48810 | 80729 | 0.336 | 0.560 | 4.72 |
| 4H | 100895 | 83573 | 0.418 | 0.390 | 8.69 |
| 5A | 3767 | 41130 | 0.199 | 1.82 | 1.34 |
| 5B | 4797 | 76175 | 0.381 | 5.15 | 0.944 |
| 5C | 9669 | 60185 | 0.387 | 3.29 | 0.773 |
| 5D | 18018 | 144652 | 0.682 | 6.08 | 0.674 |
| 5E | 20691 | 82744 | 0.649 | 2.66 | 0.676 |
| 5F | 36220 | 92602 | 1.02 | 2.80 | 0.703 |
| 5G | 40131 | 197733 | 0.822 | 5.25 | 0.798 |
| 5H | 70161 | 208035 | 1.43 | 4.27 | 1.01 |

Table D.1: Raw extracted data. The units are Coulomb for the accumulated charges and nb/GeV² for the cross section. Note that the subtraction of random events is already applied in Y_{Data} , but not tracking, triggering, deadtime or virtual photon corrections.

Bibliography

- [1] M. Gell-Mann. “A schematic model of baryons and mesons”. *Physics Letters* 8.3 (1964), pp. 214–215.
- [2] G. Zweig et al. *An $SU(3)$ model for strong interaction symmetry and its breaking. I & II (1964)*. Tech. rep. CERN-TH-412, TH401.
- [3] M. Gell-Mann et al. “The eightfold way”. *Prog Theoret Phys (Kyoto)* 27 (1962), pp. 949–966.
- [4] M. Gell-Mann. *The eightfold way: A theory of strong interaction symmetry*. Tech. rep. California Inst. of Tech., Pasadena. Synchrotron Lab., 1961.
- [5] V. Barnes et al. “Observation of a hyperon with strangeness minus three”. *Physical Review Letters* 12.8 (1964), pp. 204–206.
- [6] D. J. Gross et al. “Ultraviolet behavior of non-abelian gauge theories”. *Physical Review Letters* 30.26 (1973), p. 1343.
- [7] D. J. Gross et al. “Asymptotically free gauge theories. I”. *Physical Review D* 8.10 (1973), p. 3633.
- [8] H. D. Politzer. “Reliable perturbative results for strong interactions”. *Physical Review Letters* 30.26 (1973), pp. 1346–1349.
- [9] H. D. Politzer. “Asymptotic freedom: An approach to strong interactions”. *Physics Reports* 14.4 (1974), pp. 129–180.
- [10] K. G. Wilson. “Confinement of quarks”. *Physical Review D* 10.8 (1974), p. 2445.
- [11] A. Jaffe et al. “Yang-Mills Existence and Mass Gap”. *Millenium Prize Problems, Clay Mathematics Institute, Cambridge, MA* (2000).

- [12] Y. Nambu. “Quasi-particles and gauge invariance in the theory of superconductivity”. *Physical Review* 117.3 (1960), p. 648.
- [13] Y. Nambu et al. “Dynamical model of elementary particles based on an analogy with superconductivity. I”. *Physical Review* 122.1 (1961), p. 345.
- [14] J. Bardeen et al. “Theory of superconductivity”. *Physical Review* 108.5 (1957), p. 1175.
- [15] J. Goldstone. “Field theories with «Superconductor» solutions”. *Il Nuovo Cimento* 19.1 (1961), pp. 154–164.
- [16] R. W. McAllister et al. “Elastic Scattering of 188-Mev Electrons from the Proton and the Alpha Particle”. *Phys. Rev.* 102 (1956), pp. 851–856.
- [17] R. Hofstadter et al. “Electron Scattering from the Proton”. *Phys. Rev.* 98.1 (1955), pp. 217–218.
- [18] R. Hofstadter. “Electron Scattering and Nuclear Structure”. *Rev. Mod. Phys.* 28.3 (1956), pp. 214–254.
- [19] A. W. Thomas et al. *The Structure of the Nucleon, 2001*. 2001.
- [20] P. E. Bosted. “Empirical fit to the nucleon electromagnetic form factors”. *Phys. Rev. C* 51.1 (1995), pp. 409–411.
- [21] M. K. Jones et al. “ G_{E_p}/G_{M_p} Ratio by Polarization Transfer in $\vec{e}p \rightarrow e\vec{p}$ ”. *Physical review letters* 84.7 (2000), p. 1398.
- [22] O. Gayou et al. “Measurement of G_{E_p}/G_{M_p} in $\vec{e}p \rightarrow e\vec{p}$ to $Q^2 = 5.6 \text{ GeV}^2$ ”. *Physical review letters* 88.9 (2002), p. 092301.
- [23] R. G. Arnold et al. “Polarization transfer in elastic electron scattering from nucleons and deuterons”. *Physical Review C* 23.1 (1981), p. 363.
- [24] M. N. Rosenbluth. “High Energy Elastic Scattering of Electrons on Protons”. *Phys. Rev.* 79 (1950), pp. 615–619.
- [25] C. Perdrisat et al. “Nucleon electromagnetic form factors”. *Progress in Particle and Nuclear Physics* 59.2 (2007), pp. 694–764.
- [26] E. Brash et al. “New empirical fits to the proton electromagnetic form factors”. *Physical Review C* 65.5 (2002), p. 051001.

- [27] W. Alberico et al. “Electromagnetic form factors of the nucleon: New fit and analysis of uncertainties”. *Physical Review C* 79.6 (2009), p. 065204.
- [28] J. Blümlein. “The theory of deeply inelastic scattering”. *Progress in Particle and Nuclear Physics* 69 (2013), pp. 28–84.
- [29] M. Breidenbach et al. “Observed behavior of highly inelastic electron-proton scattering”. *Physical Review Letters* 23.16 (1969), p. 935.
- [30] H. W. Kendall. “Deep inelastic scattering: Experiments on the proton and the observation of scaling”. *Reviews of Modern Physics* 63.3 (1991), pp. 597–614.
- [31] J. Beringer et al. “Review of particle physics”. *Physical Review D* 86.1 (2012).
- [32] J. Ashman et al. “A measurement of the spin asymmetry and determination of the structure function g_1 in deep inelastic muon-proton scattering”. *Physics Letters B* 206.2 (1988), pp. 364–370.
- [33] X. Ji. “Gauge-invariant decomposition of nucleon spin”. *Physical Review Letters* 78.4 (1997), p. 610.
- [34] X. Ji. “Deeply virtual Compton scattering”. *Physical Review D* 55.11 (1997), p. 7114.
- [35] A. Radyushkin. “Scaling limit of deeply virtual Compton scattering”. *Physics Letters B* 380.3 (1996), pp. 417–425.
- [36] A. Radyushkin. “Asymmetric gluon distributions and hard diffractive electroproduction”. *Physics Letters B* 385.1 (1996), pp. 333–342.
- [37] P. Kroll. “Generalized Parton Distributions and wide-angle exclusive scattering”. *Nuclear Physics B-Proceedings Supplements* 135 (2004), pp. 168–172.
- [38] A. Radyushkin. “Nonforward parton densities and soft mechanism for form factors and wide-angle Compton scattering in QCD”. *Physical Review D* 58.11 (1998), p. 114008.
- [39] H. W. Huang et al. “Large momentum transfer electroproduction of mesons”. *The European Physical Journal C-Particles and Fields* 17.3 (2000), pp. 423–435.

- [40] P. Kroll. “Wide-angle exclusive scattering-an update”. *Nuclear Physics A* 782.1 (2007), pp. 77–85.
- [41] H. Huang et al. “Signatures of the handbag mechanism in wide-angle photoproduction of pseudoscalar mesons”. *The European Physical Journal C-Particles and Fields* 33.1 (2004), pp. 91–103.
- [42] S. J. Brodsky et al. “Scaling laws at large transverse momentum”. *Physical Review Letters* 31.18 (1973), p. 1153.
- [43] V. Matveev et al. “Automodellism in the large-angle elastic scattering and structure of hadrons”. *Lettere Al Nuovo Cimento (1971–1985)* 7.15 (1973), pp. 719–723.
- [44] G. P. Lepage et al. “Exclusive processes in perturbative quantum chromodynamics”. *Physical Review D* 22.9 (1980), p. 2157.
- [45] D. Dutta et al. “Generalized counting rule and oscillatory scaling”. *Physical Review C* 71.3 (2005), p. 032201.
- [46] S. J. Brodsky et al. “Helicity selection rules and tests of gluon spin in exclusive quantum-chromodynamic processes”. *Physical Review D* 24.11 (1981), p. 2848.
- [47] T. Gousset et al. “Hadron helicity violation in exclusive processes: Quantitative calculations in leading order QCD”. *Physical Review D* 53.3 (1996), p. 1202.
- [48] M. Shupe et al. “Neutral-pion photoproduction and proton Compton scattering at large angles”. *Physical Review D* 19.7 (1979), p. 1921.
- [49] M. Shupe et al. “Proton Compton Scattering and Neutral-Pion Photoproduction at Large Angles”. *Physical Review Letters* 40.5 (1978), p. 271.
- [50] M. Deutsch et al. “Recoil-Proton Polarization in Neutral-Pion Photoproduction and in Proton Compton Scattering”. *Physical Review Letters* 29.26 (1972), p. 1752.
- [51] D. Hamilton. “Polarization Transfer in Proton Compton Scattering at High Momentum Transfer”. PhD thesis. University of Glasgow, 2004.

- [52] D. J. Hamilton et al. “Polarization Transfer in Proton Compton Scattering at High Momentum Transfer”. *Phys. Rev. Lett.* 94 (24 2005), p. 242001.
- [53] A. Danagoulian. “Measurement of compton Scattering on the Proton at 2-6 GeV”. PhD thesis. University of Illinois at Urbana-Champaign, 2006.
- [54] A. Danagoulian et al. “Compton-scattering cross section on the proton at high momentum transfer”. *Physical review letters* 98.15 (2007), p. 152001.
- [55] V. Mamyan. “Real Compton Scattering on the Proton at Large Momentum Transfer”. PhD thesis. Yerevan Physics Institute, 2005.
- [56] H. Huang et al. “Perturbative and non-perturbative QCD corrections to wide-angle Compton scattering”. *The European Physical Journal C-Particles and Fields* 23.2 (2002), pp. 301–310.
- [57] M. Diehl et al. “Proton mass effects in wide-angle Compton scattering”. *Phys. Rev. D* 67 (3 2003), p. 037502.
- [58] G. A. Miller. “Handling the handbag diagram in Compton scattering on the proton”. *Phys. Rev. C* 69 (5 2004), p. 052201.
- [59] T. Brooks et al. “Recalculation of proton Compton scattering in perturbative QCD”. *Phys. Rev. D* 62 (11 2000), p. 114021.
- [60] F. Cano et al. “Real and virtual Compton scattering in a Regge approach”. *Physics Letters B* 551.3 - 4 (2003), pp. 317 –323.
- [61] E. Klempt et al. “Baryon spectroscopy”. *Reviews of Modern Physics* 82.2 (2010), p. 1095.
- [62] M. Dugger et al. “ π^0 photoproduction on the proton for photon energies from 0.675 to 2.875 GeV”. *Physical Review C* 76.2 (2007), p. 025211.
- [63] O. Bartholomy et al. “Neutral-Pion Photoproduction off Protons in the Energy Range $0.3 \text{ GeV} < E_\gamma < 3 \text{ GeV}$ ”. *Physical review letters* 94.1 (2005), p. 012003.
- [64] H. Van Pee et al. “Photoproduction of π mesons off protons from the Δ (1232) region to $E_\gamma = 3 \text{ GeV}$ ”. *The European Physical Journal A-Hadrons and Nuclei* 31.1 (2007), pp. 61–77.

- [65] V. Crede et al. “Photoproduction of neutral pions off protons”. *Physical Review C* 84.5 (2011), p. 055203.
- [66] R. Anderson et al. “Measurements of exclusive photoproduction processes at large values of t and u from 4 to 7.5 GeV”. *Physical Review D* 14.3 (1976), p. 679.
- [67] M. Braunschweig et al. “Single photoproduction of neutral π -mesons on hydrogen at small angles between 4 and 5.8 GeV”. *Physics Letters B* 26.6 (1968), pp. 405–409.
- [68] R. Anderson et al. “Measurements of π^0 and η^0 Photoproduction at Incident Gamma-Ray Energies of 6.0-17.8 GeV”. *Physical Review Letters* 21.6 (1968), p. 384.
- [69] R. Anderson et al. “Neutral-Boson Photoproduction on Hydrogen at High Energies”. *Physical Review D* 1.1 (1970), p. 27.
- [70] R. L. Anderson et al. “High-Energy π^0 Photoproduction from Hydrogen with Unpolarized and Linearly Polarized Photons”. *Physical Review D* 4.7 (1971), p. 1937.
- [71] C. White et al. “Comparison of 20 exclusive reactions at large t ”. *Physical Review D* 49.1 (1994), p. 58.
- [72] L. Zhu et al. “Cross section measurements of charged pion photoproduction in hydrogen and deuterium from 1.1 to 5.5 GeV”. *Physical Review C* 71.4 (2005), p. 044603.
- [73] L. Alexa et al. “Measurements of the Deuteron Elastic Structure Function $A(Q^2)$ for $0.7 \leq Q^2 \leq 6.0$ (GeV/c) 2 at Jefferson Laboratory”. *Physical Review Letters* 82.7 (1999), p. 1374.
- [74] R. G. Arnold et al. “Measurement of Elastic Electron Scattering from the Proton at High Momentum Transfer”. *Phys. Rev. Lett.* 57 (2 1986), pp. 174–177.

- [75] L. Andivahis et al. “Measurements of the electric and magnetic form factors of the proton from $Q^2=1.75$ to 8.83 (GeV/c)²”. *Phys. Rev. D* 50 (9 1994), pp. 5491–5517.
- [76] J. Napolitano et al. “Measurement of the Differential Cross Section for the reaction ${}^2\text{H}(\gamma, p)n$ at High Photon Energies and $\theta_{\text{c.m.}} = 90^\circ$ ”. *Phys. Rev. Lett.* 61 (22 1988), pp. 2530–2533.
- [77] S. J. Freedman et al. “Two-body disintegration of the deuteron with 0.8–1.8 GeV photons”. *Phys. Rev. C* 48 (4 1993), pp. 1864–1878.
- [78] J. E. Belz et al. “Two-Body Photodisintegration of the Deuteron up to 2.8 GeV”. *Phys. Rev. Lett.* 74 (5 1995), pp. 646–649.
- [79] C. Bochna et al. “Measurements of Deuteron Photodisintegration up to 4.0 GeV”. *Phys. Rev. Lett.* 81 (21 1998), pp. 4576–4579.
- [80] D. Meekins et al. “Coherent π^0 photoproduction on the deuteron up to 4 GeV”. *Physical Review C* 60.5 (1999), p. 052201.
- [81] K. Wijesooriya et al. “Polarization measurements in neutral pion photoproduction”. *Physical Review C* 66.3 (2002), p. 034614.
- [82] W. Luo et al. “Polarization Components in π^0 Photoproduction at Photon Energies up to 5.6 GeV”. *Physical review letters* 108.22 (2012), p. 222004.
- [83] B. Wojtsekhowski et al. “Exclusive Compton Scattering on the Proton” (1999).
- [84] <http://www.jlab.org>.
- [85] H. Grunder et al. “The continuous electron beam accelerator facility”. *Nuclear Physics A* 478.0 (1988), pp. 831–846.
- [86] C. W. Leemann et al. “The Continuous Electron Beam Accelerator Facility: CEBAF at the Jefferson Laboratory”. *Annual Review of Nuclear and Particle Science* 51.1 (2001), pp. 413–450.
- [87] <https://hallaweb.jlab.org/equipment/targets.html>.
- [88] J. Matthews et al. “Accurate formulae for the calculation of high energy electron bremsstrahlung spectra”. *Nuclear Instruments and Methods* 111.1 (1973), pp. 157–168.

- [89] L. Azhgirey et al. “Measurement of analyzing powers for the reaction $\vec{p} + CH_2$ at $p_p = 1.75 - 5.3 \text{ GeV}/c$ ”. *Nuclear Instruments and Methods in Physics Research Section A: Accelerators, Spectrometers, Detectors and Associated Equipment* 538.1 (2005), pp. 431–441.
- [90] J. Alcorn et al. “Basic instrumentation for Hall A at jefferson lab”. *Nuclear Instruments and Methods in Physics Research Section A: Accelerators, Spectrometers, Detectors and Associated Equipment* 522.3 (2004), pp. 294–346.
- [91] N. Liyanage. *Optics Calibration of the Hall A High Resolution Spectrometers using the new optimizer*. Tech. rep. 2002, pp. 244–248.
- [92] R. Brun et al. “ROOT - an object oriented data analysis framework”. *Nuclear Instruments and Methods in Physics Research Section A: Accelerators, Spectrometers, Detectors and Associated Equipment* 389.1 (1997), pp. 81–86.
- [93] W. H. Press. *Numerical recipes 3rd edition: The art of scientific computing*. Cambridge university press, 2007.
- [94] K. Amako et al. “Geant4 and its validation”. *Nuclear Physics B-Proceedings Supplements* 150 (2006), pp. 44–49.
- [95] S. Agostinelli et al. “GEANT4: a simulation toolkit”. *Nuclear instruments and methods in physics research section A: Accelerators, Spectrometers, Detectors and Associated Equipment* 506.3 (2003), pp. 250–303.
- [96] D. Meekins. *Bremsstrahlung codes*. Tech. rep. Jefferson Laboratory, 2000.
- [97] J. Matthews et al. “The distribution of electron energy losses in thin absorbers”. *Nuclear Instruments and Methods* 180.2 (1981), pp. 573–579.
- [98] W. Heitler. *The quantum theory of radiation*. Courier Dover Publications, 1954.
- [99] H. W. KOCH et al. “Bremsstrahlung Cross-Section Formulas and Related Data”. *Rev. Mod. Phys.* 31 (4 1959), pp. 920–955.
- [100] Y. Tsai. “Pair production and bremsstrahlung of charged leptons”. *Rev. Mod. Phys.* 46 (4 1974), pp. 815–851.

- [101] M. L. Perl. *Notes on the Landau, Pomeranchuk, Migdal effect*. Tech. rep. SCAN/9408125, 1994.
- [102] P. Anthony et al. “Bremsstrahlung suppression due to the Landau-Pomeranchuk-Migdal and dielectric effects in a variety of materials”. *Physical Review D* 56.3 (1997), p. 1373.
- [103] P. Anthony et al. “Measurement of dielectric suppression of bremsstrahlung”. *Physical review letters* 76.19 (1996), p. 3550.
- [104] S. Chauvie et al. “Validation of Geant4 bremsstrahlung models: first results”. *Nuclear Science Symposium Conference Record, 2006. IEEE*. Vol. 3. IEEE. 2006, pp. 1511–1515.
- [105] R. Ent et al. “Radiative corrections for $(e, e'p)$ reactions at GeV energies”. *Phys. Rev. C* 64 (5 2001), p. 054610.
- [106] A. Puckett. “Recoil Polarization Measurements of the Proton Electromagnetic Form Factor Ratio to High Momentum Transfer”. PhD thesis. MIT, 2010.
- [107] H. Bethe. “Moliere’s theory of multiple scattering”. *Physical Review* 89.6 (1953), p. 1256.
- [108] https://hallcweb.jlab.org/wiki/index.php/SIMC_Monte_Carlo.
- [109] M. Roedelbronn. *Determination of $B \cdot dl$ dependence for RCS deflection magnet*. Tech. rep. University of Illinois, 2004.
- [110] L. Zhu. “Exclusive photoproduction of charged pions in hydrogen and deuterium from 1 to 6 GeV”. PhD thesis. Massachusetts Institute of Technology, 2004.
- [111] E. V. Hungerford. “Experimental considerations in electromagnetic production of hypernuclei”. *Progress of Theoretical Physics Supplement* 117 (1994), pp. 135–149.
- [112] *ESPACE, Manual version 2.9.0 β* . The Hall A Collaboration. 2002.